Modification of Characteristics of Multi-Metallic Nanoparticles via Electronic Charge Transfer toward Novel Bio/Chemical Sensing Probes

DAO THI NGOC ANH

Japan Advanced Institute of Science and Technology

Doctoral Dissertation

Modification of Characteristics of Multi-Metallic Nanoparticles via Electronic Charge Transfer toward Novel Bio/Chemical Sensing Probes

DAO THI NGOC ANH

Supervisor: Professor Shinya Maenosono

School of Materials Science

Japan Advanced Institute of Science and Technology

September 2014

Abstract

Plasmonic metallic nanoparticles have been explored extensively in terms of their fundamental and practical applications such as for optoelectronic devices, optical metamaterials, sensors, and solar cells as well as many others. During the past decade the concomitant rapid development of plasmonics into a vibrant sub-area of nanotechnology has focused almost entirely on Au and Ag as (nano) plasmonic metals. Ag provides high enhanced-Raman activity, while the Au provides excellent chemical stability and a great reactivity with sulfur containing biomolecules, which has inevitably leaded to the combination of Au and Ag in a single nanoparticle system. The synthetic approach to Au-Ag nanoparticles still has many obstacles. Aqueous synthesis techniques for Ag nanoparticles are advantageous for biological applications because the resulting nanoparticles can often be used directly, yet these techniques typically provide unstable Ag nanoparticles of low monodispersity, or with a size that is difficult to control. In addition, it is still challenging to synthesize well-defined uniform Ag@Au nanoparticles because the Ag core is easily etched away due to the galvanic replacement reaction between Au ions and the Ag metal cores which causes gaps in the Au shell or hollow sections at the interface of the core and the shell. In my research, Au@Ag core-shell nanoparticles were demonstrated to have better chemical stability and very high SERS activity together with tunable size, shell thickness and plasmonic properties. Moreover, Ag in the shell also could suppress the galvanic replacement reaction allowing the formation of double shell (Au@Ag)@Au nanoparticles without any defects or gaps in the structure. All of these attractive aspects arise from the electron transfer phenomenon which has been shown to occur in the Au-Ag system.

By extending this phenomenon to other silver based NP systems, insight can be gained into how to manipulate the particle structure and composition towards the desired characteristics. With this goal in mind, we created a series of different sized platinum particles and coated them in silver shells of various thicknesses. In this case, platinum was chosen as a core material because of its status as a noble metal, its *fcc* crystal structure (the same as for silver), and its chemical similarity to gold. The resulting particles were characterized in terms of their structural/composition properties, and then the electronic properties of these probes were analyzed by using X-Ray Photoelectron Spectroscopy. The results demonstrate that the electronic transfer phenomenon can be extended to a wide range of heterostructure systems, and provides insight into how to exploit electronic transfer to create silver based sensing probes with enhanced robustness, high optical/plasmonic activity and plasmonic characteristics that can be tuned for a desired application.

Electron transfer or charge transfer phenomenon is very attractive as a route to manipulate the properties of materials and also presents a complex challenge. Understanding the mechanism of operation and its effect to materials characteristics can lead us to systematically design materials with distinct characteristics for specific applications. My PhD research attempted to make clear the controllability of electron transfer phenomenon specifically in multi-metallic nanomaterials. In order to have the full picture of electron transfer phenomenon, we clarify the interaction among three noble metals (Ag, Au and Pt) by comparing Au-Ag, Pt-Ag and Au-Pt in homogeneous and heterogeneous nanostructure. This fundamental research will provide scientists with a useful tool in understanding, designing and controlling the properties of metallic nanomaterials. In addition, nanoparticles which are composed of Au, Ag or Pt are promising not only in biosensing and diagnostics applications but also are a good candidate for medical – therapy or catalyst applications.

Keywords: noble metal, heterostructure, nanoparticle, electron charge transfer, biosensor.

Acknowledgments

My first words are to acknowledge all those people who had helped, contributed to the works in this dissertation. It will be an impossible task if I, myself alone, work on all things such as doing research and experiments and many more things. In the foremost position of my gratitude would stand Prof. Shinya Maenosono for his supervision, advice and guidance to me from the very first days when I newly accustom science. His endless enthusiasm for science has inspired me in doing research and finally this dissertation can be realized. Above all and most needed, he always tries his utmost to encourage and support me in various ways. Once again, I would like to send my most nicely thankful words to him.

Many thanks would go to Prof. Kohki Ebitani, Prof. Kenzo Fujimoto, Prof. Mikio Koyano and Prof. Yuzuru Takamura for their help and advice to me in doing research. I was allowed to use many facilities in their laboratories to do research and these facilities helped forming a big important part of my dissertation. I aslo would like to thank Dr. Koichi Higashimine for many helps and supports in STEM-HAADF measurements.

Working environment is a key point in forming the way and attitude of working to me. I am very lucky to work in a good environment with wise and scholarly colleagues. I especially thank every member from my laboratory during my time at JAIST. My Vietnamese and Japanese friends at JAIST have given me much memorable time. They make my life here happier and more meaningful.

I gratefully send thankful words to my parents and other members in my family. My family has always been encouraging and supporting me and that is a strongest motivation for me to successfully complete this dissertation. I deeply thank Dr. Derrick Mott, my husband, for his support in my scientific works as well as his endless caring and sharing in life.

My last words are to thank to everybody because you deserve that for your importance to me.

Table of Contents

List of Publications

Papers

1. **D.T.N. Anh**, P. Singh, A. Wadhwa, D. Hotta, D Mott, K. Higashimine, S. Maenosono, "Impact of Electron Transfer Effect on Modification of Characteristics of Multi-Metallic Nanoparticles". (In preparation)
2. **D.T.N. Anh**, D. Mott, K. Higashimine, S. Maenosono, "Enhanced Electronic Properties of Pt@Ag Heterostructured Nanoparticles", *Sensors*, **2013**, *13*, 7813.
3. D. Mott, **D.T.N. Anh**, P. Singh, C. Shankar, S. Maenosono, "Electronic Transfer as a Route to Increase the Chemical Stability in Gold and Silver Core-Shell Nanoparticles", *Adv. Colloid Interface Sci.*, **2012**, *185-186*, 14-33.
4. S. Maenosono, J.D. Lee, **D.T.N. Anh**, D. Mott, "Peak Shape Analysis of Ag3d Core-Level X-ray Photoelectron Spectra of Au@Ag Core-Shell Nanoparticles Using an Asymmetric Gaussian-Lorentzian Mixed Function", *Surf. Interface Anal.*, **2012**, *44*, 1611.
5. C. Shankar, **D.T.N. Anh**, P. Singh, K. Higashimine, D. Mott, S. Maenosono,"Chemical Stabilization of Gold Coated by Silver Core-shell Nanoparticles *via* Electron Transfer", *Nanotechnology*, **2012**, *23*, 245704.
6. S. Nishimura, **D.T.N. Anh**, D. Mott, K. Ebitani, S. Maenosono, "X-ray Absorption Near-Edge Structure and X-ray Photoelectron Spectroscopy Studies of Interfacial Charge Transfer in Gold-Silver-Gold Double-Shell Nanoparticles", *J. Phys. Chem. C*, **2012**, *116*, 4511.
7. **D.T.N. Anh**, P. Singh, C. Shankar, D. Mott, S. Maenosono, "Chare-Transfer-Induced Suppression of Galvanic Replacement and Synthesis of (Au@Ag)@Au Double Shell Nanoparticles for Highly Uniform, Robust and Sensitive Bioprobes", *Appl. Phys. Lett.*, **2011**, *99*, 073107.
8. **D.T.N. Anh**, H.T.L. Phuong, H.T.H. Thao, N.T.C. Ha, N.X. Hoan, "Crystal Structures and Properties of ZnO Nanopowders Prepared by Ultrasonic Method", *e-J. Surf. Sci. Nanotech.*, **2011**, *9*, 482.

Book chapters

1. **D.T.N. Anh**, Derrick Mott, Shinya Maenosono, "Characterization of Metallic Nanoparticles Based on the Abundant Usages of X-ray Techniques", *Handbook of nanoparticles, Synthesis, Functionalization and Surface Treatment*, **2015**, Springer-Verlag. (In press)

Proceedings

1. S. Nishimura, **D.T.N. Anh**, D. Mott, K. Ebitani, S. Maenosono, "Spectroscopic Study on the Charge Redistribution between Au and Ag in Au@Ag Core-shell Nanoparticles", *Nanotech Conference Technical Proceedings*, Santa Clara, California, **2012**, *1*, 38.

Abbreviations

ATT	3-Amino-5-mercapto-1,2,4-triazole
CE	Chemical enhancement
CV	Cyclic voltammetry
DNA	Deoxyribonucleic acid
DDA	Discrete dipole approximation
EM	Electromagnetic
EDS	Energy-dispersive X-ray spectroscopy
ELISA	Enzyme-linked immunosorbent assay
FDTD	Finite-difference time-domain
HR-TEM	High-resolution transmission electron microscopy
HcG	Human chorionic gonadotropin
LSPR	Localized surface plasmon resonance
NIR	Near infrared
SCE	Saturated calomel electrode
SEF	Surface enhanced fluorescence
SERS	Surface enhanced-Raman scattering
SPR	Surface plasmon resonance
STEM-HAADF	Scanning TEM at high-angle annular dark-field imaging
TEM	Transmission electron microscopy
UV-Vis	Ultraviolet–visible spectroscopy
XPS	X-ray photoelectron spectroscopy

List of Figures

List of Schemes

List of Tables

Chapter 1. Introduction

1.1 Modern route of science: Nanotechnology

Nowadays, nanoscience and nanotechnology have been vigorously contributing to materials science and engineering research and many other scientific disciplines. Many of the recent results of the research activities in nanoscience and nanotechnology have led to discovery or improvement of advanced materials for sensors, biosensors, disease detection, optical devices, energy storage, fuel cells, electronics, catalysts, and many others.[1]

The increase of attention in the nano size regime identified by the great advancement driven by novel properties of the new size regime.[2] The prefix nano in the metric system denotes the scale of 10^{-9} meters. If only size is considered in general, nanotechnology deals mostly with materials in the size range from 1 to 100 nanometers. Even recent interest has increased rapidly in this field, indeed the existence of nanoscale materials is actually centuries old. In medieval times, materials with nanoscale sizes have been used to color stained glass windows, or to impart color to cookware.[3] In fact, the ancient uses of colloidal gold or silver nanoparticles took advantage of the optical properties of the particles. Hence the physical or chemical properties of materials in nanoscale sizes are interesting and important because such properties can be promising for use in various applications.[1]

When the size of a material is decreased from its bulk phase to the nano size, the physical and chemical properties of the materials change, which contributes to one of the most important aspects of nanotechnology. The most attractive factor of these materials is the incredible novel properties that are observed for nanomaterials over their bulk counterparts including optical, catalytic, electronic, and magnetic properties as well as many others.[1,2,4]

The small sizes present in nanoscale systems directly influence the energy band structure

and can lead indirectly to changes in the associated atomic structure. Such effects are generally termed quantum confinement. Initially, there are two general descriptions that can account for such size-dependent effects in nanoscale systems.[4]

Changes to the system total energy[4]

In the free electron model, it is clear that the energies of the electronic states depend on $1/L^2$ where L is the dimension of the system in a particular direction; the spacing between successive energy levels also varies as $1/L^2$. Thus if the number of atoms in a system, hence the length scale, is substantially different to that in a normal bulk material, the energies and energy separations of the individual electronic states will be very different. In other words, the number of energy levels in the bulk material model is so large and the gap between them so small that we could treat them as essentially infinite solids with continuous bands of allowed energy. At the nanometer scale, a typical nanoparticle contains 10^2 to 10^4 atoms, which might not be large enough to make a good approximation to an infinite solid. The result is that in nanoparticles, we can still distinguish bands of energy, but the gaps between the bands may differ from those found in the bulk and, within the bands, the energy levels do not quite form a continuum so that we can observe effects due to the quantized nature of levels within bands (Scheme 1.1). Furthermore, as the system size decreases, the allowed energy bands become substantially narrower than in an infinite solid. The main effect of these alterations to the bulk electronic structure is to change the total energy and hence, ignoring entropy considerations, the thermodynamic stability of the reduced length scale system relative to that of a normal bulk crystal. This can have a number of important implications. It may change the most energetically stable form of a particular material; such as small nanoparticles or nanodimensional layers may adopt a different crystal structure from that of the normal bulk material. For example, some metals which normally have an *hcp* atomic arrangement have been reported to adopt a *fcc* structure in confined systems such as

metallic multilayers. If a different crystallographic structure is adopted below some particular critical length scale, then this arises from the corresponding change in the electronic density of states which often results in a reduced total energy for the system. Reduction of system size may change the chemical reactivity, which will be a function of the structure and occupation of the outermost electronic energy levels. Correspondingly, physical properties such as electrical, thermal, optical and magnetic characteristics which also depend on the arrangement of the outermost electronic energy levels, may be changed. For example, metallic systems can undergo metal-insulator transitions as the system size decreases, resulting from the formation of a forbidden energy band gap (Scheme 1.1).

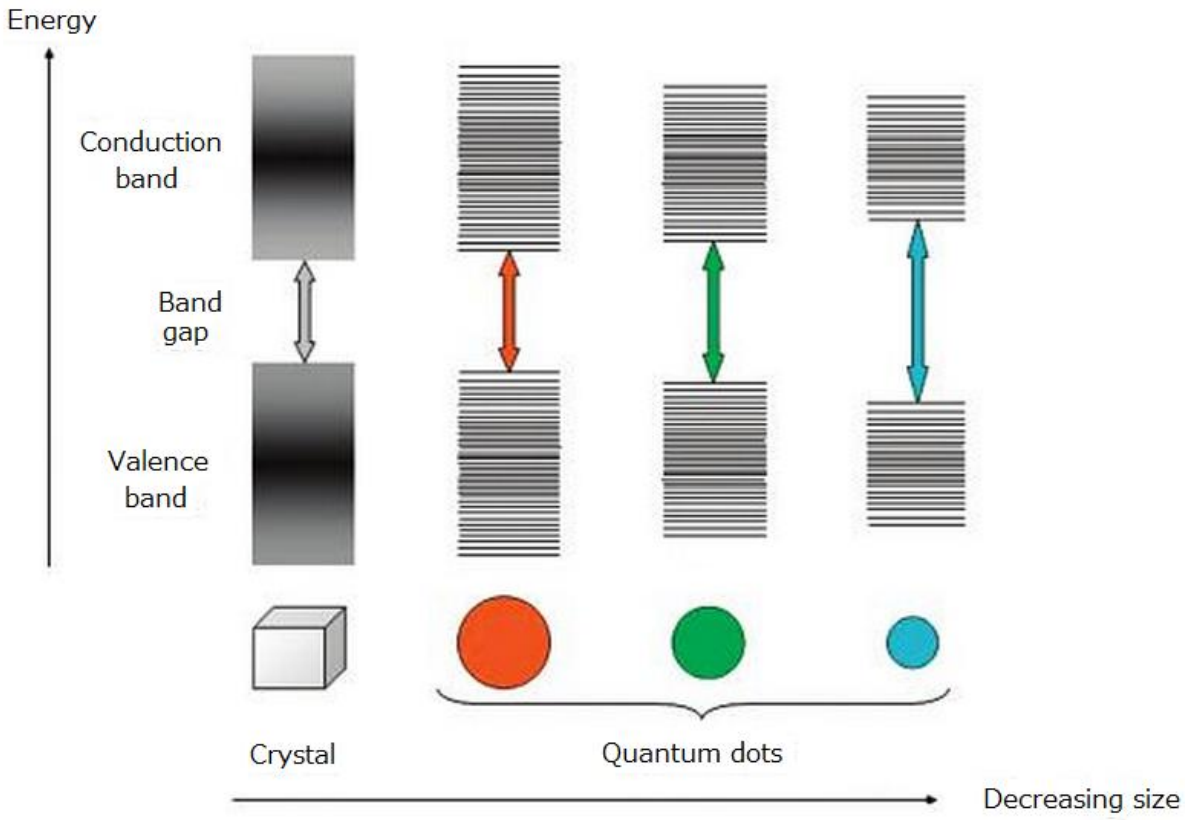

Scheme 1.1. The band gap of a semiconductor depends on its size.[5]

Other properties such as mechanical strength which, to a first approximation, depends on the change in the electronic structure as a function of applied stress and hence interatomic

spacing, may also be affected. Transport properties may also change in that they may now exhibit a quantized rather than continuous behavior owing to the changing nature and separation of the electron energy levels (Scheme 1.1).

Changes to the system structure[4]

A related viewpoint for understanding the changes observed in systems of reduced dimension is to consider the proportion of atoms which are in contact with either a free surface, as in the case of an isolated nanoparticle, or an internal interface, such as a grain boundary in a nanocrystalline solid. Both cases have a very high surface area to mass ratio in comparison to the bulk material.[1] Figure 1.1 shows a plot of particle size vs. the surface area to volume ratio, as well as the percentage of surface atoms for gold nanoparticles.[6]

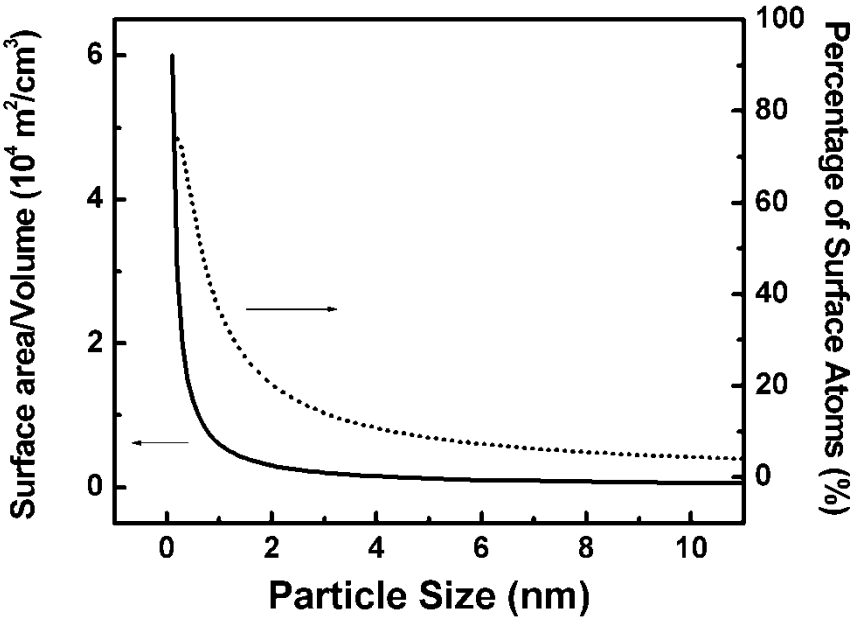

Figure 1.1. A plot of the relationship between partical size, surface area to volume ratio, and percentage of surface atoms.[6]

It can be seen that as the particle size decreases, there is a huge increase in the surface area of the nanomaterials, and also in the percentage of surface atoms which will have

important implications for the total energy of the system. As discussed above this may lead to the stabilization of metastable structures in nanometer-sized systems, which are different from the normal bulk structure or, alternatively, may induce a simple relaxation (expansion or contraction) of the normal crystalline lattice which could in turn alter other materials properties. If an atom is located at a surface then it is clear that the number of nearest-neighbor atoms are reduced, giving rise to differences in bonding (leading to the well-known phenomenon of surface tension or surface energy) and electronic structure. In a small isolated nanoparticle, a large proportion of the total number of atoms will be present either at or near the free surface. Such structural differences in reduced-dimensional systems would be expected to lead to very different properties from the bulk.

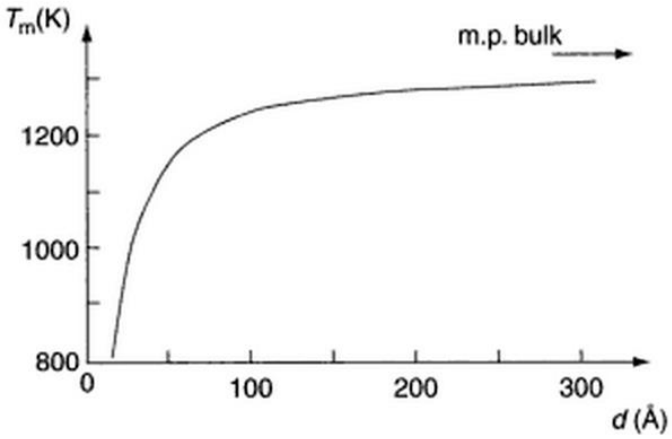

Figure 1.2. Schematic diagram of the variation in melting point of gold nanoparticles as a function of particle size[7]

For example, the melting point of gold particles has been observed to decrease rapidly for particle sizes less than 10 nm,[5,7] as show in figure 1.2. The decrease in the melting point with reduced particle size can be explained by the early thermodynamic model describing melting curves for fine metal particles,[8,9] which relates the melting point of nanoparticles to that of its bulk metal by the equation

$$\frac{T_r - T_\infty}{T_\infty} = -\frac{4}{\rho_s L 2r}\left[\gamma_s - \gamma_l\left(\frac{\rho_s}{\rho_l}\right)^{2/3}\right] \quad (1.1)$$

Where T_r and T_∞ are the melting temperatures of the particle and the bulk solid, respectively, r is the radius of the particle, ρ_s and ρ_l are the densities of the solid and the liquid, respectively, γ_s and γ_l are the surface energies of the solid and liquid, respectively, and L is the heat of fusion.[9]

The investigation of nanoparticles and their unique properties have captured enormous research interests around the world in the past few decades in the dawn of nanotechnology. For example, nanoparticles have found many interesting applications including catalysis[10,11], calorimetric detection of biological target and binding in DNA[12], drug delivery agents[13,14], medical applications e.g. biological imaging[12–14], cancer targeting[15], ultraviolet absorbers (e.g. ZnO and TiO_2)[4], labeling agents, sensors[16], microelectronics[17], coating[4], and many others.

1.2 Nanotechnology in biosensing and diagnostic applications

Nowadays, the number of diseases and various kinds of viruses, bacteria, etc. has become enormous and the increase doesn't seem to slow down. The advancement of biosensors for the diagnosis and monitoring of diseases, drug discovery, proteomics, and environmental detection of biological agents thus is an extremely significant issue. In addition, the elementary functional units of biological systems – enzymes, motors, membranes, nucleic acids, etc. – all comprise from complex nanoscale components. It would have great impact for sensing materials, such as semiconductors, metals and magnets are made on the size scale of individual biological macromolecules.

A biosensor is basically derived from the coupling of a ligand-receptor binding reaction[18] to a signal transducer. There are various principles of signal transduction, such as electrochemical,[19,20] magnetic, mass spectrometric,[21] micromechanical[22], optical,[23,24]

radioactive,[25] and piezoelectric.[26] Among these methods, optical sensors which is particularly based on evanescent electromagnetic fields such as propagating surface plasmon resonance, have attracted many scientists in affinity biosensing applications.[27] Optical detection have become widely used mechanism for detecting biological binding events and for imaging in biological systems. In the near future, single molecule detection will be possible despite the large background present in a living system. Combination of quantum-confined systems, plasmon excitations in metal nanoparticles, and manipulation of the local fields in their environment, with control over the photon density of states, could in fact yield such systems in the coming years.[28]

1.2.1 Surface plasmon resonance and related phenomena

In quantum-mechanical language, plasmon is a quantum of plasma oscillation, and thus are the collective oscillations of the free electron gas density due to long-range Coulombic correlations.[29] Characteristically, noble metal nanoparticles exhibit a strong absorption band in the visible region, and this is indeed a small particle effect, since they are absent in the individual atom as well as in the bulk phase.[30,31] The physical origin of the light absorption by metal nanoparticles is the coherent oscillation of the conduction band electrons induced by the interacting EM field.[32] The EM surface waves can propagate along the interface between conducting materials and a dielectric over a broad range of frequencies, ranging from radio frequencies up to the visible.[33] The oscillation modes comprise an EM field coupled to the oscillations of conduction electrons and are called surface plasmons.[34] These are characterized by strong field enhancement at the interface, while the electric field vector decays exponentially away from the surface (in the nanometer range).[35,36] When the dimensions of the conductor are reduced, boundary and surface effects become very important, and for this reason, the optical properties of small metal nanoparticles are dominated by collective oscillation of conduction electrons.[37] An absorption band results

when the incident photon frequency is resonant with the collective oscillation of the conduction band electrons and is known as the surface plasmon resonance (SPR).[34] SPR in nanometer-sized structures is called localized surface plasmon resonance (LSPR).[38] The resonance frequency of this LSPR is strongly dependent upon the size, shape, interparticle interactions, dielectric properties, and local environment of the nanoparticle.[37]

As a first approximation, the plasmon resonance for a small spherical metal nanoparticle can be understood by a simple Drude free-electron model, assuming that the positively charged metal atoms are fixed in place and that the valence electrons are dispersed throughout a solid sphere of overall positive charge.[39] If the free electrons experience viscous damping due to the positive lattice and no other forces except the applied electromagnetic field, it will lead to[29]

$$\varepsilon = 1 - \frac{\omega_p^2}{\omega^2 + i\gamma\omega} \tag{1.2}$$

where ε is the dielectric function, γ is the damping constant, ω and ω_p is the angular frequency and the plasma frequency, which is a characteristic constant, respectively.

In the quasistatic limit, where the wavelength of light is much larger than the size of the particle, the force exerted by the EM field of the incident light moves all the free-electrons collectively.[40] Using the boundary condition that the electric field is continuous across the surface of the sphere, the static polarizability can be expressed as[39]

$$\alpha = 4\pi R^2 \frac{\varepsilon - \varepsilon_m}{\varepsilon + 2\varepsilon_m} \tag{1.3}$$

where R is the sphere radius, ε is the complex dielectric function of the metal and ε_m is the dielectric constant of the embedding medium. The polarizability shows a resonance when the denominator is minimized, which occurs when the magnitude of the real part of the complex

dielectric function, ε real, is -2ε_m.[39] This resonance condition for the polarizability leads to a strong extinction of light at the plasmon resonance frequency. Within this free-electron description, plasmons can be thought of as collective oscillations of the conduction band electrons induced by an interacting light wave.[40]

To determine the plasmon-resonant properties of arbitrarily shaped particles, solutions to Maxwell's equations must be obtained. For nanoparticles with a spherical symmetry, Mie scattering theory[41] provides a rigorous solution that describes well the optical spectra of spheres of any size. To determine the extinction spectrum of a nanoparticle using the theory, the EM fields must then satisfy Maxwell's boundary conditions of continuity at the junction between the nanoparticle and the embedding medium. Mie scattering theory is exact and it accounts for field-retardation effect that becomes significant for particles whose sizes are comparable to the wavelength of light.[40]

According to the Mie theory, for a metal nanosphere with particle size *2R* much smaller than the wavelength of light λ (quasistatic and dipole limit), the nanoparticle extinction cross-section is given by[41–43]

$$C_{ext} = \frac{24\pi^2 R^3 \varepsilon_m^{3/2}}{\lambda} \frac{\varepsilon_i}{(\varepsilon_r + 2\varepsilon_m)^2 + \varepsilon_i^2} \tag{1.4}$$

Absorption and scattering components of the optical extinction, C_{abs} and C_{sca}, of spherical homogeneous Au nanoparticles can be calculated using Mie theory,[41] which includes the nanoparticle size as a parameter and includes dipolar and all higher order modes.[44] Mie theory calculations of the absorption, scattering and extinction spectra of spherical Au nanoparticles of different sizes are presented in Figure 1.3[42] The extinction band for smaller nanoparticles is predominantly caused by absorption. As the nanoparticle size becomes larger (Figure 1.3a-c), Mie scattering begins to contribute to the total extinction. This is

because larger nanoparticles have a much more enhanced radiative coupling to the outgoing EM field. The scattering quantum yield increase rapidly with increasing nanoparticle diameter (Figure 1.3d).[42] Within the size regime where the dipole mode contributes predominantly, the extinction cross-section increases with a direct dependence on the sphere volume or the total number of electrons in the nanoparticle.[42,45] These trends aid in the selection of nanoparticles for optical applications. Smaller nanoparticles offer light absorption without any scattering losses, whereas larger nanoparticles offer strong light scattering along with absorption.[42]

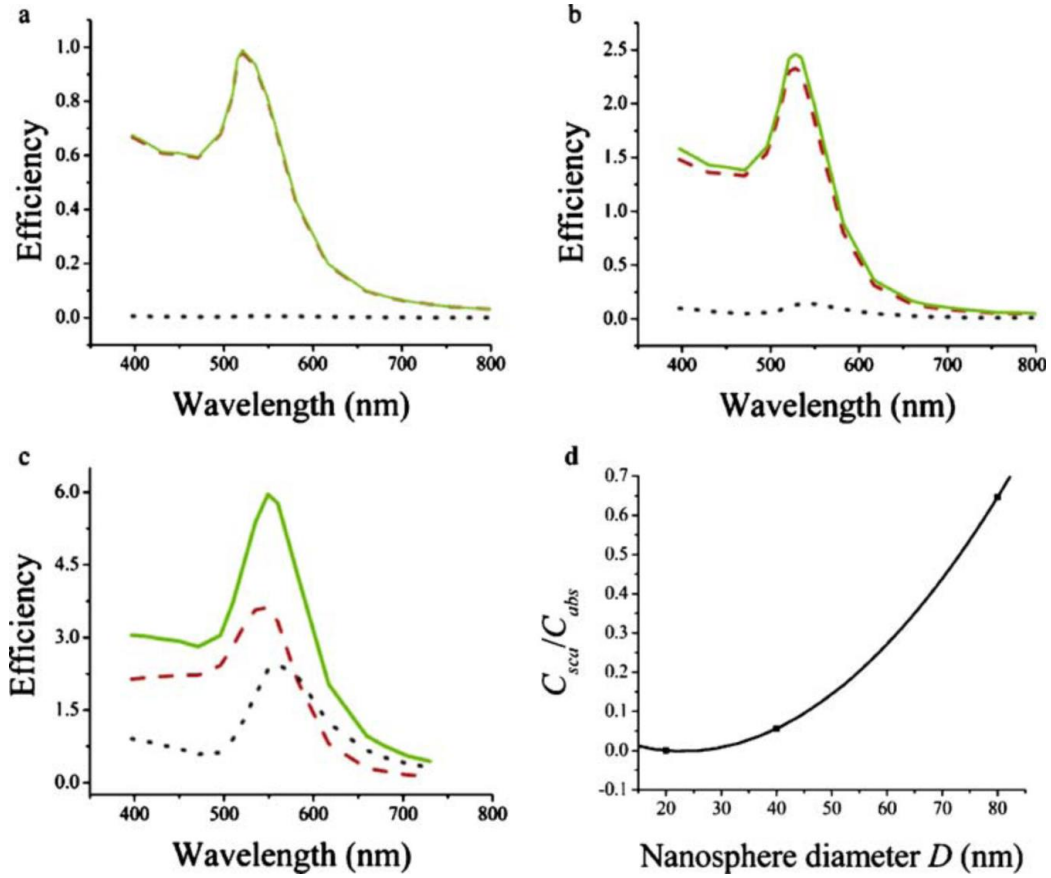

Figure 1.3. Mie theory absorption (red dashed curve), scattering (black dotted curve) and extinction (green solid curve) spectra of spherical Au nanoparticles of diameter **(a)** 20 nm, **(b)** 40 nm, and **(c)** 80 nm. Spectra are shown in terms of efficiency, i.e., the ratio of the calculated optical cross-section of the nanoparticle to the geometrical cross-section **(d)**. Ratio of scattering to absorption is as a function of Au nanosphere diameter.[42]

For nonspherical geometries, brute-force computational methods, such as the discrete dipole approximation (DDA)[46] and the finite-difference time domain (FDTD)[47,48] methods are widely used.

The recent discovery of single-molecule sensitivity of Raman scattering enhanced by resonantly excited metal nanoparticles has brought a renewed interest in surface-enhanced Raman scattering (SERS) and its application to molecular detection.[49–51] Noble metal nanoparticles, usually of Ag and Au, are well-known for their strong interactions with visible light through the resonant excitations of the collective oscillations of the conduction electrons within the particles. Since its discovery in 1974, the mechanism for SERS has been a matter of considerable debate.[37,52–54] It has been widely accepted that there are two mechanisms for the observed, and at times huge, enhancement in SERS: electromagnetic (EM) and chemical enhancement (CE) mechanisms. The EM mechanism is based on the interaction of the electric field of the surface plasmons with the transition moment of the adsorbed molecule, whereas the CE is based on the idea that mixing of molecular and metal states occur.

1.2.2 Biosensing technique using LSPR or SERS

Typically, a biosensor is a device comprising a biological recognition layer designed to bind a specific substance and a physical transducer that can translate the biochemical interaction into a quantifiable signal.[55] The recent progress in highly sensitive optical transducers combined with the exquisite specificity, affinity and versatility of biomolecular interactions has driven the development of a wide variety of optical biosensors with applications in diverse fields including clinical diagnosis, biomolecular engineering, drug design, environmental control or food industry.[55] It consists of 3 parts:[56]

- the sensitive biological element: biological material (e.g. tissue, microorganisms, organelles, cell receptors, enzymes, antibodies, nucleic acids, etc.), a biologically derived

material or biomimic. The sensitive elements can be created by biological engineering;

- the transducer or the detector element (works in a physicochemical way; optical, piezoelectric, electrochemical, etc.) that transforms the signal resulting from the interaction of the analyte with the biological element into another signal (i.e., transducers) that can be more easily measured and quantified;

- associated electronics or signal processors that are primarily responsible for the display of the results in a user-friendly way.[57] This sometimes accounts for the most expensive part of the sensor devices, however it is possible to generate a user friendly display that includes transducer and sensitive element.

An excellent example of biosensors is the home pregnancy test which shows how nano-properties of metal nanostructures can be used to provide practical solutions to real-world problems. The story behind some of the color change urine dipstick tests is related to the presence in pregnant women's urine of a significant excess of HcG, human gonadotropic hormone, which has a certain protein structure that binds to a complementary DNA base pair sequence.[55] That very specific complementary lock for the HcG key is attached to gold nanoparticles which reflect red light. If HcG is detected, the spot or line of the dipstick reflects red; if not, blue or clear or whatever the design entails.[55]

Although there are so many types of biosensors, we intend to mention about optical biosensors (or bioassays), utilizes unique LSPR or SERS properties of gold and silver nanoparticles, as most related to our research.

When metal nanostructures interact with a light beam, part of the incident photons are absorbed and part are scattered in different directions. Both absorption and scattering are greatly enhanced when the localized surface plasmon resonance (LSPR) is excited. Consequently, to detect the LSPR on metal nanostructure we use optical spectroscopy which

is generally based on extinction or scattering measurements. Extinction is often used to characterize systems containing a large amount of nanostructures, such as nanoparticle colloids. In the other hand, scattering measurements present a much lower signal-to-background ratio than extinction. Therefore, scattering detection is more interesting in samples with a low density of nanostructures, allowing the optical characterization of even single nano-objects.[55]

It is well established that the LSPR is strongly dependent on the dielectric properties of the local environment of the nanoparticles[44] including substrate, solvent, and adsorbates.[27,58,59] This dependence arises from the plasmon resonance condition[41] $\varepsilon_r = -2\varepsilon_m$. In the case of Au and Ag, the negative real part of the dielectric constant increases with increasing wavelength in the visible range.[60,61] An increase in dielectric constant ε_m of the surrounding medium is therefore reflected as a red shift in the LSPR band. This provides a very sensitive probe to detect small changes in the dielectric environment around the nanostructures, which is particularly attractive for sensing applications. Depending on the origin of LSPR changes, we can distinguish two types of sensors: aggregation sensors and refractive index sensors. The first group is based on the drastic color change induced in nanoparticles aggregates due to near-field electromagnetic coupling.[55] In general, for two metal nanoparticles, the resonance peak red-shifts when the inter-particle separation distance decreases below the particle diameter (Figure 1.4).[55] Thus, if two sets of metal nanoparticles are functionalized with complementary biomolecules, the biochemical interaction between them will induce the aggregation of the nanoparticles, which can be easily detected through the corresponding color change.[55]

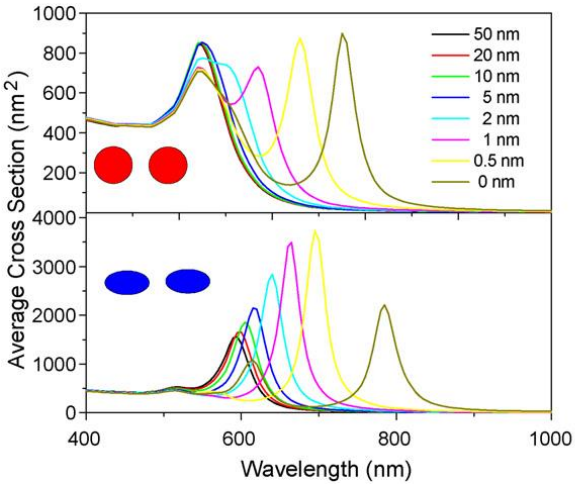

Figure 1.4. Red shift of the extinction cross-section of a pair of 20 nm gold spheres (upper panel) and ellipsoids with aspect ratio 2 (lower panel) as the separation distance between them is reduced (calculations based on the boundary element method).[55]

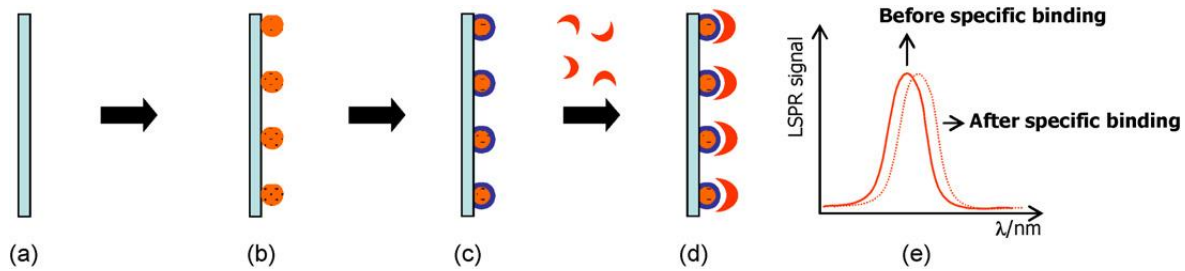

Figure 1.5. Schematic representation of the preparation and response of LSPR biosensors based on refractive index changes: (a) a substrate is chosen, (b) metal nanoparticles are attached to it by means of chemical linkers or prepared by nanolithography, (c) the metal particles are modified with the sensor moiety, (d) the analyte attaches from solution specifically onto the recognition function adsorbed onto the particles, causing a change in the refractive index around the particle resulting in an LSPR shift (e).[55]

The LSPR spectral position is highly dependent on the composition, size or shape of the nanoparticles, as well as the refractive index of the dielectric medium around them.[62] Size and shape dependence provides us with a wide spectral tenability along the whole visible and NIR spectrum, which is extremely useful to optimize surface enhanced effects, thermal treatments and also to maximize the biosensing response of the nanostructures. On the other

hand, the red-shift of the LSPR induced by a refractive index increase around metal nanostructures is the basis of the refractive index sensors.[55] Local refractive index changes such as those induced by biomolecular interactions at the surface of the nanostructures can be monitored via the LSPR peak shift (Figure 1.5).[55] Thus, by monitoring the LSPR wavelength λ_m by absorption or scattering-based techniques in response to adsorbate-induced changes in the local environment of the nanoparticle, a nanoscale chemical ore biosensor can be developed.[27,63]

In the case of extremely low analyte concentrations, e.g., sensing of pollutants or biological agents as DNA, extremely high analyte sensitivity is required.[42] This would require large changes in the LSPR wavelength in response to relatively small changes in the medium refractive index. The dependence of the LSPR sensitivity on the metal type and the nanoparticle shape has been discussed by Lee and El-Sayed.[61] Choosing a metal with a steeper wavelength dependence of the real part of the dielectric constant is expected to result in a higher LSPR sensitivity.[42] However, the choice of metals is limited to Ag and Au, both of which have a similar wavelength dispersion of the real part of the dielectric constant.[61]

Other appealing sensing schemes can be devised taking advantage of the extremely large electromagnetic fields created in the so-called "hot-spot", which occur within nanoparticle aggregates or at sharp edges and tips in single nanoparticles. Within these regions, the cross-section of inelastic optical processes can be amplified by many orders of magnitude, giving rise to surface-enhanced Raman scattering (SERS), surface enhanced fluorescence (SEF) and other related phenomena.[55] SERS can greatly benefit from the use of gold and silver nanoparticles in optical biosensors. For example, by using SERS for the output signal generation, in the case of silver-coated gold nanoparticles, the analytical signal increases by a factor of 10^{14}.[64,65]

1.3 Nanomaterials for biosensing and diagnostic applications

1.3.1 Noble metal nanoparticles

Noble metals are metals that are resistant to corrosion and oxidation; tend to be precious, often due to their rarity in the Earth's crust. The noble metals are usually considered to be ruthenium, rhodium, palladium, silver, osmium, iridium, platinum, and gold. Noble metal nanomaterials with interesting physical and chemical properties are ideal building blocks for engineering and tailoring nanoscale structures for specific technological applications.[66–70] Especially, the intense scattering and absorption of light from noble metal nanoparticles is the source of the beautiful colors in stained glass windows or artworks and has attracted the interest of scientists for generations.[29] Although scientists have learned that the characteristic hues of these noble metal nanoparticles suspensions arise from their strong interaction with light, the advent of the field of nanoparticle optics has allowed for a deeper understanding of the relationship among material properties (including chemical composition, size, and shape), local dielectric environments, and the observed color of a metal suspension.[39] An understanding of the optical properties of noble metal nanoparticles is of both fundamental and practical significance.[71] It helps to systematically explore the nanoscale structural and local environmental characteristics that cause optical property variation as well as provide access to regimes of predictable behavior.[72] Practically, the tunable photophysical attributes of metal nanocrystals,[73,74] their efficient addressability via optical and spectroscopic techniques, and rapid advances in nanoparticle synthesis and fabrication[75] have brought these nanostructures to the forefront of nanotechnology research directed toward applications ranging from photonics[76,77] to biomedicine,[12,15,28,78,79] such as surface-enhanced spectroscopy,[80] optical filters,[81] and sensors.[63]

The interesting optical attributes of metal nanoparticles, as reflected in their bright intense colors, are due to their unique interaction with light. In the presence of the oscillating

electromagnetic (EM) field of the light, the free electrons of the metal nanoparticle undergo a collective coherent oscillation with respect to the positive metallic lattice.[44,45] This process is resonant at a particular frequency of the light and is termed the localized surface plasmon resonance (LSPR) oscillation. This electronic oscillation can be simply visualized as a photon confined to the small size of the nanostructure, constituting an intense electric field around the particle. The surface plasmon oscillation decays by radiating its energy resulting in light scattering or decays nonradiatively as a result of conversion of absorbed light to heat.[42] The electric field intensity and the scattering and absorption cross-sections are all strongly enhanced at the LSPR frequency,[16] which for gold, silver and copper lies in the visible region. Since copper is easily oxidized, gold and silver nanostructures are most attractive for optical applications. Besides, they have many advantages such as easy synthesis in a wide range of sizes and shapes,[75] facile surface conjugation to a variety of chemical and biomolecular ligands,[82] biocompatibility,[83] and high chemical and photostability. Therefore, they become a novel class of optical and spectroscopic tags for biological sensing.[84–88]

1.3.2 Homogeneous and heterogeneous structure in multi-metallic nanoparticles

Nanosized bimetallic colloidal particles exhibit unique optical, electronic, magnetic, and catalytic properties[89–100] distinct not only from the bulk metals but also from the corresponding monometallic particles as well. Preparation and characterization of colloids of bimetallic nanoparticles were the subject of numerous papers, e.g. Au-Pt,[89] Ag-Pt,[89,90] and Ag-Au.[91–100] Nanoparticles composed of free-electron-like metals such as Ag and Au are known to provide strong resonance optical responses to irradiation by light,[74] which result in amplification of light-induced processes undergone by molecules localized on their surfaces, such as Raman scattering, giving rise to SERS.[37,101]

When nanoparticles are composed of various metals, both the composition and the actual

distribution will determine the resulting physicochemical properties, in particularly the optical properties.[62] We can define bimetallic nanostructure by the distribution modes of two elements into homogeneous (e.g. alloy, intermetallic) and heterogeneous (e.g core@shell, janus) structure. There are also some intermediate structures, such as partial alloy or partial segregation. In this section we will discuss about the strength and weakness of alloy and core@shell structure, in particularly for optical properties and biosensing applications.

Alloy structure is considered a solid mixture of various metals in one single nanoparticle. A fundamental problem in the theory and practice of alloy formation is the manner in which the microscopic crystal structures of alloys depend on the atomic properties and relative concentrations of the constituent elements.[102] Several physical factors which affecting the crystal structure of resulted alloy nanoparticles are the relative atomic sizes of the elements, the relative volume per valence electron in crystals of the pure elements, Brillouin-zone effects, and electrochemical differences between the elements.

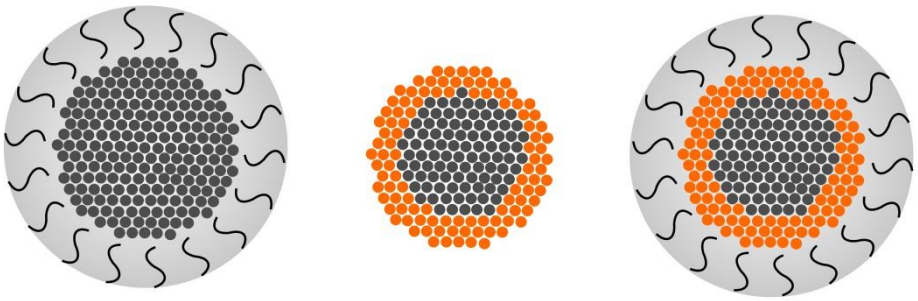

Scheme 1.2. Schematic illustration of several core-shell nanoparticles including a metallic core encapsulated in organic ligands (A), a metallic core encapsulated in a different metal (B), and a metallic core encapsulated in a different metal, protected by organic ligands (C).[104]

In the most general sense of the term, the core-shell nanoparticles are composed of a central "core" which can be a metal, metal oxide, or other material, and an outside "shell" of a

different substance, which surrounds the core.[4,103] This outside shell may be composed of adsorbed organic molecules that act as a protecting encapsulation, or the shell can be a metal or metal oxide that is different in composition to the core. For most instances the term "core shell nanoparticle" indicates a core and shell composed of different types of metals.[12,16] Scheme 1.2 shows some of the different types of nanoparticles that are composed of a core and a shell.[104]

Such nanoparticles are interesting because the use of an organic encapsulating shell allows the synthesis of nanoparticles with very well defined sizes, which leads to highly controllable properties for those particles.[105–109] In addition the surface capping protects the particle from aggregation during the synthesis process.[110–112] For metallic core and metallic shell nanoparticles, the use of different metals for each can lead to enhanced surface properties for catalysis, or electronic properties for applications in sensors or microelectronics, or bio-compatibility. The ability to control the composition of the core and shell allow the manipulation of the materials properties.[113,114] There are growing research interests in such core-shell nanoparticles because they are very attractive as advanced materials for many technological applications.[104]

In particular, bimetallic nanoparticles with a core@shell structure often exhibit improved physical and chemical properties[88,97,115,116] over their single-component counterparts due to the electric field enhancement, which is responsible for SERS enhancement.[117]

1.4 Chemical synthesis and preparation of nanoparticles for biosensing and diagnostic applications[104]

There are many routes to obtaining nanoscale materials. Nanoparticles may be synthesized in aqueous phase,[95,118–121] organic phase,[113,114,122–125] and produced by chemical reduction of transition metal salts,[126–129] thermal treatment,[130] seeded growth of particles,[131–

[137] or electrochemical reduction.[138] Nanoparticles can also be composed of many varied materials including pure metals,[111,112,126–128,139–146] alloyed metals,[100,147–149] metal oxides,[150–154] metal sulfides,[155] as well as non-metals such as carbon (buckminster fullerine and carbon nanotubes).[156] However one of the greatest challenges in synthesizing particles that are useful in high technology applications is the formation of materials with well-defined and uniform size as well as shape. There is a vast array of unique and interestingly shaped nanoparticles that have been formed including nanowires,[157–160] nanotubes,[161–163] nanorods,[164–168] nanotriangles, and nanocubes.[169,170] Even more interesting is the formation of particles with shapes such as dumbbells, stars, prisms, octahedral, wreaths, or flowers as well as many others.[171–182] These shapes may appear because of the action of a templating or directing agent, or because of natural growth of different crystalline faces of the particles.

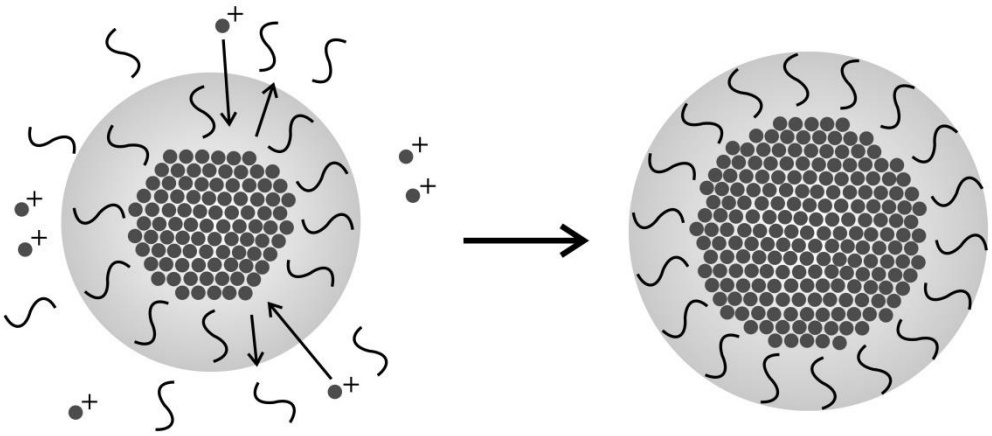

Scheme 1.3. An illustration of the formation of metal nanoparticles capped with an organic monolayer shell[104]

Nanoparticles that are synthesized in solution phase have some benefits over nanoparticles that are synthesized by precipitation or deposition methods.[183] When particles are synthesized in solution, it makes it possible to employ a capping agent and more closely

control the synthesis parameters such as feed concentration of metal precursor, or temperature of the reaction environment. By using an organic capping agent to protect the synthesized particles, very uniform sizes can be obtained because the organic capping agents adsorbed to the metal surface regulate the growth of the particles.[183] In this way the growth can be highly controlled by manipulating such parameters as the reaction temperature.[184–186] Scheme 1.3 shows the general process for surface capping desorption, particle growth, and surface capping re-adsorption during synthesis of the nanoparticles.

Another attractive feature of using organic capping species is the ability to exploit their properties to obtain shaped nanomaterials. In short, nanparticles have many well-defined faces such as the 111, 100, or 110 crystalline faces at their surface. Capping species will adsorb to these faces with differing strength depending on the ligand used, and the face it adsorbs to. Usually the capping agent adsorbs to the 100 face more strongly because that face is less saturated than the 111 face. Because of this, the 111 faces would have a greater chance to grow in size, and the 100 faces would grow more slowly. This difference in rates of growth of different faces of a single particle can lead to highly monodispersed and shaped nanoparticles.[130,187]

1.4.1 Synthesis in Organic Solutions[104]

There is a wide range of different synthesis techniques that may be carried out in organic phase.[110,125,146,148,187–190] This wide array of different synthesis techniques emerged because of the need to control the size, shape, and properties of the resulting particles. Some of the most widely used methods of synthesis are the Polyol process[110], and the synthesis of nanoparticles capped in alkylthiols.[148,191,192] However, organic solvent are always considered being less environmentally friendly than aqueous media. In addition, the treatment of nanoparticles surfaces which contains long chain molecule would be difficult and complicated for

biosensing applications. In the other hands, nanoparticles which are synthesized in aqueous have advantage of being able for directly used or applied in sensing processes.

1.4.2 Synthesis in Aqueous Solutions[104]

There is a wide range of different synthesis techniques that may be carried out in aqueous phase.[105–110,191–197] The most widely used method of synthesis for aqueous particles is discussed below.[194–196] In this synthesis technique, an organic ligand that is soluble in water must be chosen, as well as one that has a strong interaction with the surface of the metal particle. For example, in the case of synthesizing gold nanoparticles in water, citrate acts as a capping agent.[198] For this synthesis, the citrate also acts as the reducing agent to reduce Au(+3) to Au^0. Because the gold precursor salt is dissolved in boiling water during the synthesis of the particles, a very narrow size distribution of around 11 to 13 nm is obtained.[193,197,199] This synthesis method is of great interest to applications that require an aqueous environment. These particles are ideal for biological applications where the particles may be linked into functional structures using biological molecules such as many different amino acids (cysteine, homocysteine, glutathione), or even different types of DNA. Much interesting work has been done with aqueous gold nanoparticles in the fabrication of sensitive biological sensors that can detect specific markers for disease. The research performed by the Chad Mirkin group is an excellent example of this.[200–202] They have successfully made and employed biological molecule mediated nanosensors that can detect early stages of cancer and other disorders and that are much more sensitive than traditional sensing methods such as ELISA.[203] These advances allow for the early detection of diseases and a higher standard of treatment in medical situations. In addition this is made possible by the biocompatibility of gold with organic systems.[200–202] Gold nanoparticles could also be used to encapsulate a drug, or the drug could be adsorbed to the particle surface. Once in the body the medicine could be delivered directly to a target, speeding treatment and lowering

impact to the rest of the body. This is especially useful for cancer treatment as tumors or cancerous cells can be directly targeted without greatly affecting the rest of the body.[200–202]

In addition to all of the advantages of aqueous synthesis mentioned earlier, the formation process of metal nanoparticles capped with a monolayer shell of ligand (Scheme 1.2) allows the creation of continuous metallic atomic layers without including impurity, especially in the reaction at low temperature which is maximized at 100°C. For instance, the synthesis of silver nanoparticles in aqueous phase at refluxing conditions and using citrate reduction is based on the following reaction:[204]

$$C_6H_5O_7^{3-} + 2Ag^+ \rightarrow C_5H_4O_5^{2-} + H^+ + CO_2 + 2Ag^o \quad (1.5)$$

$$(C_5H_4O_5^{2-} = {}^-OOCCH_2COCH_2COO^-)$$

The resulting silver nanoparticles have been found to have no internal impurity.[204] Meanwhile, in order to incorporate carbon into nanoparticles, the reaction usually has to be carried out at high temperature, in organic solvent, or by a specific method such as chemical vapor deposition,[156] or spray pyrolysis apparatus.[205]

1.5 Characterization methods of metallic nanoparticles[104]

1.5.1 Spectroscopic methods

Raman spectroscopy is a vibrational spectroscopic technique that has been widely employed in the sensitive detection of organic molecules. The increase in the SERS intensity observed when samples are adsorbed on roughened surface has been reported by Van Duyne and co-workers.[206,207] The enhancement originating from the substrate is linked to the electronic properties of these precious metals. By coupling Raman active molecules, especially biomolecules to metal nanoparticles such as gold or silver, huge enhancement

factors are observed.[200–202] This technique has found very promising applications in bioassay, and the detection of very complex molecules and systems including that for specific sequences of DNA or protein chains.[200–202] In addition, Raman active molecules that are attached to nanoparticles can be used to label non-active biomolecules in-situ, thereby allowing scientists to track complex biological reactions and their products. Recently, Mirkin et. al. has reported their work involving the monitoring of the complementary binding of DNA labeled nanoparticles. In this work they showed that the association of complementary DNA molecules could be monitored using SERS where silver nanoparticles served as the enhancing substrate.[201]

X-ray photoelectron spectroscopy has been extensively used to characterize nanoparticles because of the high sensitivity of the technique.[208] For example, XPS has been used to determine the oxidation states of nanomaterials, elucidating whether the particle is an oxide particles, or pure metal samples were synthesized.[105–109,208] XPS has also been utilized to examine the relative concentrations of metals in a sample, and whether or not the sample is alloyed or phase segregated.[105–109,208] XPS also provides information about the adsorbed surface species on the metal nanoparticles. By examining the binding energy of the peaks in the XPS spectrum, a large amount of information can be found. Not only is the chemical identity of any adsorbed species be found, the interaction between the adsorbed species and the metal surface (i.e. gold-thiolate bonding) can be obtained.[105–109,208] These chemical identifications make XPS an indispensable technique in the analysis of nanomaterials.

Ultraviolet-visible spectroscopy is a molecular absorption spectroscopy that is very useful for studying the optical properties of metal nanoparticles. UV-Vis is mostly known for its use in studying the electronic transition of a molecule. In our study, we have employed UV-Vis to aid our analysis in the surface plasmon resonance (SP) resonance band of the nanoparticles and its assemblies. Some metal nanoparticles display a surface plasmon resonance band,

which occurs when the surface electrons oscillate at a specific electromagnetic wavelength.[193,197] While many metals display the surface plasmon resonance band, several do not fall within the visible range, and cannot be easily measured using UV-Vis. The metals gold, platinum, and silver all have distinct surface plasmon resonance bands. For example, gold nanoparticles exhibit a SP band around 520nm.[199] Both the intensity and width of the band depend on the size of the particles. A narrow band denotes a very monodispersed particle size distribution, while a broad band indicates non-uniformly sized particles. The position of the band is also dependent on particle size, with small particles having a peak position at shorter wavelength, and larger particles showing a longer wavelength. For gold nanoparticles smaller than ~ 5 nm, the SP band is rather weak due to the damping of the electrons on the metal surface.[193] The intensity of the band can also be used to determine the concentration of the sample using Beers law.[193,197,199]

The monitoring of the change in surface plasmon resonance band can provide information on the assembly of metal nanoparticles. For molecularly-mediated assembly of gold nanoparticles in solution to form structures of arrayed particles, the surface plasmon resonance band shift to longer wavelength due to a change in interparticle spatial properties of the assemblies.[193,197,199]

1.5.2 Microscopic methods

There are several microscopic methods for characterizing nanoparticles such as transmission electron microscopy (TEM), high resolution transmission electron microscopy (HR-TEM) and scanning transmission electron microscopy (STEM). For example, TEM has been used to reveal nanoparticles of different sizes with different shapes such as spherical shape,[95,118–121,209] cube shape,[169,170] or star shape.

TEM has been used extensively in the characterization of the size and shape of

nanoparticles.[105–109] TEM is an ideal technique because it allows the direct visualization of the size and shape of the synthesized particles. By casting the transmitted electrons from a sample onto a fluorescent screen, we can see an image that is made possible by the smaller wavelength that electrons possess.[210] Information regarding the crystalline facets of individual particles and the interparticle distance between neighboring particles can be obtained. This gives indirect information about the identity of capping species on the particles. In addition, high resolution TEM is used extensively to determine the interatomic distances for atoms within individual nanoparticles. This can be used to determine if a particle is composed of a monotamic species or if it is an alloy.[210] Different types of particles such as core-shell particles can also be studied using this technique because the different materials transmit the electron beam to different degrees. It is thus possible to determine if a particle is composed of a core and shell of different materials.[211]

1.5.3 Crystallography

X-ray diffraction is especially useful in the analysis of nanomaterials and nanoparticles because of the two primary types of information that can be obtained with the technique. The first type of information that XRD can elucidate is the composition of metal nanoparticles and alloys of metal nanoparticles.[8,146,212] The location of each line in an XRD spectrum is indicative of the spacing between crystalline faces in the material, for metal nanoparticles this means that we can determine the identity of the metal being analyzed because we can determine the lattice parameter in our particle. In addition we can determine the relative ratios of metals in a bimetallic sample by deducing the lattice parameter, because the lattice parameter reflects the average values of both metals in the bimetallic sample.

The second type of information that can be provided by XRD is the crystal size of the particle. Because the line width of the peaks observed in XRD spectra is dependent on the crystal sizes in the sample we can determine the particle size (if each particle is a single well

defined crystal) using the Scherrer equation (Equation 4.1). Typically the peak width at half height is used for the calculation. In general, the smaller the particles, the wider the peak width is. Very large particles will give a very narrow peak in the XRD spectrum.

XRD techniques have been used to determine alloy and phase properties of bimetallic gold platinum particles,[213,214] size and shape of various metal particles,[105–109,215] as well as composition, oxidation state, or lattice parameter for nanoscale materials.[213–215]

1.6 Research objective

As mentioned above, gold (Au) and silver (Ag) nanoparticles have novel optical properties that make them ideal candidates for use as probes in biosensing and diagnostics applications. However, nanoparticles for biosensors must be prepared in a way that ensures reproducibility and monodispersity in size, shape, composition and structure. Also, the nanoparticles must be stable against degradation and leaching.[55] Silver nanoparticles have exceptionally high extinction coefficient associated with very high enhancement ability in Raman spectroscopy, which has led to their use as sensing agents in several biological applications, such as the detection of proteins, amino acids, or DNA.[86,88] Despite the promising properties displayed by Ag nanoparticles though, there have been several difficult challenges to address, namely the ability to synthesize Ag nanoparticles in aqueous phase with a desired size, shape or monodispersity,[216] and the ability to associate the resulting Ag particles with the desired biomolecules so that the detection can be performed.[86] Ag metal exhibits a weaker affinity for biomolecules containing sulfur compared with Au, which has very strong affinity for sulfur and sulfur-containing molecules.[86,88] Besides, Au nanoparticles have high resistance to oxidation. In light of this, many researchers have attempted to couple Ag and Au nanoparticles in a core@shell (Ag@Au) structure where the core Ag provides ideal optical properties and the Au shell imparts chemical stability and reactivity with sulfur

containing biomolecules.[101,117] In addition, gold and silver metals have a closely matched lattice parameter[86] which reduces lattice strain at the Ag-Au interface and facilitates formation of a bimetallic structure. Despite the multitude of attempts to synthesize aqueous Ag@Au nanoparticles, few attempts have succeeded in producing monodisperse nanoparticles in terms of size, shape and most importantly structure. The challenges associated with synthesizing Ag@Au particles primarily stems from the galvanic replacement reaction that occurs between aqueous gold and metallic silver during the shell deposition procedure.[217,218] In fact, galvanic replacement has been extensively utilized to generate novel nanoparticle structures including hollow metal particles, or gold nano-cages.[52,53] The galvanic replacement reaction between Ag nanoparticles and Au ions is expressed as[70]

$$3Ag(s) + HAuCl_4(aq) \rightarrow Au(s) + 3AgCl(s) + HCl(aq) \quad (1.6)$$

To synthesize monodispersed Ag@Au nanoparticles the galvanic replacement reaction should be suppressed or eliminated. In our previous work we used a technique where additional reducing agent is added in tandem with Au precursor to minimize the etching of the Ag cores during the coating process.[219] While the galvanic replacement reaction was partially suppressed, the resulting Ag@Au nanoparticles still had gaps in the gold shell or hollow sections at the interface of the core and shell.[220] Due to the galvanic replacement reaction between Au ions and the Ag metal cores, it is still a challenge to synthesize well-defined and uniform Ag@Au nanoparticles with no defects in the structure such as gaps in the gold shell, or void spaces within the core area.

It has been reported that a charge compensation mechanism leads to a depletion of d electrons at the Au site accompanied by an increase in d electrons at the Ag site in the Au-Ag alloy.[221,222] Ag atoms vapor-deposited onto a Pt(111) surface were found to increase d electron populations as indicated by the negative shift in the Ag $3d_{5/2}$ binding energy (BE).[223]

Small Pt nanoparticles dispersed on the surfaces of alkali metal titanate nanotubes ($M_2Ti_3O_7$, M = Li^+, Na^+, and K^+) exhibited a negative shift in the Pt 4f BE due to an electron donation from titanate nanotubes to Pt nanoparticles yielding a negative Pt oxidation state.[224] Based on these results, we first synthesized monodispersed Au seeds, and then, deposited a Ag shell onto the Au seeds to form uniform Au@Ag core@shell nanoparticles via seed-mediated growth. It is expected that the electronic and chemical properties of the Ag shell can be tuned by coupling the Ag shell to the Au core due to a charge transfer that increases electron density within the Ag shell yielding a negative Ag oxidation state which may suppress the galvanic replacement reaction at the Ag shell surface. Subsequently, we further deposited a Au second shell onto the Au@Ag nanoparticles to form defect-free (Au@Ag)@Au double shell nanoparticles taking advantage of the suppressed galvanic replacement reactivity of the Ag intermediate shell. These results will be discussed carefully in chapter 3.

By extending this phenomenon to other silver based NP systems, insight can be gained into how to manipulate the particle structure and composition towards the desired characteristics. With this goal in mind, we attempt to make a series of different sized platinum particles and coat them in silver shells of various thicknesses. In this case, platinum was chosen as a core material because of its status as a noble metal, its *fcc* crystal structure (the same as for silver), and its chemical similarity to gold. The resulting particles were characterized in terms of their structural/composition properties, and then the electronic properties of these probes were analyzed by using X-Ray Photoelectron Spectroscopy. The results could demonstrate that the electronic transfer phenomenon can be extended to a wide range of heterostructure systems, and provides insight into how to exploit electronic transfer to create silver based sensing probes with enhanced robustness, high optical/plasmonic activity and plasmonic characteristics that can be tuned for a desired application (chapter 4).

Electron transfer or charge transfer phenomenon is very attractive as a route to

manipulate the properties of materials and also presents a complex challenge. Understanding the mechanism of operation and its effect to materials characteristics can lead us to systematically design materials with distinct characteristics for specific applications. My PhD research attempts to make clear the controllability of electron transfer phenomenon specifically in multi-metallic nanomaterials. In order to have the full picture of electron transfer phenomenon, we clarify the interaction among three noble metals (Ag, Au and Pt) by comparing Au-Ag, Pt-Ag and Au-Pt in homogeneous and heterogeneous nanostructure (chapter 5). This fundamental research will provide scientists with a useful tool in understanding, designing and controlling the properties of metallic nanomaterials. In addition, nanoparticles which are composed of Au, Ag or Pt are promising not only in biosensing and diagnostics applications but also are a good candidate for medical – therapy or catalyst applications.

1.7 References

(1) *Catalysis by metals and alloys*; Ponec, V.; Bond, G. C., Eds.; Elsevier, 1995.

(2) Love, J. C.; Estroff, L. A.; Kriebel, J. K.; Nuzzo, R. G.; Whitesides, G. M. *Chem. Rev.* **2005**, *105*, 1103.

(3) Faraday, M. *Phil. Trans. R. Soc. Lond.* **1857**, *147*, 145.

(4) *Nanoscale Science and Technology*; Kelsall, R.; Hamley, I.; Geoghegan, M., Eds.; John Wiley & sons, Ltd, 2005.

(5) Smart, L. E.; Moore, E. A. *Solid State Chemistry: An Introduction*; CRC Press: Florida, 2005.

(6) *Nanotechnology in Catalysis*; Zhou, B.; Hermans, S.; Somorjai, G. A., Eds.; Kluwer Academic/Plenum Publishers, 2004.

(7) *Nanomaterials: Synthesis, Properties and Applications*; Edelstein, A. S.; Cammaratra, R. C., Eds.; CRC Press, 1998.

(8) Maye, M. M.; Zheng, W.; Leibowitz, F. L.; Ly, N. K.; Zhong, C.-J. *Langmuir* **2000**, *16*,

490.

(9) Buffat, P.; Borel, J.-P. *Phys. Rev. A* **1976**, *13*, 2287.

(10) Palo, D. R.; Dagle, R. A.; Holladay, J. D. *Chem. Rev.* **2007**, *107*, 3992.

(11) Cameron, D.; Holliday, R.; Thompson, D. *J. Power Sources* **2003**, *118*, 298.

(12) Rosi, N. L.; Mirkin, C. *Chem. Rev.* **2005**, *105*, 1547.

(13) Ichiyanagi, Y.; Moritake, S.; Taira, S.; Setou, M. *J. Magn. Magn. Mater.* **2007**, *310*, 2877.

(14) Kannan, R.; Rahing, V.; Cutler, C.; Pandrapragada, R.; Katti, K. K.; Kattumuri, V.; Robertson, J. D.; Casteel, S. J.; Jurisson, S.; Smith, C.; Boote, E.; Katti, K. V. *J. Am. Chem. Soc.* **2006**, *128*, 11342.

(15) Jain, P. K.; El-Sayed, I. H.; El-Sayed, M. A. *Nano Today* **2007**, *2*, 18.

(16) Eustis, S.; El-Sayed, M. A. *Chem. Soc. Rev.* **2006**, *35*, 209.

(17) Cushing, B. L.; Kolesnichenko, V. L.; O'Connor, C. J. *Chem. Rev.* **2004**, *104*, 3893.

(18) Klotz, I. M. *Ligand-Receptor Energetics: A Guide for the Perplexed*; Wiley: New York, 1997.

(19) Thévenot, D. R.; Toth, K.; Durst, R. A.; Wilson, G. S. *Biosens. Bioelectron.* **2001**, *16*, 121.

(20) Mascini, M.; Palchetti, I.; Marrazza, G. *Fresenius J. Anal. Chem.* **2001**, *369*, 15.

(21) Natsume, T.; Nakayama, H.; Isobe, T. *Trends Biotechnol.* **2001**, *19*, S28.

(22) Kasemo, B. *Curr. Opin. Chem. Biol.* **1998**, *3*, 451.

(23) Lee, H. J.; Goodrich, T. T.; Corn, R. M. *Anal. Chem.* **2001**, *73*, 5525.

(24) Hall, D. *Anal. Biochem.* **2001**, *288*, 109.

(25) Wang, J.; Cai, X.; Rivas, G.; Shiraishi, H.; Farias, P. A. M.; Dontha, N. *Anal. Chem.* **1996**, *68*, 2629.

(26) Ebersole, R. C.; Miller, J. A.; Moran, J. R.; Ward, M. D. *J. Am. Chem. Soc.* **1990**, *112*, 3239.

(27) Haes, A. J.; Duyne, R. P. Van. *J. Am. Chem. Soc.* **2002**, *124*, 10596.

(28) Alivisatos, P. *Nat. Biotechnol.* **2004**, *22*, 47.

(29) Kerker, M. *J. Colloid Interf. Sci.* **1985**, *105*, 297.

(30) Alvarez, M. M.; Khoury, J. T.; Schaaff, T. G.; Shafigullin, M. N.; Vezmar, I.; Whetten, R. L. *J. Phys. Chem. B* **1997**, *101*, 3706.

(31) Link, S.; El-Sayed, M. A. *J. Phys. Chem. C* **1999**, *103*, 8410.

(32) El-Brolossy, T. A.; Abdallah, T.; Mohamed, M. B.; Abdallah, S.; Easawi, K.; Negm, S.; Talaat, H. *Eur. Phys. J. Spec. Top.* **2008**, *153*, 361.

(33) Collin, R. *Field theory of guided waves*; Wiley: New York, 1990.

(34) Ghosh, S. K.; Pal, T. *Chem. Rev.* **2007**, *107*, 4797.

(35) Ritchie, R. H. *Phys. Rev.* **1957**, *106*, 874.

(36) Barnes, W. L.; Dereux, A.; Ebbesen, T. W. *Nature* **2003**, *424*, 824.

(37) Moskovits, M. *Rev. Mod. Phys.* **1985**, *57*, 783.

(38) Rivera, V. A. G.; Ferri, F. A.; Jr., E. M. In *Plasmonics – Principles and Applications*; 2012; p. 285.

(39) Zhu, S.; Zhou, W. *J. Nanomater.* **2010**, *2010*, Article ID 562035.

(40) Lal, S.; Link, S.; Halas, N. J. *Nat. Photonics* **2007**, *1*, 641.

(41) Mie, G. *Ann. Phys.* **1908**, *25*, 377.

(42) Jain, P. K.; Huang, X.; El-Sayed, I. H.; El-Sayed, M. A. *Plasmonics* **2007**, *2*, 107.

(43) Klabunde, K. J. *Nanoscale materials in chemistry*; Wiley: New York, 2001.

(44) Kelly, K. L.; Coronado, E.; Zhao, L. L.; Schatz, G. C. *J. Phys. Chem. B* **2003**, *107*, 668.

(45) Jain, P. K.; Lee, K. S.; El-Sayed, I. H.; El-Sayed, M. A. *J. Phys. Chem. B* **2006**, *110*, 7238.

(46) Taton, T. A.; Lu, G.; Mirkin, C. A. *J. Am. Chem. Soc.* **2001**, *123*, 5164.

(47) Draine, B. T.; Flatau, P. J. *J. Opt. Soc. Am. A* **1994**, *11*, 1491.

(48) Futamata, M.; Maruyama, Y.; Ishikawa, M. *J. Phys. Chem. B* **2003**, *107*, 7607.

(49) Nie, S.; Emory, S. R. *Science (80-.).* **1997**, *275*, 1102.

(50) Kneipp, K.; Wang, Y.; Kneipp, H.; Perelman, L. T.; Itzkan, I.; Dasari, R. R.; Feld, M. S. *Phys. Rev. Lett.* **1997**, *78*, 1667.

(51) Xu, H.; Bjerneld, E.; Käll, M.; Börjesson, L. *Phys. Rev. Lett.* **1999**, *83*, 4357.

(52) Sandroff, C. J.; Weitz, D. A.; Chung, J. C.; Herschbach, D. R. *J. Phys. Chem.* **1983**, *87*, 2127.

(53) Voisin, C.; Fatti, N. Del; Christofilos, D.; Vallée, F. *J. Phys. Chem. B* **2001**, *105*, 2264.

(54) Campion, A.; Kambhampati, P. *Chem. Soc. Rev.* **1998**, 241.

(55) Sepúlveda, B.; Angelomé, P. C.; Lechuga, L. M.; Liz-Marzán, L. M. *Nano Today* **2009**, *4*, 244.

(56) Barbarisi, A.; Bechi, P.; Innocenti, P.; Redi, C. A.; Rosso, F. *Biotechnology in Surgery*; Italia, 2010; p. 67.

(57) Cavalcanti, A.; Shirinzadeh, B.; Zhang, M.; Kretly, L. C. *Sensors* **2008**, *8*, 2932.

(58) Ghosh, S. K.; Nath, S.; Kundu, S.; Esumi, K.; Pal, T. *J. Phys. Chem. B* **2004**, *108*, 13963.

(59) Malinsky, M. D.; Kelly, K. L.; Schatz, G. C.; Duyne, R. P. Van. *J. Am. Chem. Soc.* **2001**, *123*, 1471.

(60) Johnson, P. B.; Christy, R. W. *Phys. Rev. B* **1972**, *6*, 4370.

(61) Lee, K.-S.; El-Sayed, M. A. *J. Phys. Chem. B* **2006**, *110*, 19220.

(62) Liz-Marzán, L. M. *Langmuir* **2006**, *22*, 32.

(63) Haes, A. J.; Zou, S.; Schatz, G. C.; Duyne, R. P. Van. *J. Phys. Chem. B* **2004**, *108*, 6961.

(64) Kneipp, K.; Kneipp, H.; Itzkan, I.; Dasari, R. R.; Feld, M. S. *Chem. Rev.* **1999**, *99*, 2957.

(65) Fritzsche, W.; Taton, T. A. *Nanotechnology* **2003**, *14*, R63.

(66) Daniel, M.-C.; Astruc, D. *Chem. Rev.* **2004**, *104*, 293.

(67) Sau, T. K.; Rogach, A. L. *Adv. Mater.* **2010**, *22*, 1781.

(68) Tao, A. R.; Huang, J.; Yang, P. *Acc. Chem. Res.* **2008**, *41*, 1662.

(69) Murray, R. W. *Chem. Rev.* **2008**, *108*, 2688.

(70) Skrabalak, S. E.; Chen, J.; Sun, Y.; Lu, X.; Au, L.; Cobley, C. M.; Xia, Y. *Acc. Chem. Res.* **2008**, *41*, 1587.

(71) Stuart, D. A.; Haes, A.; McFarland, A. D.; Nie, S.; Van Duyne, R. P. *Plasmon. Biol. Med.* **2004**, *5327*, 60.

(72) Haes, A. J.; Stuart, D. A.; Nie, S.; Duyne, R. P. Van. *J. Fluoresc.* **2004**, *14*, 355.

(73) El-Sayed, M. A. *Acc. Chem. Res.* **2001**, *34*, 257.

(74) Bohren, C. F.; Huffman, D. R. *Absorption and scattering of light by small particles*; Wiley: New York, 1983.

(75) Burda, C.; Chen, X.; Narayanan, R.; El-Sayed, M. A. *Chem. Rev.* **2005**, *105*, 1025.

(76) Hutter, E.; Fendler, J. H. *Adv. Mater.* **2004**, *16*, 1685.

(77) Krenn, J. R.; Salerno, M.; Felidj, N.; Lamprecht, B.; Schider, G.; Leitner, A.; Aussenegg, F. R.; Weeber, J. C.; Dereux, A.; Goudonnet, J. P. *J. Microsc.* **2001**, *202*, 122.

(78) Aslan, K.; Lakowicz, J. R.; Geddes, C. D. *Curr. Opin. Chem. Biol.* **2005**, *9*, 538.

(79) El-Sayed, I. H.; Huang, X.; El-Sayed, M. A. *Nano Lett.* **2005**, *5*, 829.

(80) Haynes, C. L.; Mcfarland, A. D.; Zhao, L.; Duyne, R. P. Van; Schatz, G. C.; Gunnarsson, L.; Prikulis, J.; Kasemo, B.; Kä ll, M. *J. Phys. Chem. B* **2003**, *107*, 7337.

(81) Haynes, C. L.; Duyne, R. P. Van. *Nano Lett.* **2003**, *3*, 939.

(82) Katz, E.; Willner, I. *Angrew. Chem. Int. Ed.* **2004**, *43*, 6042.

(83) Connor, E. E.; Mwamuka, J.; Gole, A.; Murphy, C. J.; Wyatt, M. D. *Small* **2005**, *1*, 325.

(84) Lee, J.-S.; Stoeva, S. I.; Mirkin, C. A. *J. Am. Chem. Soc.* **2006**, *128*, 8899.

(85) Lim, D.-K.; Kim, I.-J.; Nam, J.-M. *Chem. Commun.* **2008**, 5312.

(86) Cao, Y.; Jin, R.; Mirkin, C. A. *J. Am. Chem. Soc.* **2001**, *123*, 7961.

(87) Wu, D.; Liu, X. *Appl. Phys. Lett.* **2010**, *97*, 061904.

(88) Cui, Y.; Ren, B.; Yao, J.-L.; Gu, R.-A.; Tian, Z.-Q. *J. Phys. Chem. B* **2006**, *110*, 4002.

(89) Liz-Marzán, L. M.; Philipse, A. P. *J. Phys. Chem.* **1995**, *99*, 15120.

(90) Torigoe, K.; Nakajima, Y.; Esumi, K. *J. Phys. Chem.* **1993**, *97*, 8304.

(91) Aihara, N.; Torigoe, K.; Esumi, K. *Langmuir* **1998**, *14*, 4945.

(92) Itakura, T.; Torigoe, K.; Esumi, K. *Langmuir* **1995**, *11*, 4129.

(93) Teo, B. K.; Keating, K.; Kao, Y.-H. *J. Am. Chem. Soc.* **1987**, *109*, 3494.

(94) Han, S. W.; Kim, Y.; Kim, K. *J. Colloid Interf. Sci.* **1998**, *208*, 272.

(95) Link, S.; Wang, Z. L.; El-Sayed, M. A. *J. Phys. Chem. B* **1999**, *103*, 3529.

(96) Freeman, R. G.; Hommer, M. B.; Grabar, K. C.; Jackson, M. A.; Natan, M. J. *J. Phys. Chem.* **1996**, *100*, 718.

(97) Rivas, L.; Sanchez-Cortes, S.; Garcı-Ramos, J. V.; Morcillo, G. *Langmuir* **2000**, *16*, 9722.

(98) Mallik, K.; Mandal, M.; Pradhan, N.; Pal, T. *Nano Lett.* **2001**, *1*, 319.

(99) Srnová-Šloufová, I.; Lednický, F.; Gemperle, A.; Gemperlová, J. *Langmuir* **2000**, *16*, 9928.

(100) Hostetler, M. J.; Zhong, C.-J.; Yen, B. K. H.; Anderegg, J.; Gross, S. M.; Evans, N. D.; Porter, M.; Murray, R. W. *J. Am. Chem. Soc.* **1998**, *120*, 9396.

(101) Srnová-Šloufová, I.; Vlčková, B.; Bastl, Z.; Hasslett, T. L. *Langmuir* **2004**, *20*, 3407.

(102) Denton, A. R.; Ashcroft, N. W. *Phys. Rev. A* **1991**, *43*, 3161.

(103) Wang, L.; Luo, J.; Maye, M. M.; Fan, Q.; Rendeng, Q.; Engelhard, M. H.; Wang, C.; Lin, Y.; Zhong, C.-J. *J. Mater. Chem.* **2005**, *15*, 1821.

(104) Mott, D. M. Synthesis, Characterization, and Catalysis of Metal Nanoparticles, State University of New York at Binghamton, 2008.

(105) Luo, J.; Maye, M. M.; Lou, Y.; Han, L.; Hepel, M.; Zhong, C.-J. *Catal. Today* **2002**, *77*, 127.

(106) Maye, M. M.; Kariuki, N. N.; Luo, J.; Han, L.; Njoki, P.; Wang, L.; Lin, Y.; Naslund, H. R.; Zhong, C.-J. *Gold Bull.* **2004**, *37*, 217.

(107) Maye, M. M.; Luo, J.; Lin, Y.; Engelhard, M. H.; Hepel, M.; Zhong, C. *Langmuir* **2003**, *19*, 125.

(108) Njoki, P. N.; Jacob, A.; Khan, B.; Luo, J.; Zhong, C.-J. *J. Phys. Chem. B* **2006**, *110*, 22503.

(109) Maye, M. M.; Luo, J.; Han, L.; Kariuki, N. N.; Zhong, C.-J. *Gold Bull.* **2003**, *36*, 75.

(110) Sun, S.; Murray, C. B.; Weller, D.; Folks, L.; Moser, A. *Science (80-.).* **2000**, *287*, 1989.

(111) Zamborini, F. P.; Gross, S. M.; Murray, R. W. *Langmuir* **2001**, *17*, 481.

(112) Jimenez, V. L.; Georganopoulou, D. G.; White, R. J.; Harper, A. S.; Mills, A. J.; Lee, D.; Murray, R. W. *Langmuir* **2004**, *20*, 6864.

(113) Kariuki, N. N.; Luo, J.; Hassan, S. A.; Lim, I.-I. S.; Wang, L.; Zhong, C.-J. *Chem. Mater.* **2006**, *18*, 123.

(114) Kariuki, N. N.; Luo, J.; Maye, M. M.; Hassan, S. A.; Menard, T.; Naslund, H. R.; Lin, Y.; Wang, C.; Engelhard, M. H.; Zhong, C.-J. *Langmuir* **2004**, *20*, 11240.

(115) Hao, E.; Li, S.; Bailey, R. C.; Zou, S.; Schatz, G. C.; Hupp, J. T. *J. Phys. Chem. B* **2004**, *108*, 1224.

(116) Yang, Y.; Nogami, M.; Shi, J.; Chen, H.; Ma, G.; Tang, S. *J. Phys. Chem. B* **2005**, *109*, 4865.

(117) Yang, Y.; Shi, J.; Kawamura, G.; Nogami, M. *Scr. Mater.* **2008**, *58*, 862.

(118) Mallin, M. P.; Murphy, C. J. *Nano Lett.* **2002**, *2*, 1235.

(119) Maxwell, D. J.; Emory, S. R.; Nie, S. *Chem. Mater.* **2001**, *13*, 1082.

(120) Njoki, P. N.; Luo, J.; Wang, L.; Maye, M. M.; Quaizar, H.; Zhong, C.-J. *Langmuir* **2005**, *21*, 1623.

(121) Liu, Q.; Guo, M.; Nie, Z.; Yuan, J.; Tan, J.; Yao, S. *Langmuir* **2008**, *24*, 1595.

(122) Lai, T.-L.; Lai, Y.-L.; Lee, C.-C.; Shu, Y.-Y.; Wang, C.-B. *Catal.Today* **2008**, *131*, 105.

(123) Toshima, N.; Ito, R.; Matsushita, T.; Shiraishi, Y. *Catal. Today* **2007**, *122*, 239.

(124) Tsai, S.-H.; Liu, Y.-H.; Wu, P.-L.; Yeh, C.-S. *J. Mater. Chem.* **2003**, *13*, 978.

(125) Shon, Y.-S.; Dawson, G. B.; Porter, M.; Murray, R. W. *Langmuir* **2002**, *18*, 3880.

(126) Zhao, S.-Y.; Chen, S.-H.; Wang, S.-Y.; Li, D.-G.; Ma, H.-Y. *Langmuir* **2002**, *18*, 3315.

(127) Sondi, I.; Goia, D. V.; Matijević, E. *J. Colloid Interf. Sci.* **2003**, *260*, 75.

(128) Yonezawa, T.; Onoue, S.; Kimizuka, N. *Langmuir* **2000**, *16*, 5218.

(129) Kapoor, S.; Joshi, R.; Mukherjee, T. *Chem. Phys. Lett.* **2002**, *354*, 443.

(130) Salzemann, C.; Lisiecki, I.; Urban, J.; Pileni, M.-P. *Langmuir* **2004**, *20*, 11772.

(131) Jana, N. R.; Gearheart, L.; Murphy, C. J. *Chem. Mater.* **2001**, *13*, 2313.

(132) Jana, N. R.; Gearheart, L.; Murphy, C. J. *Langmuir* **2001**, *17*, 6782.

(133) Orendorff, C. J.; Murphy, C. J. *J. Phys. Chem. B* **2006**, *110*, 3990.

(134) Murphy, C. J.; Sau, T. K.; Gole, A. M.; Orendorff, C. J.; Gao, J.; Gou, L.; Hunyadi, S. E.; Li, T. *J. Phys. Chem. B* **2005**, *109*, 13857.

(135) Gole, A.; Murphy, C. J. *Chem. Mater.* **2004**, *16*, 3633.

(136) Njoki, P. N.; Lim, I.-I. S.; Mott, D.; Park, H.-Y.; Khan, B.; Mishra, S.; Sujakumar, R.; Luo, J.; Zhong, C.-J. *J. Phys. Chem. C* **2007**, *111*, 14664.

(137) Sau, T. K.; Pal, A.; Jana, N. R.; Wang, Z. L.; Pal, T. *J. Nanopart. Res.* **2001**, *3*, 257.

(138) Ingham, B.; Illy, B. N.; Ryan, M. P. *J. Phys. Chem. C* **2008**, *112*, 2820.

(139) Libert, S.; Goia, D. V.; Matijevic, E. *Langmuir* **2003**, *19*, 10673.

(140) Kapoor, S.; Palit, D. K.; Mukherjee, T. *Chem. Phys. Lett.* **2002**, *355*, 383.

(141) Schmid, G.; Corain, B. *Eur. J. Inorg. Chem.* **2003**, 3081.

(142) Petroski, J. M.; Green, T. C.; El-Sayed, M. A. *J. Phys. Chem. A* **2001**, *105*, 5542.

(143) Kimling, J.; Maier, M.; Okenve, B.; Kotaidis, V.; Ballot, H.; Plech, A. *J. Phys. Chem. B* **2006**, *110*, 15700.

(144) Murphy, C. J.; Gole, A. M.; Hunyadi, S. E.; Orendorff, C. J. *Inorg. Chem.* **2006**, *45*, 7544.

(145) Tian, N.; Zhou, Z.-Y.; Sun, S.-G.; Ding, Y.; Wang, Z. L. *Science (80-.).* **2007**, *316*, 732.

(146) Mott, D.; Galkowski, J.; Wang, L.; Luo, J.; Zhong, C.-J. *Langmuir* **2007**, *23*, 5740.

(147) Demortière, A.; Petit, C. *Langmuir* **2007**, *23*, 8575.

(148) Brust, M.; Walker, M.; Bethell, D.; Schiffrin, D. J.; Whyman, R. *J. Chem. Soc., Chem. Commun.,* **1994**, 801.

(149) Zhang, X.; Zhang, F.; Chan, K.-Y. *Catal. Commun.* **2004**, *5*, 749.

(150) Panigrahi, S.; Kundu, S.; Ghosh, S. K.; Nath, S.; Praharaj, S.; Basu, S.; Pal, T. *Polyhedron* **2006**, *25*, 1263.

(151) Suh, W. H.; Jang, A. R.; Suh, Y.-H.; Suslick, K. S. *Adv. Mater.* **2006**, *18*, 1832.

(152) Azimirad, R.; Goudarzi, M.; Akhavan, O.; Moshfegh, A. Z.; Fathipour, M. *J. Cryst.*

Growth **2008**, *310*, 824.

(153) Song, X.; Sun, S.; Zhang, W.; Yin, Z. *J. Colloid Interf. Sci.* **2004**, *273*, 463.

(154) Meulenkamp, E. A. *J. Phys. Chem. B* **1998**, *102*, 5566.

(155) Tian, C.; Kang, Z.; Wang, E.; Gao, L.; Wang, C.; Xu, L.; Hu, C. *Mater. Lett.* **2005**, *59*, 1156.

(156) Veziri, C. M.; Pilatos, G.; Karanikolos, G. N.; Labropoulos, A.; Kordatos, K.; Kasselouri-Rigopoulou, V.; Kanellopoulos, N. K. *Microporous Mesoporous Mater.* **2008**, *110*, 41.

(157) Duan, J.-L.; Liu, J.; Yao, H.-J.; Mo, D.; Hou, M.-D.; Sun, Y.-M.; Chen, Y.-F.; Zhang, L. *Mater. Sci. Eng. B* **2008**, *147*, 57.

(158) Tao, C. G.; Cullen, W. G.; Williams, E. D.; Hunyadi, S. E.; Murphy, C. J. *Surf. Sci.* **2007**, *601*, 4939.

(159) Sun, Y.; Mayers, B.; Herricks, T.; Xia, Y. *Nano Lett.* **2003**, *3*, 955.

(160) Sun, Y.; Mayers, B. T.; Xia, Y. *Nano Lett.* **2002**, *2*, 481.

(161) Yu, X.; Cao, C.; An, X. *Chem. Mater.* **2008**, *20*, 1936.

(162) Yu, H.; Jin, Y.; Li, Z.; Peng, F.; Wang, H. *J. Solid State Chem.* **2008**, *181*, 432.

(163) Son, S. J.; Bai, X.; Nan, A.; Ghandehari, H.; Lee, S. B. *J. Control. Release* **2006**, *114*, 143.

(164) Robinson, R. D.; Sadtler, B.; Demchenko, D. O.; Erdonmez, C. K.; Wang, L.-W.; Alivisatos, A. P. *Science (80-.).* **2007**, *317*, 355.

(165) Tsuji, M.; Matsumoto, K.; Jiang, P.; Matsuo, R.; Tang, X.-L.; Kamarudin, K. S. N. *Colloids Surfaces A Physicochem. Eng. Asp.* **2008**, *316*, 266.

(166) Harichandran, G.; Lalla, N. P. *Mater. Lett.* **2008**, *62*, 1267.

(167) Murphy, C. J.; Gole, A. M.; Hunyadi, S. E.; Stone, J. W.; Sisco, P. N.; Alkilany, A.; Kinard, B. E.; Hankins, P. *Chem. Commun.* **2008**, 544.

(168) Gou, L.; Murphy, C. J. *Chem. Mater.* **2005**, *17*, 3668.

(169) Sun, Y.; Xia, Y. *Science (80-.).* **2002**, *298*, 2176.

(170) Petrova, H.; Lin, C.-H.; Hu, M.; Chen, J.; Siekkinen, A. R.; Xia, Y.; Sader, J. E.; Hartland, G. V. *Nano Lett.* **2007**, *7*, 1059.

(171) You, T.; Cao, G.; Song, X.; Fan, C.; Zhao, W.; Yin, Z.; Sun, S. *Mater. Lett.* **2008**, *62*, 1169.

(172) Zuo, F.; Yan, S.; Zhang, B.; Zhao, Y.; Xie, Y. *J. Phys. Chem. C* **2008**, *112*, 2831.

(173) Wang, H.; Schaefer, K.; Moeller, M. *J. Phys. Chem. C* **2008**, *112*, 3175.

(174) Zhong, Z.; Yin, Y.; Gates, B.; Xia, Y. *Adv. Mater.* **2000**, *12*, 206.

(175) Wang, X.; Li, Y. *Angew. Chem. Int. Ed.* **2003**, *42*, 3497.

(176) Liu, B.; Ren, T.; Zhang, J.-R.; Chen, H.-Y.; Zhu, J.-J.; Burda, C. *Electrochem. Commun.* **2007**, *9*, 551.

(177) Colder, A.; Huisken, F.; Trave, E.; Ledoux, G.; Guillois, O.; Reynaud, C.; Hofmeister, H.; Pippel, E. *Nanotechnology* **2004**, *15*, L1.

(178) Kim, D.; Park, J.; An, K.; Yang, N.-K.; Park, J.-G.; Hyeon, T. *J. Am. Chem. Soc.* **2007**, *129*, 5812.

(179) Wang, L.; Chen, D. *Mater. Lett.* **2007**, *61*, 2113.

(180) Zhen, L.; Wang, W. S.; Xu, C. Y.; Shao, W. Z.; Ye, M. M.; Chen, Z. L. *Scripta. Mater.* **2008**, *58*, 461.

(181) Bédard, M.; Skirtach, A. G.; Sukhorukov, G. B. *Macromol. Rapid Commun.* **2007**, *28*, 1517.

(182) Kim, J.-W.; Choi, S. H.; Lillehei, P. T.; Chu, S.-H.; King, G. C.; Watt, G. D. *Chem. Commun.* **2005**, 4101.

(183) Luo, J.; Han, L.; Kariuki, N. N.; Wang, L.; Mott, D.; Zhong, C.-J.; He, T. *Chem. Mater.* **2005**, *17*, 5282.

(184) Lang, H.; Maldonado, S.; Stevenson, K. J.; Chandler, B. D. *J. Am. Chem. Soc.* **2004**, *126*, 12949.

(185) Meyer, R.; Lemire, C.; Shaikhutdinov, S. K.; Freund, H.-J. *Gold Bull.* **2004**, *37*, 72.

(186) Kim, C. S.; Korzeniewski, C. *Anal. Chem.* **1997**, *69*, 2349.

(187) Lisiecki, I.; Sack-Kongehl, H.; Weiss, K.; Urban, J.; Pileni, M.-P. *Langmuir* **2000**, *16*,

8802.

(188) Bond, G. C.; Thompson, D. T. *Gold Bull.* **2000**, *33*, 41.

(189) Corti, C. W.; Holliday, R. J.; Thompson, D. T. *Gold Bull.* **2002**, *35*, 111.

(190) Luo, J.; Maye, M. M.; Kariuki, N. N.; Wang, L.; Njoki, P.; Lin, Y.; Schadt, M.; Naslund, H. R.; Zhong, C.-J. *Catal. Today* **2005**, *99*, 291.

(191) Brust, M.; Bethell, D.; Kiely, C. J.; Schiffrin, D. J. *Langmuir* **1998**, *14*, 5425.

(192) Baum, T.; Bethell, D.; Brust, M.; Schiffrin, D. J. *Langmuir* **1999**, *15*, 866.

(193) Lim, I.-I. S.; Ip, W.; Crew, E.; Njoki, P. N.; Mott, D.; Zhong, C.-J.; Pan, Y.; Zhou, S. *Langmuir* **2007**, *23*, 826.

(194) Enüstün, B. V.; Turkevich, J. *J. Am. Chem. Soc.* **1963**, *85*, 3317.

(195) Turkevich, J. *Gold Bull.* **1985**, *18*, 86.

(196) Turkevich, J. *Gold Bull.* **1985**, *18*, 125.

(197) Lim, I.-I. S.; Zhong, C.-J. *Gold Bull.* **2007**, *40*, 59.

(198) Pong, B.-K.; Elim, H. I.; Chong, J.-X.; Ji, W.; Trout, B. L.; Lee, J.-Y. *J. Phys. Chem. C* **2007**, *111*, 6281.

(199) Lim, I.-I. S.; Pan, Y.; Mott, D.; Ouyang, J.; Njoki, P. N.; Luo, J.; Zhou, S.; Zhong, C.-J. *Langmuir* **2007**, *23*, 10715.

(200) Lee, J.-S.; Ulmann, P. A.; Han, M. S.; Mirkin, C. A. *Nano Lett.* **2008**, *8*, 529.

(201) Cao, Y. C.; Jin, R.; Mirkin, C. A. *Science (80-.).* **2002**, *297*, 1536.

(202) Xu, X.; Han, M. S.; Mirkin, C. A. *Angew. Chem. Int. Ed.* **2007**, *46*, 3468.

(203) Hage, D. S. *Anal. Chem.* **1999**, *71*, 294R.

(204) Yang, Z.; Qian, H.; Chen, H.; Anker, J. N. *J. Colloid Interf. Sci.* **2010**, *352*, 285.

(205) Seo, J. Y.; Kang, H. W.; Jung, D. S.; Lee, H. M.; Park, S. Bin. *Mater. Res. Bull.* **2013**, *48*, 1484.

(206) *Handbook of Vibrational Spectroscopy*; Chalmers, J. M.; Griffiths, P. R., Eds.; Wiley: New York, 2002.

(207) Haynes, C. L.; Duyne, R. P. Van. *J. Phys. Chem. B* **2003**, *107*, 7426.

(208) Berg, C.; Venvik, H. J.; Strisland, F.; Ramstad, A.; Borg, A. *Surf. Sci.* **1998**, *409*, 1.

(209) Lu, X.; Imae, T. *J. Phys. Chem. C* **2007**, *111*, 8459.

(210) Bozzola, J. J.; Russell, J. D. *Electron Microscopy: Principles and Techniques for Biologists*; Jones and Bartlett Publishers: Boston, 1999.

(211) Guo, S.; Wang, E. *Anal. Chim. Acta* **2007**, *598*, 181.

(212) Schadt, M. J.; Cheung, W.; Luo, J.; Zhong, C.-J. *Chem. Mater.* **2006**, *18*, 4212.

(213) Mott, D.; Luo, J.; Njoki, P. N.; Lin, Y.; Wang, L.; Zhong, C.-J. *Catal. Today* **2007**, *122*, 378.

(214) Mott, D.; Luo, J.; Smith, A.; Njoki, P. N.; Wang, L.; Zhong, C.-J. *Nanoscale Res. Lett.* **2007**, *2*, 12.

(215) Luo, J.; Njoki, P. N.; Lin, Y.; Mott, D.; Wang, L.; Zhong, C.-J. *Langmuir* **2006**, *22*, 2892.

(216) Sharma, V. K.; Yngard, R. A.; Lin, Y. *Adv. Colloid Interface Sci.* **2009**, *145*, 83.

(217) Bi, Y.; Hu, H.; Lu, G. *Chem. Commun.* **2010**, *46*, 598.

(218) Pearson, A.; O'Mullane, A. P.; Bansal, V.; Bhargava, S. K. *Chem. Commun.* **2010**, *46*, 731.

(219) Mott, D.; Thuy, N. T. B.; Aoki, Y.; Maenosono, S. *Phil. Trans. R. Soc. A* **2010**, *368*, 4275.

(220) Mott, D.; Lee, J.; Thuy, N. T. B.; Aoki, Y.; Singh, P.; Maenosono, S. *Jpn. J. Appl. Phys.* **2011**, *50*, 065004.

(221) Tyson, C. C.; Bzowski, A.; Kristof, P.; Kuhn, M.; Sammynaiken, R.; Sham, T. K. *Phys. Rev. B* **1992**, *45*, 8924.

(222) Roy, R. K.; Mandal, S. K.; Pal, A. K. *Eur. Phys. J. B* **2003**, *33*, 109.

(223) Rodriguez, J. A.; Kuhn, M. *J. Phys. Chem.* **1994**, *98*, 11251.

(224) Hsu, C.-Y.; Chiu, T.-C.; Shih, M.-H.; Tsai, W.-J.; Chen, W.-Y.; Lin, C.-H. *J. Chem. Phys. C* **2010**, *114*, 4502.

Chapter 2. Experimental Details and Analysis Procedures

2.1 Chemicals and Materials

The chemicals used for all the experiments in this work are listed in alphabetical order (Table 2.1) and include the abbreviation if used in the text as well as the purity of the chemical in volume percentage, unless otherwise noted. Chemicals were obtained from Sigma-Aldrich; Tokyo Chemical Industry CO., LTD., Japan; Kanto Chemical Co., Inc., Japan; and Wako Pure Chemical Industries, LTD., Japan.

Table 2.1. List of chemicals, abreviations, and purity % used in the dissertation work.

Chemical	Abbreviation/ Formula	Purity %
3-Amino-5-mercapto-1,2,4-triazole	ATT/$C_2H_4N_4S$	95%
3-Aminopropyltrimethoxysilane	$C_6H_{17}NO_3Si$ or APTMS	97%
Acetone	C_3H_6O	99.5%
Chloroplatinic acid solution 8% wt.	H_2PtCl_6	—
Citric acid	$C_6H_8O_7$	99.5%
Gold (III) chloride trihydrate	$HAuCl_4.3H_2O$	99.9%
Hydrogen hexachloroplatinate (IV)	H_2PtCl_6 xH_2O	99.995%
L-ascorbic acid	$C_6H_8O_6$	99.5%
Methanol	C_2H_5OH	99.9%

Rhodamine 6G	R6G/$C_{28}H_{31}ClN_2O_3$	99%
Silver nitrate	$AgNO_3$	99.9%
Sodium acrylate	$C_3H_3O_2Na$	97%
Sodium borohydride	$NaBH_4$	98%
Sodium chloride	NaCl	99%
Sodium citrate tribasic dihydrate	$Na_3C_6H_5O_7.2H_2O$	99%
Sodium hydroxide	NaOH	98%
Sulfuric acid	H_2SO_4	95%

The materials used in the experiments conducted in this work are those that required refinement, further processing, or additional treatment before they could be used for experimentation. This section addresses those materials and the techniques with which they were treated.

Water was purified with a Millipore Milli-Q water system to obtain ultra pure water with a final resistance of at least 18.2 MΩ. Micro glass slides (76 x 26 mm, S111) were purchased from Matsunami glass Ind., LTD., Japan.

2.2 Synthesis and preparation of metal nanoparticles

All glassware used in the following procedures were cleaned by using aqua regia which was prepared by freshly mixing HCl and HNO_3 in a volume ratio of 3:1 respectively. After being soaked in aqua regia for 15 minutes, glassware were sonicated with soap in 15 minutes, followed by sonicating in distilled water for 30 minutes and rinsed thoroughly in Milli-Q grade water before experiments.

2.2.1 Au nanoparticles

Au nanoparticles were synthesized by the citrate-reduction of Frens.[1] The citrate ions were

used as a reducing agent, as well as a protective capping agent to stabilize the Au nanoparticles in the medium. Typically, an aqueous solution of $HAuCl_4$ (45 mL, 1.1 mM) was stirred vigorously in a 100 mL round bottom flask and heated to reflux at 100°C. Then, aqueous sodium citrate (5 mL, 37.9 mM) was rapidly injected in the flask. After the injection of sodium citrate, the color of reaction mixture changed from yellow to midnight-blue, and then gradually changed to deep-red, indicating the formation of Au nanoparticles. The whole reaction system was heated and refluxed for 60 minutes at 100°C, followed by being cooled naturally to room temperature.

2.2.2 Ag nanoparticles

The Ag nanoparticles were prepared by sodium citrate reduction of $AgNO_3$.[2] A solution of $AgNO_3$ (45 mL, 1.1 mM) was stirred in a 100 mL round bottom flask and purged with argon gas in 15 minutes. This solution was heated to reflux at 100°C, and then 5 mL of 6.8 mM sodium citrate solution was added. After 5 minutes of boiling, the color of the solution turned to yellow, and after 15 minutes it became opaque. The reaction solution was cooled to room temperature after 1 hour refluxing, and then the opaque dispersion was centrifuged at 4000 rpm for 30 minutes. After the centrifugation, the upper part of the solution became a transparent light-yellow color. This part contained the final Ag nanoparticles and was taken to a container for further experiments.

2.2.3 Au@Ag nanoparticles

Before being used to synthesize core@shell or double shell nanoparticles, the as-synthesized particles were purified to remove excess citrate, silver, gold, sodium, and other ions from the solution. Purification is performed by enveloping the particle solution inside a cellulose dialysis membrane with pore size of 10,000 Da and soaking in a distilled water bath. The water was changed every 12 hours for 24 hours.

Au@Ag core@shell nanoparticles were synthesized by the deposition of Ag on the Au cores.

40 mL of the dialyzed Au particles (8.05 x 10^{-9} M Au nanoparticles) are brought to reflux and purged with argon. 5 mL of a silver nitrate solution (ranging from 1.128 to 12.86 mM according to the thickness of the Ag shell desired) and 5 mL of a sodium citrate solution (13.6 mM) were added dropwise simultaneously. Different concentrations of $AgNO_3$ were used to control the Ag shell thickness of the resultant Au@Ag nanoparticles from 0.4 nm up to 3.6 nm. The solution color changed depending on the concentration of $AgNO_3$ added. The reaction mixture was then cooled to room temperature and purified to remove the excess ions.

2.2.4 (Au@Ag)Au double shell nanoparticles

(Au@Ag)@Au double shell nanoparticles were synthesized by carefully depositing Au on the Au@Ag nanoparticles which had 3.6 nm of Ag shell thickness. 40 mL of the dialyzed Au@Ag particles (4.03 x 10^{-9} M Au@Ag nanoparticles) are brought to reflux and purged with argon. 5 mL of $HAuCl_4$ solution (ranging from 0.3 to 3.91 mM according to the thickness of the second Au shell desired) and 5 mL of a sodium citrate solution (13.6 mM) were added dropwise simultaneously. The solution color changed depending on the concentration of $HAuCl_4$ added. The reaction mixture was then cooled to room temperature and contained in the vial.

2.2.5 Pt nanoparticles

A platinum suspension was prepared in aqueous solution following a multistep seed-mediated growth procedure by Bigall *et al.*.[3] Initially, small platinum seeds of 4.5 ± 0.7 nm in diameter were prepared. First, an 8% (by weight) chloroplatinic acid solution (0.086 mL) was added to boiling purified water (43.314 mL). After 1 minute, a solution (1.1 mL) containing 1% sodium citrate and 0.05% citric acid was added, followed half a minute later by a quick injection of a freshly prepared 0.08% sodium borohydride solution (5.5 mL) also containing 1% sodium citrate and 0.05% citric acid. After 10 minutes, the sol solution was cooled down to room temperature. The platinum seeds obtained here were used in preparing larger sized

platinum nanoparticles in further reaction steps. [3]

Larger sized platinum nanoparticles were prepared by adding the platinum seed solution (1 mL) to purified water (28.12 mL), 8% chloroplatinic acid solution, 25% citric acid solution (0.35 mL), and then 1.25% L-ascorbic acid solution (0.5 mL) containing 1% sodium citrate. The mixture was slowly heated to the boiling point and left to react for 30 minutes with stirring, and then cooled down to room temperature. The amount of chloroplatinic acid solution used in various reactions included 0.017, 0.03, 0.045 and 0.334 mL to obtain 25.7 ± 4.3, 31.3 ± 5.1, 39.8 ± 4.6 and 99.3 ± 3.7 nm platinum nanoparticles, respectively. The reaction products collected by centrifugation (centrifuge operated at 3,000–8,500 rpm depending on nanoparticle size) were washed three times with 0.5% sodium citrate solution, and then stored by dispersing in 0.5% sodium citrate solution.

2.2.6 Pt@Ag core@shell nanoparticles

The as-synthesized citrate-capped platinum nanoparticles were used as core particles in the preparation of Pt@Ag core@shell nanoparticles.[4] The platinum NP dispersion (20 mL) was brought to reflux with stirring until boiling, and then aqueous solution of $AgNO_3$ (5 mL) and sodium citrate (5 mL, 0.0086%) were simultaneously added dropwise. The reaction solution was refluxed for 20 minutes and then left to cool to room temperature. The silver shell thickness of Pt@Ag core@shell nanoparticles was controlled by increasing the concentration of $AgNO_3$ added in the reaction. To 25.7 nm platinum nanoparticles, an 8.1 nm Ag shell thickness was deposited by adding a 1.18 mM solution of $AgNO_3$. To 39.8 nm platinum nanoparticles, $AgNO_3$ concentrations including 0.17, 0.58, and 2.19 mM were used to prepare Ag shell thicknesses of 1.3, 5.2, and 9.1 nm, respectively.

2.2.7 Au@Pt core@shell nanoparticles

The as-synthesized citrate-capped gold nanoparticles (see section 2.2.1) were used as core particles in the preparation of Au@Pt core@shell nanoparticles. The gold nanoparticle

dispersion (20 mL) was brought to reflux with stirring until boiling, and then aqueous solution of H_2PtCl_6 8% and sodium citrate (5 mL, 0.0086%) were simultaneously added dropwise. The reaction solution was refluxed for 20 minutes and then left to cool to room temperature.

2.3 Characterization techniques

The analysis and characterization of the nanoparticles involved several instrumental techniques. The basic principles and measurement procedures for some of main instrumental techniques used in this work are briefly outlined in this section.

2.3.1 UV-Vis[5]

UV-Vis spectroscopy is a versatile technique that is most useful in the study of plasmonic nanoparticles. The technique relies on light in the visible to near UV region to promote the molecules in solution into electronically excited states. This causes the molecules to absorb the energy of the incident light of discrete wavelengths. A photodiode detector measures the spectrum of the light that passes through the sample. The spectrum elucidates the wavelengths of light that are absorbed by the sample.[6–10]

As the incident light interacts with the sample, there are many electronic transitions that can take place. One common one is the pi to pi* transition, although many other transitions take place. The ability of solutions to absorb light lends the technique to be used to quantitatively determine solution concentration using the Beer Lambert Law ($A = -Log_{10} (I/I_o) = \varepsilon \ell C$, where A is absorbance, I_o incident intensity, I is the transmitted intensity, ε is the extinction coefficient of the absorbing species, ℓ is the path length that the light must travel through the solution, and C is the concentration of the absorbing species. The Beer Lambert law has made possible the quantitative determination of concentration of absorbing solutions.[6–10]

For the studies conducted herein, UV-Vis spectra were acquired with a Perkin-Elmer

Lambda 35 UV-Vis spectrometer. A cuvet cell with a path-length of 1 cm was used and spectra were collected over the range of 300-1100 nm.

2.3.2 TEM[5]

Transmission electron microscopy heralded the first technique that could theoretically image at the atomic scale. Despite the theoretical projections, it took some years before TEM become refined enough to allow true atomic scale imaging. TEM now stands today as only one of two techniques that are capable of true atomic resolution.

TEM uses a stream of electrons, which have wavelengths smaller than individual atoms. The electron source in the TEM is a fine tungsten filament. When a current is passed through the filament, electrons begin to "boil" off. This stream of electrons must be controlled into a coherent beam, which is accomplished by using a series of magnetic "lenses". The magnetic lenses condense the stream of electrons down an evacuated metal cylinder and also make the beam coherent so that it may be focused. Next the beam is passed through a condenser aperture to help make the beam symmetrical. The sample is inserted into the path of the beam using a special holder that maintains the vacuum of the system. The electrons pass through the sample creating an image pattern, which strikes a phosphorescent screen. The phosphorescent screen illuminates under the electron pattern, which allows a visible image to be seen. To capture the image a camera underneath the phosphorescent screen opens up to capture the electron pattern on film. Scheme 2.1 shows the integral components of a basic TEM instrument. In today's new TEM instruments a digital camera instantly captures the image, replacing the older photo method.[11]

TEM has been extensively used to image biological samples and nanoscale materials. For biological samples, this is accomplished by completely freezing a tissue sample, creating a thin section by slicing the sample, then staining it to observe fine structure of the cell components. TEM is ideal for imaging nanoparticles of a wide range of sizes. The resolution limits of TEM allow for even the smallest of nanoparticles to be imaged with high resolution.

Inorganic nanoparticle samples may be prepared by casting the suspended particles onto a carbon-coated grid. Allowing the sample to dry creates a fine dispersion of particles over the carbon surface.

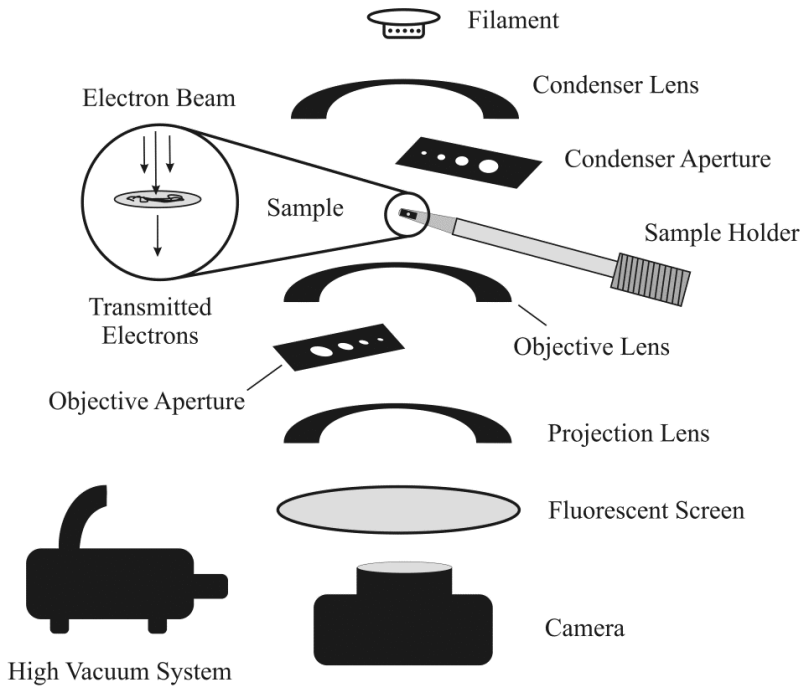

Scheme 2.1. Schematic illustration of the basic components of a TEM instrument.[5]

For our own studies, TEM was performed on an Hitachi H-7650 electron microscope (100 kV). For TEM measurements, samples were prepared by dropping the nanoparticle solution onto a carbon-coated copper grid followed by solvent evaporation in air at room temperature. The samples were imaged and processed using computer software to study the size and morphology of the particles.

2.3.3 XRD[12]

Diffraction occurs when waves scattered from an object constructively and destructively interfere with each other. For a fixed scatterer spacing, the angle will depend on the wavelength, with short wavelengths diffracting at higher angles than longer ones. A crystal structure is composed of a set of atoms arranged in a particular way, and a lattice exhibiting

long-range order and symmetry. Vectors and atomic planes in a crystal lattice can be described by a three-value Miller index notation *hkl*. The distance between two adjacent planes is given by the interplanar spacing d_{hkl} with the indices specifying the Miller indices of the appropriate lattice planes. Bragg diffraction is a consequence of interference between waves reflecting from different crystal planes. The condition of constructive interference is demonstrated in figure 2.1 and given by Bragg's equation:

$$n\lambda = 2d_{hkl}sin\theta \tag{2.1}$$

where λ is the wavelength of incident X-ray, θ is the angle of the diffracted X-ray, and n is an integer known as the order of diffraction. X-ray diffraction experiments are generally made at a fixed wavelength, thus a measure of the diffraction angles will allow the associated d-spacings to be calculated. X-radiation has wavelength of 0.1-100 Å which is close to the interplanar distance in a crystal and thus allows the crystal structure to diffract X-rays.

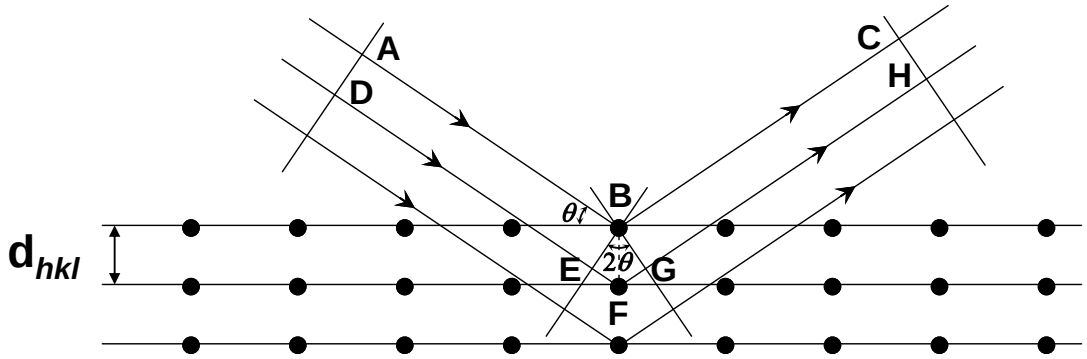

Figure 2.1. Diffraction of X-rays by a crystal

The basic components of an X-ray diffractometer are the X-ray source, specimen and X-ray detector (Figure 2.2) and they are all included in the circumference of a circle, which is called the focusing circle. The angle between the plane of the specimen and the X-ray source is θ, the Bragg angle. The angle between the projection of the X-ray source and the detector is 2θ. Therefore, the XRD patterns produced with this geometry are often known as θ-2θ scans.

The X-ray excitation source could be generated using Mo, Cu, Cr, etc. as a metal target anode. Cu is the most frequently used target. To obtain high-quality XRD data, one of the most important parameters is the method by which the analytical wavelength is treated. The difficulty in data treatment is the polychromatic nature of the diffracted beam and the variability in the angular dispersion of the diffractometer. Therefore, the monochromator is a very important component in a diffractometer. A monochromator is a single crystal which is commonly a quasi-single graphite crystal placed in the diffracted beam, in front of the detector. Placing the monochromator in the diffracted beam not only removes spectral impurities from the X-ray tube but also any fluoresced X-rays from the specimen.

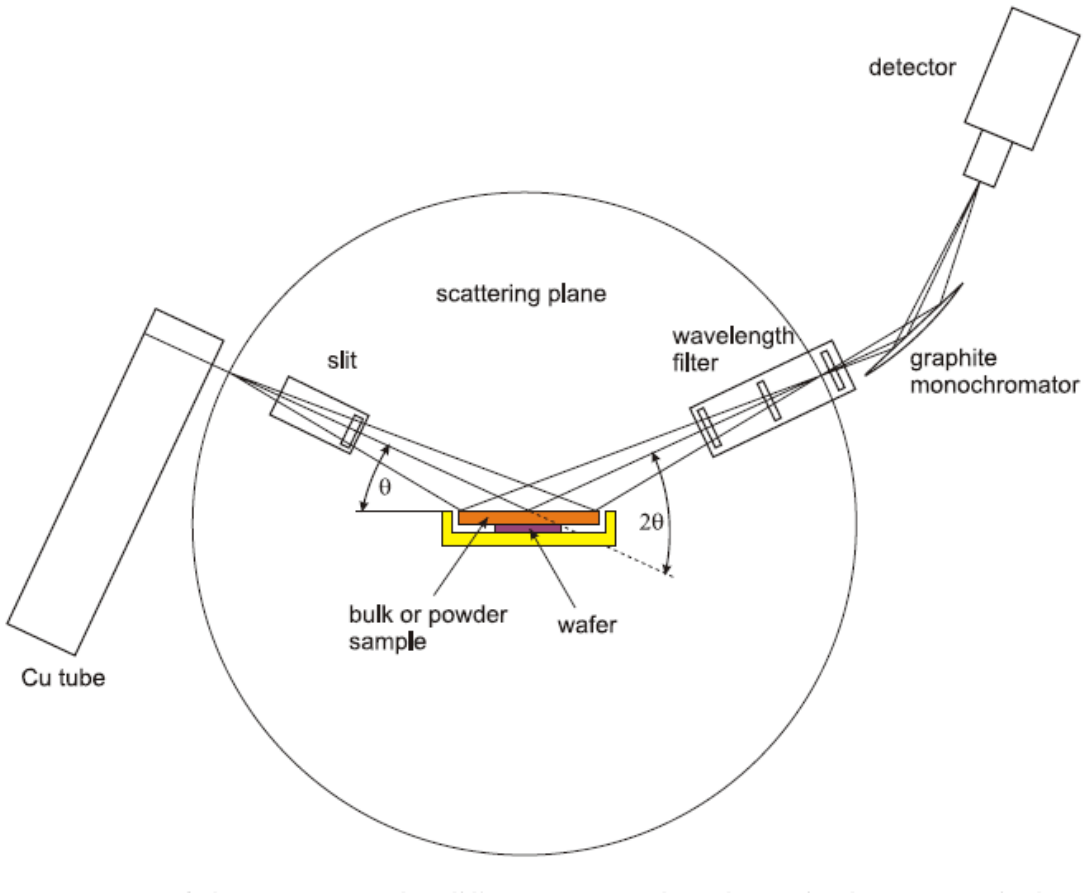

Figure 2.2. Schematic of a Bragg-Brentano parafocusing X-ray diffractometer[13]

For our analysis, XRD patterns were collected in reflection geometry using a Rigaku SmartLab X-ray diffractometer or a Rigaku MiniFlex 600 X-ray diffractometer at room

temperature with Cu K_α radiation (wavelength 1.542 Å, 40 kV, 30 mA).

2.3.4 XPS[12]

Basic principle

The fundamental principle of XPS is based on the photoelectron effect which was discovered by Heinrich Hert in 1887, and then was explained theoretically by Albert Einstein in 1905. The first high energy resolution XPS spectrum of cleaved sodium chloride (NaCl) was recorded in 1956 by Kai Siegbahn.[14] In 1981, Kai Siegbahn received the Nobel Prize to acknowledge his extensive efforts to develop XPS into a useful analytical tool.[15]

When an X-ray beam is directed to the sample surface, core electrons are liberated from the atoms of the sample as a result of a photoemission process. Each atom in the surface has core electrons with the characteristic binding energy of their particular element that is conceptually, but not strictly, equal to the ionization energy of that electron. The emitted electron has the kinetic energy of E_K and the binding energy E_B are given by the Einstein formula:

$$E_B = h\upsilon - E_K - \varphi \tag{2.2}$$

$$\varphi = E_F - E_V \tag{2.3}$$

where $h\upsilon$ is the X-ray photon energy; E_K is kinetic energy of the photoelectron, which can be measured by the energy analyzer; E_F and E_V are the energy of Fermi level and the vacuum level, respectively; and φ is the work function. Since φ can be compensated artificially (ca. 4~5 eV), it is eliminated, giving E_B (Scheme 2.2a).

Binding energy can also be described by Koopmans' theorem as below. If the energy of the atom's initial state changed, for example the increase or decrease of electron charge due to formation of a chemical bond with other atoms or the charge-transfer in a metallic interface, the E_B of electrons in that atom will change (Scheme 2.2b)

$$E_B = E_{final}(n-1) - E_{initial}(n) \quad (2.4)$$

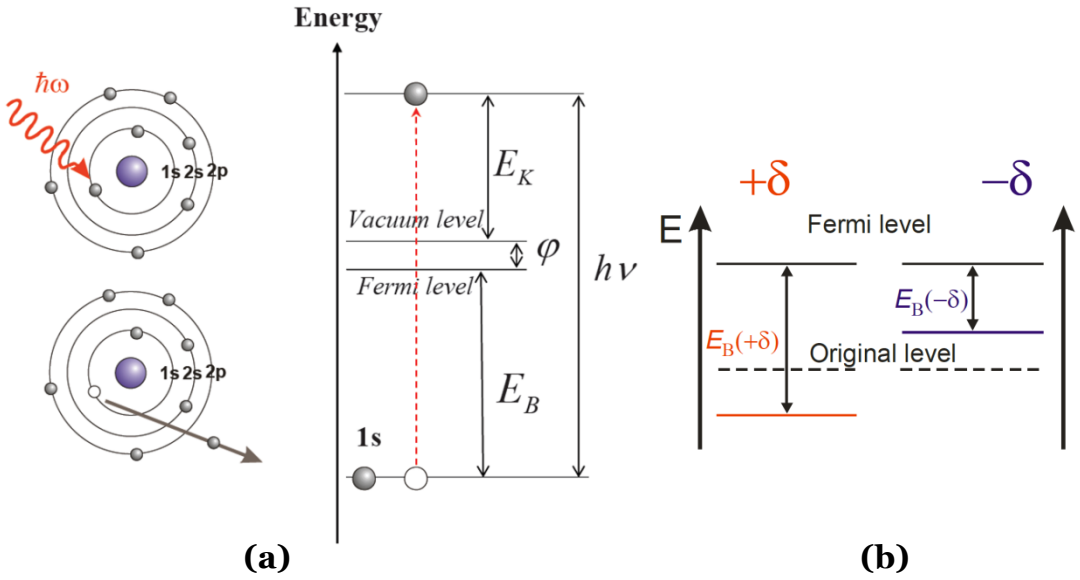

Scheme 2.2. (a) Illustration of XPS principles and (b) Illustration of the initial state effect

In Au-Cu alloy systems, charge-transfer has also been found to cause a shift in the Au 4f core level, which arises from changes in the one-electron energy and position of the Fermi level. This shift in the one-electron energy arises from Coulombic interaction while the Fermi level is affected by work function changes.[16] However, the value of E_B is considered the most direct signal of charge-transfer effect from the experimental results.

The XPS technique contains mainly the following parts: a primary X-ray source and electron energy analyzer, combined with a detection system and a sample stage, all contained within a vacuum chamber. The X-ray source, which provides photons, must have sufficiently high energy to excite intense photoelectron peaks from all elements of the periodic table. The most commonly applied configuration consists of a twin anode, providing monochromatic AlKα and MgKα lines. The electron spectrometer and sample room must be operating under ultra-high vacuum (UHV), usually ranging from 10^{-8} to 10^{-10} torr. UHV is required for detection of electrons and avoiding surface reactions or contamination. Because XPS is a surface sensitive technique, contaminates will produce an XPS signal and lead to incorrect

analysis of the surface composition. There are two common types of electron energy analyzer which measures the energy distribution of photoelectrons, namely the cylindrical mirror analyzer (CMA) and the concentric hemispherical analyzer (CHA). CMA is particularly suited to AES and older multitechnique instruments. CHA is now universally employed in high performance XPS instruments.

Spin-orbit coupling

In atomic physics, spin-orbit coupling describes a weak magnetic interaction, or coupling, of the particle spin and the orbital motion of the particle. One example is the electromagnetic interaction between the electron's spin and the electron's orbital magnetic moment. One of its effects is to separate the energy of the internal states of the atom. Based on the L-S coupling (Russel-Saunders coupling) approximation, we have $j = l+s$, where j is the total angular momentum quantum number, l is the orbit angular momentum quantum number, and s is the spin quantum number ($s = \pm 1/2$). To understand how spin-orbit coupling appears in XPS, for instance, here we analyze the inner core electronic configuration of the initial state of a silver atom:

Electron configuration of Ag: $(1s)^2(2s)^2(2p)^6(3s)^2(3p)^6(3d)^{10}(4p)^6(5s)^1(4d)^{10}$

The removal of an electron from the 3d subshell by photo-ionization leads to a $(3d)^9$ configuration for the final state. Because the d-orbitals ($l = 2$) have non-zero orbital angular momentum, there will be coupling between the unpaired spin and the orbital angular momenta. Therefore, when $l = 0$, there is a singlet XPS peak, and when $l > 0$, doublet XPS peaks (spin-orbit pairs) will be observed (Table 2.2).

Table 2.2. XPS Peak notation and peak area ratio based on spin-orbit coupling

Subshell	l	j	Peak area ratio
s	0	1/2	---
p	1	1/2, 3/2	1:2
d	2	3/2, 5/2	2:3
f	3	5/2, 7/2	3:4

Chemical shift

Core-electron binding energies are determined by electrostatic interaction between the electron and the nucleus. The electrostatic shielding of the nuclear charge from all other electrons in the atom (including valence electrons) will be altered by the removal or addition of electronic charge as a result of changes in binding energy. Therefore, E_b depends on chemical environment of atoms emitting the photoelectrons. For a simple example, E_b will be increased in the case of withdrawal of valence electron charge and decreased with addition of valence electron charge. Atoms of higher positive oxidation state exhibit a higher E_b due to the extra Coulombic interaction between photoelectron and the cation core. The ability to discriminate between different oxidation states and chemical environment is one of the major strengths of the XPS technique.

Surface charge effect

Sample surface electrons that are lost due to a photoemission process will increase in positive charge. This charging effect could cause a shift in peak position or sometimes the peak is lost entirely. Therefore metal or other conducting samples are usually grounded to the spectrometer for charge compensation. On the other hand, if the sample is a relatively poor conductor or an acceptable conductor but is electronically isolated from any conductive source, e.g., the spectrometer probe, by an effective sea of non-conductor material, the charge can be purposely compensated. For these cases, an axial electron gun in the CMA component of the XPS instrument works effectively to compensate charge for the sample. Even then, the

charging effect still occurs due to the photoelectron spectroscopy sampling depth or the depth of field of the neutralization device. If the sample has a non-uniform morphology (e.g. high roughness) including layered systems or clusters, the surface charging effect is also non-uniform and could cause a broadened peak. To avoid the peak shift caused by charging effect, carbon-tape is commonly used as a substrate for the deposition of samples. Carbon-tape is a good conductor and is thus less affected by the charging effect. During data analysis, the C 1s peak may be oftentimes used as a reference to calibrate the position of other element peaks in a sample.

Background subtraction

The XPS spectrum generally has a stair-case like shape because the background results from all electrons with initial energy greater than the measurement energy for which scattering events cause energy losses prior to emission from the sample. Moreover, during the photoemission process, excited electrons before escaping from the sample surface would collide with electrons of other atoms losing their kinetic energy. The photoelectrons that experienced collision will have lower kinetic energy than photoelectrons that did not experience collision, which contributes to the noise signal of the spectrum. The deeper relative position of a photoelectron from the surface the more difficult it is to escape from the sample due to the increasing chance of collision. Therefore, though the X-ray can penetrate into the sample surface on the order of μm, the XPS spectrum only contains information of the top 3-10 nm from the surface of the sample.

To subtract such a background from an XPS spectrum, we can use one of these methods: linear background subtraction method, Shirley method or Tougaard method. For the case of linear background subtraction method (Figure 2.3a), a straight line is draw from a point close to the peak on the low kinetic energy side of the peak to a point on the high kinetic energy side, and subtracted from the peak. Note that the binding energy becomes higher toward the left side of the horizontal axis. A problem with this method is that it is not highly accurate

since the peak area changes depending on the position of the chosen end points. For the case of the Shirley method (Figure 2.3b), the background intensity at any given binding energy is proportional to the integrated peak intensity in the binding energy peak range. The accuracy of this method is better than 5% and it's easy to use. The most accurate method is Tougaard background correction (Figure 2.3c). This is for integrating the intensity of the background at a given binding energy from the spectral intensities to higher binding energies, and it's particularly used in complicated numerous peak overlaps.

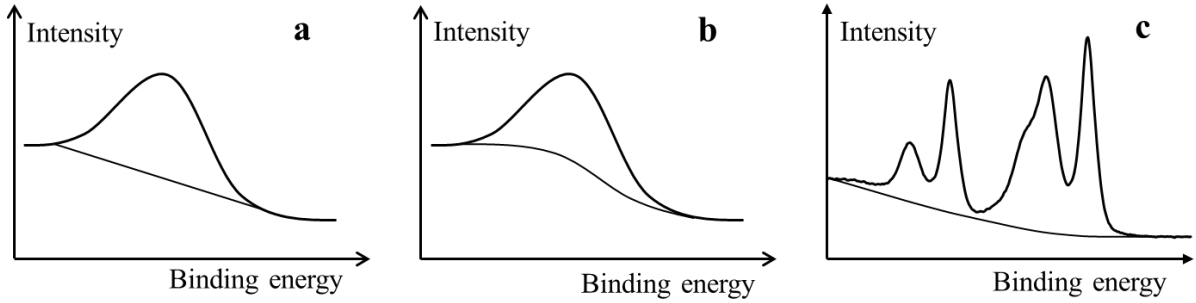

Figure 2.3. XPS background subtracted methods. (a) linear, (b) Shirley, and (c) Tougaard backgrounds

Quantification

The XPS peak intensity could be calculated by the equation below[17], for a given polar emission direction $\mu = \cos\theta$ (θ is scattering angle), primary flux F, analyser transmission T, detector efficiency D, analysed area A and signal electron production cross-section σ_{ex}.

$$I(\mu) = FTDA\Delta\Omega\sigma_{ex}\int_0^{\infty}\phi_0(z',\mu)c_0(z')dz' \qquad (2.5)$$

The atomic fraction of pure element A within the surface region, X_A, is related to intensity I_A and given by

$$X_A = \frac{\frac{I_A}{I_A^{\infty}}}{\sum_i \frac{I_i}{I_i^{\infty}}} \quad (2.6)$$

where I_i is measured intensity and I_i^{∞} is the sensitivity factor of the *i-th* element.[17]

Samples preparation and measurement conditions

XPS analysis in this research was carried out on a Shimadzu Kratos AXIS-ULTRA DLD high performance XPS system. Photoelectrons were excited by monochromated Al K_α radiation. Detection was done with a delay-line detector (DLD) and a concentric hemispherical analyzer (CHA). The X-ray tube was operated at 150W. The pass energy of the CHA was 20 eV for narrow-scan spectra. The analyzed area on the specimen surface was 300x700 μm^2 and was located in the center of the irradiated region. The instrument was operated at a vacuum level of $1x10^{-8}$ Torr. For the XPS sample preparation, the precipitated nanoparticles were deposited on a molybdenum substrate or carbon tape and dried in vacuum.

2.3.5 X-ray Absorption Spectroscopy (XAS: XANES and EXAFS)[12,18]

Basic Principle and Instrumentation

XAS techniques are closely related to other atomic absorption techniques such as XPS or Auger spectroscopy. The primary difference however is that in XAS analysis, the final state of all electronic transitions is collected, providing a high degree of specificity and sensitivity to the technique. During absorption processes, the wavelength of the X-rays is gradually decreased due to the increasing energy of photons; the absorption coefficient also decreases until it reaches a limit and suddenly enters into another absorption step. These discontinuities occur at the wavelengths where the energy of an absorbed photon corresponds to an electronic transition or ionization potential and appear in absorption spectra as a sharp edge which is the so called absorption edge (Figure 2.4). For example, the

highest energy edge corresponding to the ionization potential of a K electron is called the K edge. Each element on the periodic table has a set of unique absorption edges corresponding to different binding energies of its electrons. This gives XAS high elemental specificity.

XAS data are obtained by tuning the photon energy using a crystalline monochromator to a range where core electrons can be excited (0.1-100 keV photon energy). There are two main regions of data in a typical XAS generated spectrum. The strong oscillations which extend beyond the edge for about 30-40 eV is the so called X-ray absorption near edge structure (XANES) area and involve the multiple scattering of excited photoelectrons. The absorption spectrum beyond the XANES region is referred to as extended X-ray absorption fine structure (EXAFS). XANES and EXAFS stem from the same phenomenon. The difference between them is due to the kinetic energy of the photoelectron in each case. At a low energy, the mean free path is high, which induces an important multiple scattering effect. On the other hand, in the EXAFS region, the mean free path of the photoelectrons is limited, so single scattering is the main process observed.

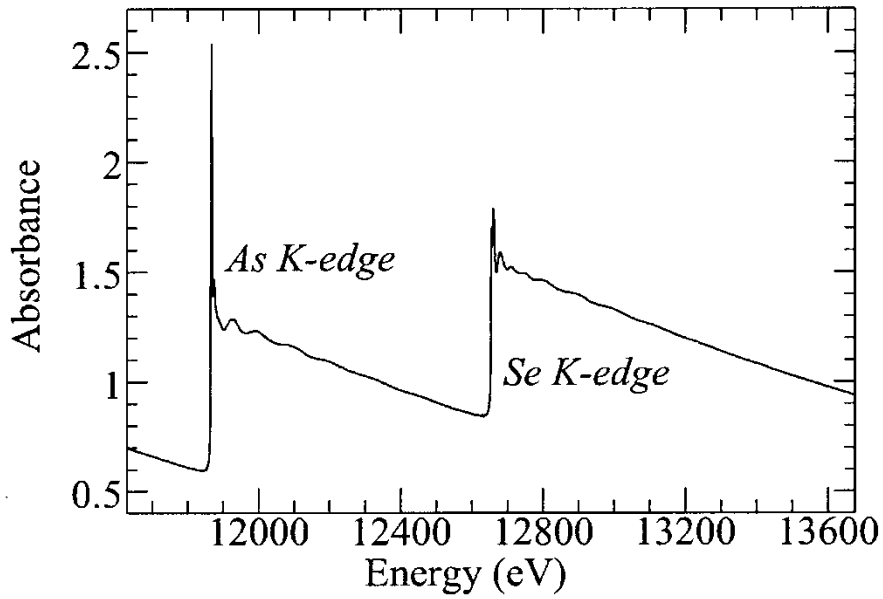

Figure 2.4. The K edge X-ray absorption spectra of As and Se.[19]

XANES

The near-edge structure in an X-ray absorption spectrum covers the range between the threshold and the point at which EXAFS begins. As mentioned above, the XANES regime is dominated by multiple scattering of the excited electrons which confers sensitivity to the details of the spatial arrangement of neighboring atoms, not only their radial distances but also the orientations relative to each other. XANES measurements may provide valuable information about the oxidation state, coordination environment, and bonding characteristics of specific elements in a sample.

EXAFS

EXAFS spectroscopy refers to the measurement of the X-ray absorption coefficient as a function of photon energy above the threshold of an absorption edge. EXAFS is the final state interference effect involving scattering of the outgoing photoelectron from the neighboring atoms. The regions of constructive and destructive interference are respectively seen as local maxima and minima giving rise to the oscillation in EXAFS. To represent the EXAFS region from the whole spectrum, a function χ can be defined in terms of the absorption coefficient μ as a function of energy

$$\chi(E) = \frac{\mu(E) - \mu_0(E_0)}{\mu_0(E)} \tag{2.7}$$

where E is the incident photon energy and E_0 is the threshold energy of a particular absorption edge. To relate $\chi(E)$ to structural parameters, energy E is necessary to be converted into the photoelectron wavevector k, and

$$\chi(k) = \sum_j N_j S_j(k) F_j(k) e^{-2\sigma_j^2 k^2} e^{-2r_j/\lambda_j(k)} \frac{\sin(2kr_j + \phi_{ij}(k))}{kr_j^2} \tag{2.8}$$

where $F_j(k)$ is the backscattering amplitude from each of the N_j neighboring atoms of the j-th type with a Debye-Waller factor of σ_j at distance r_j away; $\phi_{ij}(k)$ is the total phase shift

experienced by the photoelectron; e^{-2r_j/λ_j} corresponds to inelastic losses in the scattering process; $S_j(k)$ is the amplitude reduction factor due to many-body effects.[20] In order to complete the data extraction a Fourier transform of this expression is used to convert into frequency space, which results in a radial distribution function where peaks correspond to the most likely distances of the nearest neighbor atoms.

Instrumentation

XAS instruments are unlike other commercial instruments. The equipment must be assembled from multiple components to suit the needs of the experiment and may involve a significant amount of custom engineering. The typical XAS experiment at a synchrotron radiation source may include two main parts: the set of components which produce and deliver a controllable high intensity monochromatic X-ray beam and the set of instruments specific to the type of measurement, including sample handling, detectors, etc. The most unique point of the XAS instrument compared to other X-ray techniques is the synchrotron X-ray source. This makes the XAS an extremely sensitive measurement where the concentration of the absorbing element can be detected as low as a few ppm.

Sample preparations and measurement conditions[18]

Au $L_{2,3}$-edge XANES spectra were recorded at beam line BL01B1 of SPring-8. The photon energy was calibrated by the distinct peak in the differential spectrum of Au foil at the Au L_3-edge as 11.919 keV. The energy step of measurement in the XANES region was 0.3 eV. Both the ion-chambers were filled with N_2(85%)/Ar(15%) (I_0) and Ar (transmission mode), and the Lytle's detector was filled with Kr (fluorescence mode) and was operated at room temperature.

The nanoparticles were adsorbed onto a boehmite (Wako) substrate, diluted with boron nitride (Wako), grained and pressed to a pellet (10 mmφ) for XANES analysis. An Au foil was used as a reference for the bulk metallic Au. The obtained XANES spectra were analyzed

using the Rigaku REX2000 software (ver.2.5.7). The pre-edge background subtracted spectra were normalized to the edge jump at the center of EXAFS oscillation following a linear background subtraction, which was taken to the value of the atomic background at 13.815 and 12.050 keV, for the L_2- and L_3-edges, respectively. Estimation of the d-orbital electron density was carried out according to Mansour's method[21] as follows: The WL feature in the L_2-edge is related to the $2p_{1/2} \rightarrow 5d_{3/2}$ dipole-allowed transition while that of the L_3-edge is due to the $2p_{3/2} \rightarrow 5d_{5/2}$ and $5d_{3/2}$ dipole-allowed transitions, resulting from the spin-orbit interaction of the d states. Therefore, integration of these transitions reflects the number of holes in the $5d_{5/2}$ and $5d_{3/2}$ orbitals above the Fermi level as shown in figure 2.5.

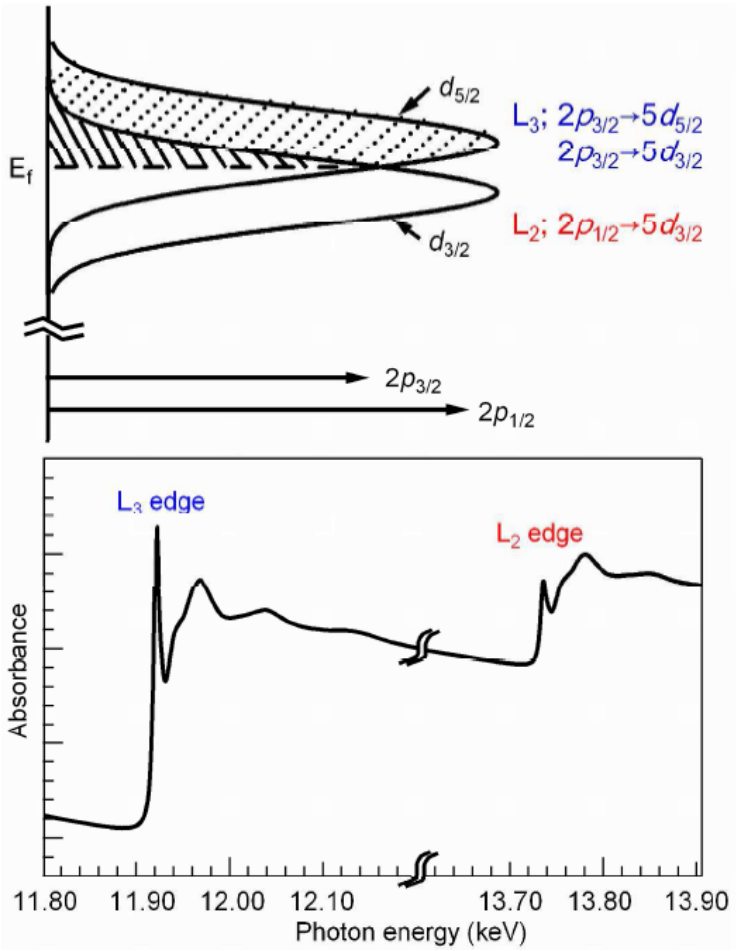

Figure 2.5. Schematic illustration of the Au $L_{2,3}$-edge XANES spectra and the corresponding electronic transition.[18]

Changes in the numbers of holes in the $d_{3/2}$ and $d_{5/2}$ orbitals from those of bulk Au, $\Delta h_{3/2} = h_{3/2,\mathrm{NP}} - h_{3/2,\mathrm{bulk}}$ and $\Delta h_{5/2} = h_{5/2,\mathrm{NP}} - h_{5/2,\mathrm{bulk}}$, were expressed as

$$\Delta h_{3/2} = \frac{3\Delta A_2}{C} \tag{2.9}$$

$$\Delta h_{5/2} = \frac{(2.25\Delta A_3 - 0.5\Delta A_2)}{C} \tag{2.10}$$

where $\Delta A_j = A_{j,NP} - A_{j,bulk}$ is the difference values between nanoparticles and bulk, and A_j is the edge area for the L_j-edge XANES spectrum (ev.cm^{-1}); C = 75213 eV.cm^{-1} is the characteristic constant of the absorption.[21,22]

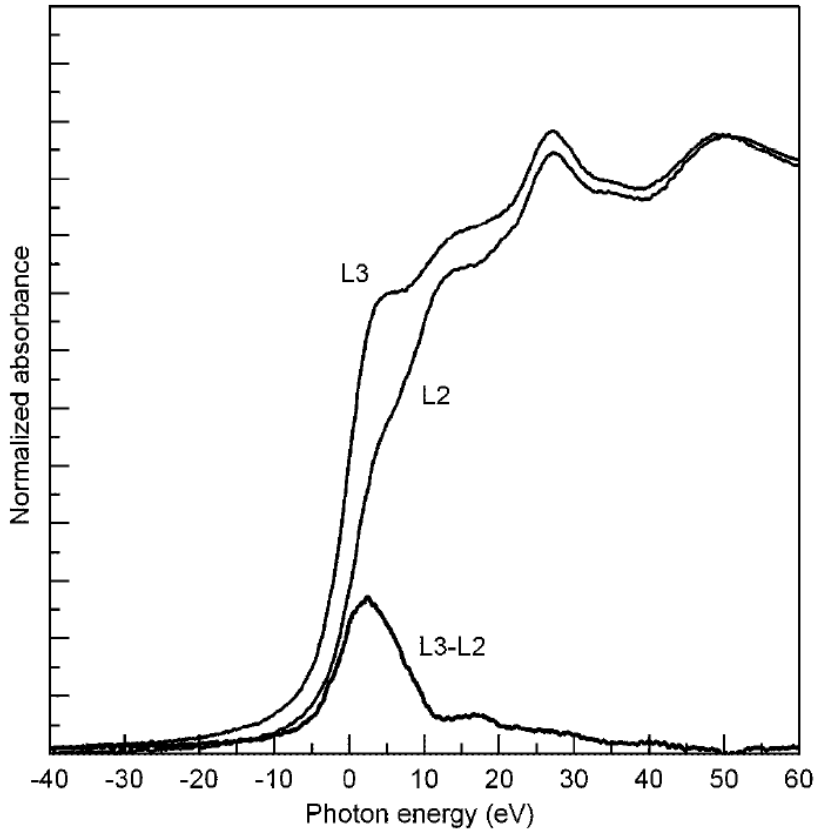

Figure 2.6. Au $L_{2,3}$-edge XANES spectra and the difference spectrum in the case of Au foil.[18]

The total width of the WL feature depends on the life time of the core hole, the experimental resolution, the dipole-transition matrix element, and the distribution of the

density of states of unoccupied d band at the Fermi level of the metal.[23,24] However, the first three factors can be considered to be uniform for the $L_{2,3}$-edge WLs.[23,24] To correlate the relative area of the WL to the d-electronic structure, the differences spectrum between the L_3- and the L_2-edge XANES spectra of the Au foil was plotted in figure 2.6.[18] A single distinct peak in the difference spectrum is observed in accordance with previous observations.[16] The area in the range from 10 eV below the X-ray absorption edge (E_0 = 0 eV) to 13 eV above the E_0 was cut off for calculating the d-hole density.[38] For the values of $h_{3/2,\text{bulk}}$ and $h_{5/2,\text{bulk}}$, 0.118 ($atom^{-1}$) and 0.283 ($atom^{-1}$) were used.[25] The occurrence of holes was explained by the spin-orbit splitting and s-p-d hybridization effects[23,25,26] despite no 5d holes in unperturbed Au (electron configuration $[Xe]6s^14f^{14}5d^{10}$).

2.3.6 Raman scattering and SERs

Raman scattering

Principle

Raman scattering is the inelastic scattering of a photon. It was discovered by Sir Chandrasekhara Venkata Raman and Kariamanickam Srinivasa Krishnan in liquids and by Grigory Landsberg and Leonid Mandelstam in crystals.

In 1922, Indian physicist C. V. Raman published his work on the "Molecular Diffraction of Light", the first of a series of investigations with his collaborators which ultimately led to his discovery (on February 28th, 1928) of the radiation effect which bears his name. Raman received the Nobel Prize in 1930 for his work on the scattering of light. In 1998 the Raman effect was designated an ACS National Historical Chemical Landmark in recognition of its significance as a tool for analyzing the composition of liquids, gases, and solids.

When light is scattered from an atom or molecule, most photons are elastically scattered (Rayleigh scattering), such that the scattered photons have the same energy (frequency) and

wavelength as the incident photons. However, a small fraction of the scattered light (approximately 1 in 10 million photons) is scattered by an excitation, with the scattered photons having a frequency different from, and usually lower than, the frequency of the incident photons.

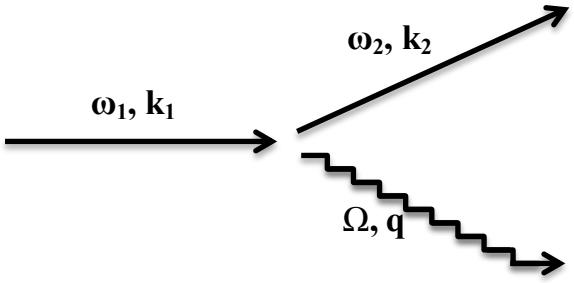

Figure 2.7. An inelastic light scattering process.

Inelastic light scattering[27] describes the phenomenon by which a light beam is scattered by an optical medium and changes its frequency in the process. It contrasts with the elastic light scattering, in which the frequency of the light is unchanged.

Light incident with angular frequency $\boldsymbol{\omega_1}$ and wave vector $\mathbf{k_1}$ is scattered by an excitation of the medium of frequency Ω and wave vector $\mathbf{q}$. The scattered photon has frequency $\boldsymbol{\omega_2}$ and wave vector $\mathbf{k_2}$.

Inelastic light scattering can be subdivided into two generic types:

- Stokes scattering;
- Anti-Stokes scattering;

Stokes scattering corresponds to the emission of a phonon (or some other types of material excitation), while anti-Stokes scattering corresponds to phonon absorption. Conservation of energy during the interaction requires that:

$$\omega_1 = \omega_2 \pm \Omega \tag{2.11}$$

The + sign in equation 2.11 corresponds to phonon emission, while the – sign corresponds to phonon absorption.

In the other ways, when the energy of the incident light is not large enough to excite the molecules from the ground state to the lowest electronic state, the molecule will be excited to a virtual state between the two states. The electron cannot stay long in the virtual state and will immediately go back to the ground state. If the electron goes to where it is originated from, then the wavelength of the scattered light is the same as the light source, which is called Rayleigh scattering. It is possible that the electron goes to the vibrational state different from where it is excited, and then there is an energy difference between the emitted photon and the incident photon. If the emitted energy is smaller than the incident energy, the process is called the Stokes scattering. The opposite is called the anti-Stokes scattering.

In Raman spectroscopy, inelastic light scattering processes are analysed, i.e. scattering processes in which energy is transferred between an incident photon with energy $\hbar\omega_I$ and the sample, resulting in a scattered photon of a different energy $\hbar\omega_s$.[27,28] The amount of transferred energy corresponds to the eigenenergy $\hbar\Omega_j$ of an elementary excitation labeled "j" in the sample, e.g. a phonon, a polariton, a plasmon, a coupled plasmon phonon mode of a single electron or hole excitation.

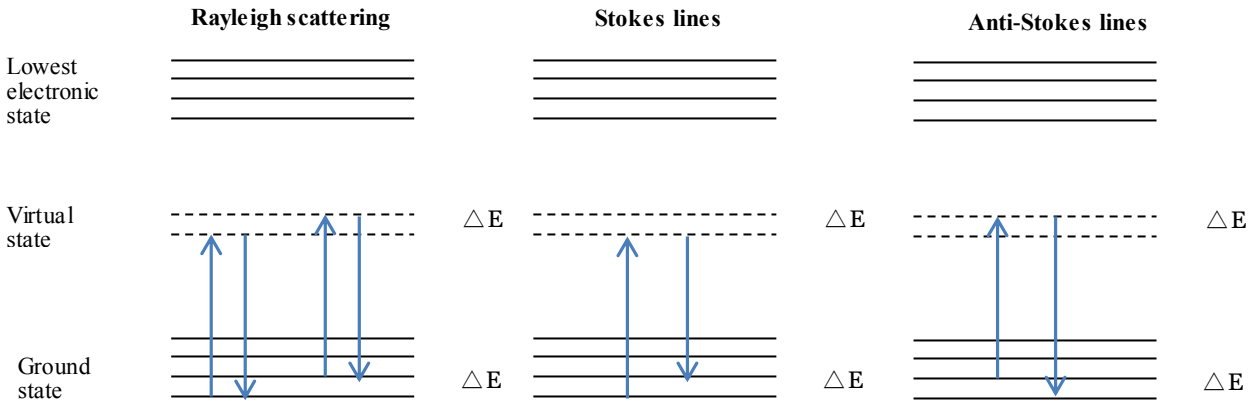

Figure 2.8. The quantum illustration for different cases of scattering

A Raman spectroscopy experiment yields the eigenfrequencies of the elementary excitations through the analysis of the peak frequencies ω_s in the scattered light, since the frequency of the incident light ω_i is well defined by the use of a laser-light source. Energy

conservation yields:

$$\hbar\omega_s = \hbar\omega_1 \pm \hbar\Omega_j \tag{2.12}$$

In analogy to energy conservation, the quasi-momentum conservation law gives the correlation between the wave vector $\mathbf{k_i}$ of the incident light, $\mathbf{k_s}$ of the scattered light and the excitation wave vector $\mathbf{q_j}$:

$$k_s = k_i \pm q_j \tag{2.13}$$

Figure 2.9 shows a basic experimental arrangement that can be used to measure Raman spectra. The sample is excited with a suitable laser, and the scattered light is collected and focused onto the entrance slit of a scanning spectrometer. The number of photons emitted at a particular wavelength is registered using a photon-counting detector and then the results are stored in a computer for analysis. Photomultiplier tubes have traditionally been employed as the detector in this application, but modern arrangements now tend to use array detectors made with charge coupled devices (CCD arrays). By orientating the sample appropriately, the reflected laser light can be arranged to miss the collection optics. However, this still does not

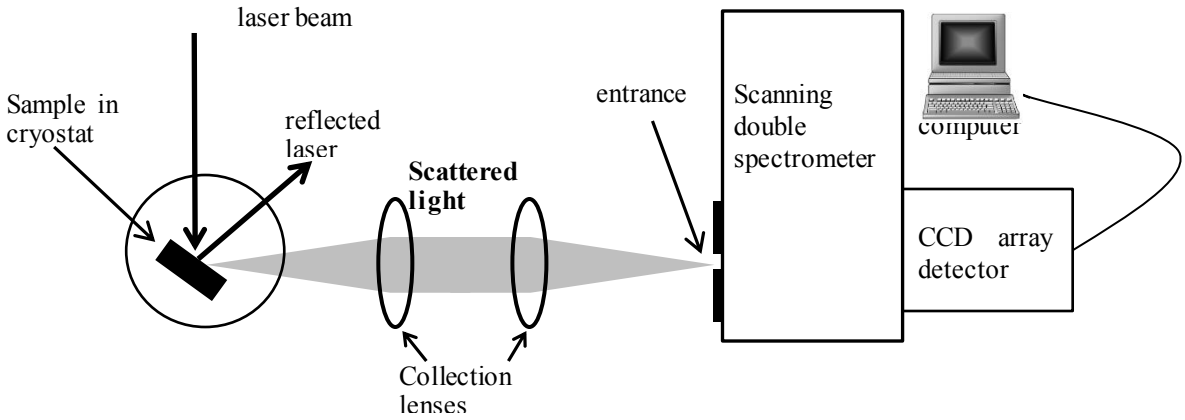

Figure 2.9. Experimental apparatus used to record Raman spectra.

prevent a large number of elastically scattered laser photons entering the spectrometer, and this could potentially saturate the detector. To get around this problem, a high resolution spectrometer with good stray light rejection characteristics is used.

Selection rules are symmetry consideration, based on group theory, which give necessary conditions for a phonon to be observable in Raman spectroscopy.[28]

For materials whose crystal lattice has a center of inversion, group theory predicts that a phonon can be observed exclusively either in Raman spectroscopy or in IR spectroscopy, depending on its symmetry properties. The reason for this exclusion criterion is that in such crystals the irreducible representations of the phonons can be classified in either even modes or odd ones. Even symmetry means invariance of the lattice deformation against inversion while for odd symmetry modes inversion implies a 180^{o} phase shift of the phonon. Due to symmetry arguments, phonons with even symmetry can be Raman active, those with odd symmetry IR-active.

However, the exclusion criterion of Raman and IR activity of phonon does not apply to crystal lattices like III-V compounds. Their structure is like Si, but without a centre of inversion, because of the nonequivalent sublattices: one consisting of group III atoms, the other of group V (T_d-symmetry: zincblende). This allows the observation of the lattice vibrations in Raman as well as in IR spectroscopy. Moreover, the degeneracy of the TO (transverse optical) and LO (longitudinal optical) phonon modes is lifted by the shift of the LO frequency due to its macroscopic electric field.

The intensities for O_h and T_d group are given by[29]

$$I_{\parallel} = A\left[\left(e_x^{(i)}R_{xz}\right)^2 + \left(e_y^{(i)}R_{yx}\right)^2 + \left(e_z^{(i)}R_{yz}\right)^2\right] \qquad (2.14)$$

where A is a constant determined from by the material and the scattered photon frequency, and R is Raman tensor.

Table 2.3. Selection rule for Raman scattering in the T_d group (includes zinc blende crystal) in back scattering and right-angle scattering geometries[29]

Scattering geometry		Selection rule	
		TO phonons	LO phonons
Back scattering	$z(y,y)\bar{z}; z(x,x)\bar{z}$	0	0
	$z(x,y)\bar{z}; z(y,x)\bar{z}$	0	$\|d_{LO}\|^2$
90° scattering	$z(x,z)x$	$\|d_{TO}\|^2$	0
	$z(y,z)x$	$\|d_{TO}\|^2/2$	$\|d_{LO}\|^2/2$
	$z(x,y)x$	$\|d_{TO}\|^2/2$	$\|d_{LO}\|^2/2$

Surface enhanced Raman scattering (SERS)

Surface Enhanced Raman Spectroscopy is a surface-sensitive technique that enhances Raman scattering by molecules adsorbed on rough metal surfaces. The enhancement factor can be as much as 1010 to 1011,7,8 which means the technique may detect single molecules.

SERS from pyridine adsorbed on electrochemically roughened silver was produced by Martin Fleischman and coworkers in 1974;9 they justified the large signal that they saw simply as a matter of the number of molecules that were scattering on the surface and did not recognize that there was a major enhancement effect. In 1977 two groups independently noted that the concentration of scattering species could not account for the enhanced signal and each proposed a mechanism for the observed enhancement. Their theories are still accepted as explaining the SERS effect. Jeanmaire and Van Duyne10 proposed an electromagnetic effect, while Albrecht and Creighton 11 proposed a charge-transfer effect. Rufus Ritchie, of Oak Ridge National Laboratory's Health Sciences Research Division, predicted the existence of the surface plasmon.

Mechanisms

The exact mechanism of the enhancement effect of SERS is still a matter of debate in the literature. There are two primary theories and while their mechanisms differ substantially, distinguishing them experimentally has not been straightforward. The electromagnetic theory posits the excitation of localized surface plasmons, while the chemical theory proposes the formation of charge-transfer complexes. The chemical theory only applies for species which have formed a chemical bond with the surface, so it cannot explain the observed signal enhancement in all cases, while the electromagnetic theory can apply even in those cases where the specimen is only physisorbed to the surface.

Electromagnetic Theory: The increase in intensity of the Raman signal for adsorbates on particular surfaces occurs because of an enhancement in the electric field provided by the surface. When the incident light in the experiment strikes the surface, localized surface plasmons are excited. The field enhancement is greatest when the plasmon frequency, ω_p, is in resonance with the radiation. In order for scattering to occur, the plasmon oscillations must be perpendicular to the surface; if they are in-plane with the surface, no scattering will occur. It is because of this requirement that roughened surfaces or arrangements of nanoparticles are typically employed in SERS experiments as these surfaces provide an area on which these localized collective oscillations can occur.[12]

The light incident on the surface can excite a variety of phenomena in the surface, yet the complexity of this situation can be minimized by surfaces with features much smaller than the wavelength of the light, as only the dipolar contribution will be recognized by the system. The dipolar term contributes to the plasmon oscillations, which leads to the enhancement. The SERS effect is so pronounced because the field enhancement occurs twice. First, the field enhancement magnifies the intensity of incident light which will excite the Raman modes of the molecule being studied, therefore increasing the signal of the Raman scattering. The Raman signal is then further magnified by the surface due to the same mechanism which

excited the incident light, resulting in a greater increase in the total output. At each stage the electric field is enhanced as E2, for a total enhancement of E4.13

The enhancement is not equal for all frequencies. For those frequencies for which the Raman signal is only slightly shifted from the incident light, both the incident laser light and the Raman signal can be near resonance with the plasmon frequency, leading to the E4 enhancement. When the frequency shift is large, the incident light and the Raman signal cannot both be on resonance with ωp, thus the enhancement at both stages cannot be maximal.14

The choice of surface metal is also dictated by the plasmon resonance frequency. Visible and near-infrared radiations (NIR) are used to excite Raman modes. Silver and gold are typical metals for SERS experiments because their plasmon resonance frequencies fall within these wavelength ranges, providing maximal enhancement for visible and NIR light. Copper's absorption spectrum also falls within the range acceptable for SERS experiments. Platinum and palladium nanostructures also display plasmon resonance within visible and NIR frequencies.

Chemical Theory: While the electromagnetic theory of enhancement can be applied regardless of the molecule being studied, it does not fully explain the magnitude of the enhancement observed in many systems. For many molecules, often those with a lone pair of electrons, in which the molecules can bond to the surface, a different enhancement mechanism has been described which does not involve surface plasmons. This chemical mechanism involves charge-transfer between the chemisorbed species and the metal surface. The chemical mechanism only applies in specific cases and probably occurs in concert with the electromagnetic mechanism.

The HOMO to LUMO transition for many molecules requires much more energy than the infrared or visible light typically involved in Raman experiments. When the HOMO and LUMO of the adsorbate fall symmetrically about the Fermi level of the metal surface, light of

half the energy can be employed to make the transition, where the metal acts as a charge-transfer intermediate. Thus a spectroscopic transition that might normally take place in the UV can be excited by visible light.

Selection rules

The term surface enhanced Raman spectroscopy implies that it provides the same information that traditional Raman spectroscopy does, simply with a greatly enhanced signal. While the spectra of most SERS experiments are similar to the non-surface enhanced spectra, there are often differences in the number of modes present. Addition modes not found in the traditional Raman spectrum can be present in the SERS spectrum, while other modes can disappear. The modes observed in any spectroscopic experiment are dictated by the symmetry of the molecules and are usually summarized by selection rules. When molecules are adsorbed to a surface, the symmetry of the system can change, slightly modifying the symmetry of the molecule, which can lead to differences in mode selection.

One common way in which selection rules are modified arises from the fact that many molecules that have a center of symmetry lose that feature when adsorbed to a surface. The loss of a center symmetry eliminates the requirements of the mutual exclusion rule, which dictates that modes can only be either Raman or Infrared active. Thus modes that would normally appear only in the infrared spectrum of the free molecule can appear in the SERS spectrum.

A molecule's symmetry can be changed in different ways depending on the orientation in which the molecule is attached to the surface. In some experiments, it is possible to determine the orientation of adsorption to the surface from the SERS spectrum, as different modes will be present depending on how the symmetry is modified.

Preparation of SERS active substrates

The surface modification of the glass substrates for SERS active experiments was conducted according to the procedure reported by Watts *et al.*[30] Glass slides were cleaned by sonication in acetone for 10 minutes, followed by 10 minutes ultrasonic cleaning in methanol. After drying for 20 minutes at 100°C in air, the slides were immersed in concentrated sulfuric acid for 2 hours. The slides were rinsed thoroughly with distilled water 6 times and then dried for 20 minutes at 100°C in air. Surface modification of the glass substrates was performed by soaking the substrates in a mixture of 3-aminopropyltrimethoxysilane (APTMS, 3 mL) and methanol (60 mL) for 4 hours at room temperature. After soaking, the glass substrates were washed thoroughly using a copious amount of methanol to remove the excess APTMS. The substrates were stored in methanol at room temperature when not in use. The substrates were dried for 20 minutes at 100°C in air as soon as being used.

Measurement conditions

Raman spectra were obtained with an Ar^+ ion laser (wave length 514.5 nm, power 50 mW), using a Horiba-Jobin Yvon Ramanor T64000 triple monochromator equipped with a CCD detector. The nonpolarized Raman scattering measurements were set under a microscope sample holder using a 180° backscattering geometry at room temperature. The laser spot diameter was 1 μm. An acquisition time of 60s per spectrum was used with averaging of three spectra per analysis area.

2.4 References

(1) Frens, G. *Nature-Phys. Sci.* **1973**, *241*, 20.

(2) Pyatenko, A.; Yamaguchi, M.; Suzuki, M. *J. Phys. Chem. B* **2005**, *109*, 21608.

(3) Bigall, N. C.; Härtling, T.; Klose, M.; Simon, P.; Eng, L. M.; Eychmüller, A. *Nano Lett.* **2008**, *8*, 4588.

(4) Dao, A. T. N.; Singh, P.; Shankar, C.; Mott, D.; Maenosono, S. *Appl. Phys. Lett.* **2011**, *99*, 073107.

(5) Mott, D. M. Synthesis, Characterization, and Catalysis of Metal Nanoparticles, State University of New York at Binghamton, 2008.

(6) Luo, J.; Maye, M. M.; Lou, Y.; Han, L.; Hepel, M.; Zhong, C.-J. *Catal. Today* **2002**, *77*, 127.

(7) Maye, M. M.; Kariuki, N. N.; Luo, J.; Han, L.; Njoki, P.; Wang, L.; Lin, Y.; Naslund, H. R.; Zhong, C.-J. *Gold Bull.* **2004**, *37*, 217.

(8) Maye, M. M.; Luo, J.; Han, L.; Kariuki, N. N.; Zhong, C.-J. *Gold Bull.* **2003**, *36*, 75.

(9) Maye, M. M.; Luo, J.; Lin, Y.; Engelhard, M. H.; Hepel, M.; Zhong, C. *Langmuir* **2003**, *19*, 125.

(10) Njoki, P. N.; Jacob, A.; Khan, B.; Luo, J.; Zhong, C.-J. *J. Phys. Chem. B* **2006**, *110*, 22503.

(11) Bozzola, J. J.; Russell, J. D. *Electron Microscopy: Principles and Techniques for Biologists*; Jones and Bartlett Publishers: Boston, 1999.

(12) Dao, A. T. N.; Mott, D. M.; Maenosono, S. In *Handbook of nanoparticles, Synthesis, Functionalization and Surface Treatment*; Springer-Verlag, 2015; p. (In press).

(13) Gilles, R.; Mukherji, D.; Hoelzel, M.; Strunz, P.; Toebbens, D. M.; Barbier, B. *Acta. Mater.* **2006**, *54*, 1307.

(14) Siegbahn, K.; Edvarson, K. *Nucl. Phys.* **1956**, *1*, 137.

(15) Siegbahn, K. M. *Nobel Lect.* **1981**, 63.

(16) Kuhn, M.; Sham, T. K. *Phys. Rev. B* **1994**, *49*, 1647.

(17) Briggs, D.; Grant, J. T. *Surface analysis by Auger and X-ray photoelectron spectroscopy*; Briggs, D.; Grant, J. T., Eds.; IM Publications and SurfaceSpectra: Chichester, 2003.

(18) Nishimura, S.; Dao, A. T. N.; Mott, D.; Ebitani, K.; Maenosono, S. *J. Phys. Chem. C* **2012**, *116*, 4511.

(19) Gailer, J.; George, G. N.; Pickering, I. J.; Buttigieg, G. A.; Denton, M. B.; Glass, R. S. *J. Organomet. Chem.* **2002**, *650*, 108.

(20) Teo, B. K. *EXAFS: Basic principles and data analysis*; Springer-Verlag: Berlin, 1986.

(21) Mansour, A. N.; Cook, J. W.; Sayers, D. E. *J. Phys. Chem.* **1984**, *88*, 2330.

(22) Tyson, C. C.; Bzowski, A.; Kristof, P.; Kuhn, M.; Sammynaiken, R.; Sham, T. K. *Phys. Rev. B* **1992**, *45*, 8924.

(23) Sham, T. K. *Phys. Rev. B* **1985**, *31*, 1888.

(24) Müller, J. E.; Jepsen, O.; Wilkins, J. W. *Solid State Commun.* **1982**, *42*, 365.

(25) Mattheiss, L. F.; Dietz, R. E. *Phys. Rev. B* **1980**, *22*, 1663.

(26) Smith, N. V.; Wertheim, G. K.; Hüfner, S.; Traum, M. M. *Phys. Rev. B* **1974**, *10*, 3197.

(27) Fox, M. *Optical Properties of Solids*; Oxford University Press, 2001.

(28) Bauer, G.; Richter, W. *Optical Characterization of Epitaxial Semiconductor Layers*; Springer, 1995.

(29) Hamaguchi, C. *Basic semiconductor physics*; Springer, 2009.

(30) Seitz, O.; Chehimi, M. M.; Cabet-Deliry, E.; Truong, S.; Felidj, N.; Perruchot, C.; Greaves, S. J.; Watts, J. F. *Colloids Surfaces A Physicochem. Eng. Asp.* **2003**, *218*, 225.

Chapter 3. Synthesis and Characterization of Au@Ag Core@Shell and (Au@Ag)@Au Double Shell Nanoparticles[1–4]

3.1 Introduction

The structural and optical properties of Au@Ag nanoparticles with different Ag shell thicknesses and (Au@Ag)@Au double shell nanoparticles are analyzed using transmission electron microscopy (TEM), scanning TEM-High Angle Annular Dark Field (STEM-HAADF), energy dispersive X-ray spectroscopy (EDS), X-ray photoelectron spectroscopy (XPS), UV-visible spectroscopy (UV-Vis), and Raman spectroscopy. In addition, a preliminary study of the relative chemical stability of Au@Ag and (Au@Ag)@Au nanoparticles in the presence of salt is presented.

3.2 Results and discussions

3.2.1 Monoelemental nanoparticles

Au nanoparticles

Au nanoparticles were synthesized by the citrate reduction method of Frens[5] and were used as seeds for the synthesis of Au@Ag core@shell nanoparticles. The colloidal dispersion of Au seeds is a deep-red color with a localized surface plasmon resonance (LSPR) peak at 518 nm (Figure 3.1b) with a mean diameter, D, of 14.4 ± 0.7 nm (Figure 3.1a).

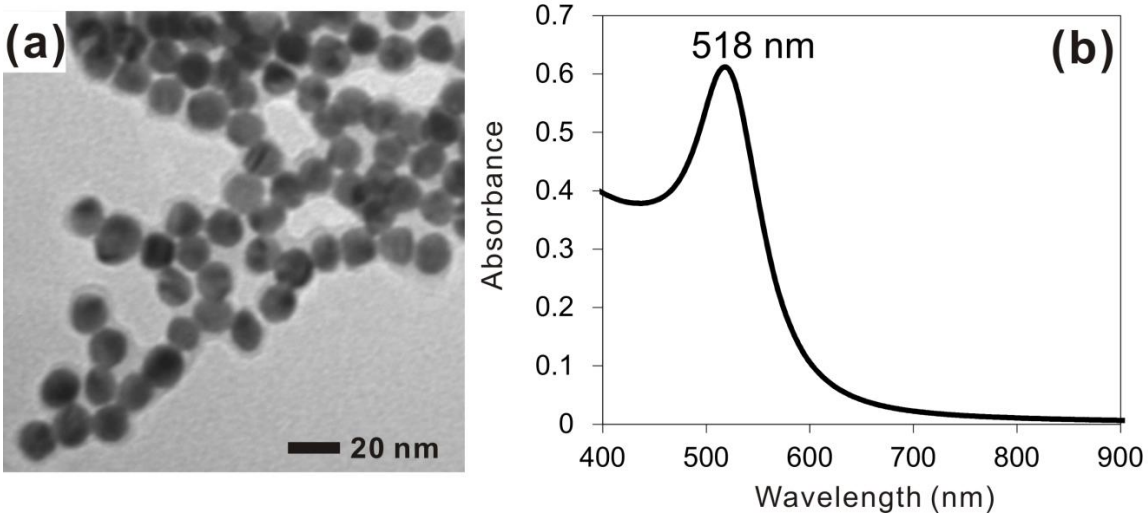

Figure 3.1. (a) TEM image of as-synthesized Au nanoparticles capped with the citrate molecule, (b) UV-Vis spectrum of as-synthesized Au nanoparticles with peak maximum of 518 nm.

Ag nanoparticles

Ag nanoparticles were synthesized by the citrate reduction of $AgNO_3$.[6] The colloidal dispersion of Ag nanoparticles has a light yellow color with a localized surface plasmon resonance (LSPR) peak at 399 nm (Figure 3.2b) with a mean diameter is 34.4±7 nm (Figure 3.2a). Ag nanoparticles synthesized by this method usually have low monodispersity in size as well as shape. In addition, it was very unstable in the presence of salt (see 3.2.5).

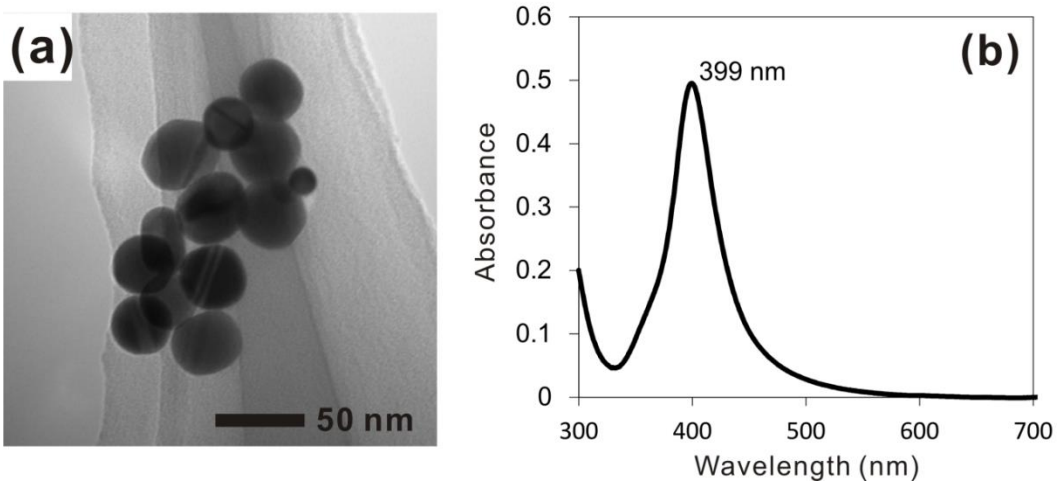

Figure 3.2. (a) TEM image of as-synthesized Ag nanoparticles capped with the citrate molecule, (b) UV-Vis spectrum of as-synthesized Ag nanoparticles with peak maximum of 399 nm.

3.2.2 Au@Ag nanoparticles

To synthesize Au@Ag core@shell nanoparticles, a Ag shell was grown on the Au seeds via seed-mediated growth by adding silver precursor ($AgNO_3$) to the Au seed dispersion with additional sodium citrate at reflux, under an argon atmosphere. As a major advantage of the seed-mediated synthesis, the Ag shell thickness of the resulting Au@Ag core@shell nanoparticles can be finely controlled by varying the amount of $AgNO_3$ added to the reaction solution. The thickness of the Ag shell for these Au@Ag nanoparticles increased by varying the concentration of 5 mL $AgNO_3$ added from 1.128, 3.008, 7.324 to 12.86 mM. In total, four different Ag shell thicknesses were obtained, including 0.4 ± 0.3, 1.0 ± 0.6, 2.2 ± 0.4 and 3.6 ± 0.4 nm (Figure 3.3), which correspond very closely to the theoretical shell thickness (0.45, 1.09, 2.29, and 3.48 nm, respectively) calculated from the metallic feeding ratio. The Ag shell thickness is expressed in the subscript hereafter, e.g. $Au@Ag_x$; x denotes the Ag shell thickness. It is noteworthy to point out that the resultant Au@Ag nanoparticles are highly monodisperse in terms of size and shape in comparison to Ag nanoparticles synthesized by comparable reduction methods.

The UV-Vis spectra of all Au@Ag core@shell nanoparticles are shown in figure 3.4. When x was increased, the LSPR band gradually became blue-shifted, with the LSPR peak of Ag eventually becoming dominant. Finally, the $Au@Ag_{3.6}$ nanoparticles show a single LSPR peak at 390 nm, which stems from the plasmon resonance of the Ag shells. The appearance of a monomodal LSPR band corresponding to Ag indicates that the Au cores are uniformly covered by the Ag shell and the optical contribution from the Au cores is completely screened. However, Ag nanoparticles of a similar size typically show a LSPR peak at 416 nm.[7] The significant blue-shift of the LSPR peak appearing in the Ag shell of the Au@Ag core@shell nanoparticles suggests a higher electron density in the Ag shells than that of pure Ag nanoparticles due to an electron transfer from the Au core to the Ag shell.[8]

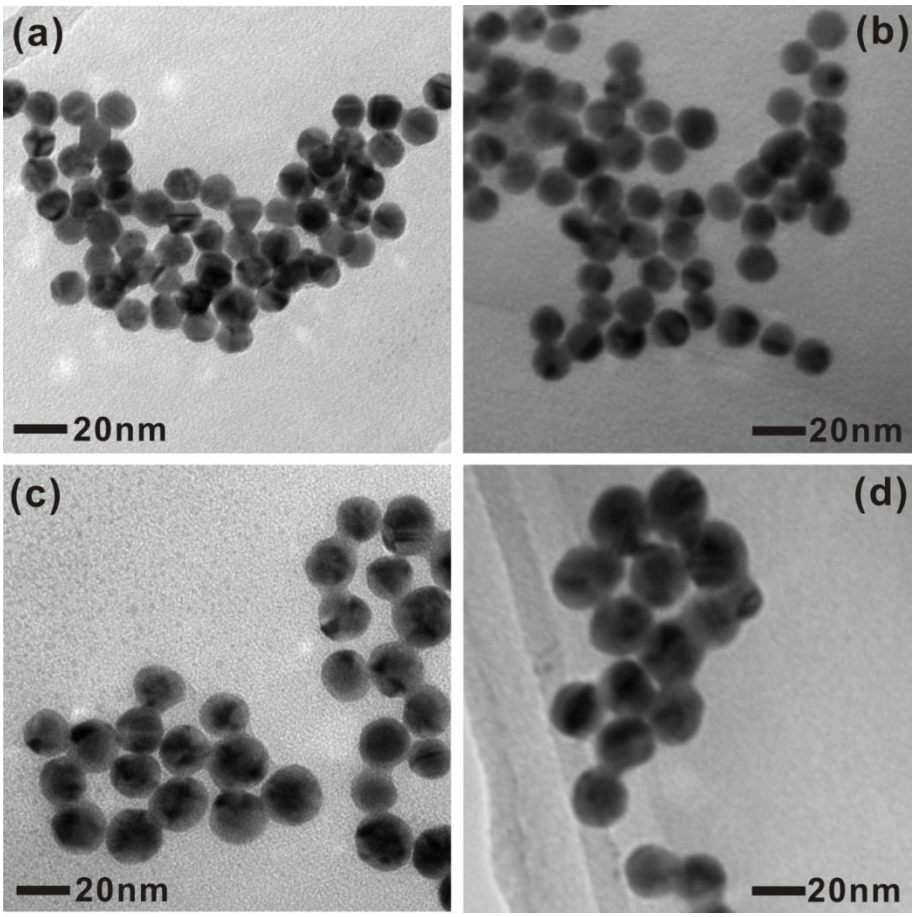

Figure 3.3. TEM images of as-synthesized Au@Ag core@shell nanoparticles with different shell thicknesses: 0.4 (a), 1 (b), 2.2 (c), 3.6 (d) nm.

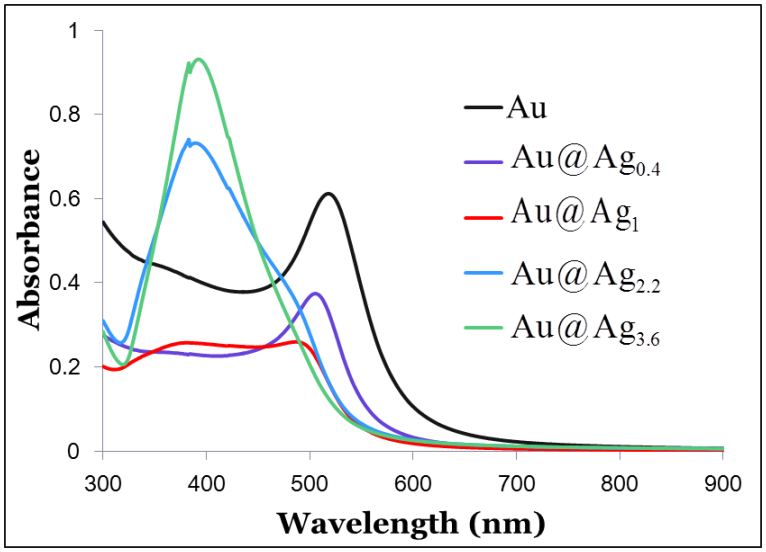

Figure 3.4. UV-Vis spectra of as-synthesized Au@Ag nanoparticles with different shell thicknesses. The values in the figure are the thicknesses of the Ag shell: 0.4, 1, 2.2, and 3.6 nm.

3.2.3 (Au@Ag)@Au double shell nanoparticles

As mentioned in 1.4, the fact that Ag@Au core@shell nanoparticles have defects or gaps in the Au shell or the hollow sections in the interface of Au and Ag mainly caused by the galvanic replacement reaction. The galvanic replacement reaction is driven by the difference in the electrochemical potential between the two metals, with one serving as the cathode and the other as the anode. Regarding the general preparation of Ag@Au nanoparticles, the reduction potential of $AuCl_4^-$/Au (0.99 V vs SHE) is more positive than that of AgCl/Ag (0.22 V vs SHE).[9] Hence, Ag nanoparticles serve as sacrificial templates being oxidized by $HAuCl_4$ according to equation 1.6. This reaction is initiated locally at a high-energy site (e.g., surface step, point defect, or hole in the capping layer)[10] rather than over the entire surface. In the case that Au@Ag nanoparticles are used as cores, however, the Ag shells are expected to have a higher electron density than Ag nanoparticles due to electron transfer from the Au core to the Ag shell. The electron rich Ag shell results in a negative oxidation state, $Ag^{\delta-}$, and thus, may lead to effectively suppress the galvanic replacement reaction. Xia and coworkers also claimed a similar result in which a higher potential was required to oxidize Ag atoms contained in a Ag-Au alloy.[9] It was also reported that when the molar ratio of Au to Ag is more than 0.17, the galvanic reaction was hindered, indicating that a higher Au content can protect Au-Ag alloy nanoparticles against galvanic etching.[11] Very possibly, the addition of Au changes the Ag reduction potential and alters the oxidative relationship between Ag^0 and $AuCl_4^-$.

To confirm this assumption, we deposited an Au second shell onto the $Au@Ag_{3.6}$ core@shell nanoparticles by adding $HAuCl_4$ with additional sodium citrate, at reflux, to form $(Au@Ag_{3.6})@Au$ double shell nanoparticles. With respect to core@shell nanoparticles, Liz Marzán and coworkers have synthesized Au@Ag, Au@Ag@Au and finally Au@Ag@Au@Ag multishell nanoparticles using a similar synthetic approach to the present scheme.[12] In their approach however, the deposited intermediate Ag shell thickness was much greater than our

own (ca. 32 nm), which resulted in the formation of hollow structures with partial alloying when the Au shell was deposited. In our own study, the intermediate Ag shell thickness is limited to the range where the charge transfer phenomenon takes place, allowing the ability to create Au@Ag@Au nanoparticles without significant alloying or defects in the structure.

The UV-Vis spectrum of (Au@$Ag_{3.6}$)@Au double shell nanoparticles was shown in the figure 3.5. After being coated by the second Au shell (theoretical thickness 0.15 nm), the LSPR peak of Au@$Ag_{3.6}$ double shell nanoparticles (392 nm) is slightly red-shifted by about 10 nm indicating the formation of a thin Au shell onto the Ag surface. In figure 3.6b, a TEM image of (Au@$Ag_{3.6}$)@Au double shell nanoparticles is shown. The (Au@$Ag_{3.6}$)@Au double shell nanoparticles are more uniform in size and shape (Figure 3.6a) when compared to typical Ag@Au nanoparticles.[13] Moreover, they have no observable gaps or defects in the particle structure. Interestingly, the deposition of the second Au shell onto the Ag surface again causes the reduction of Ag^0 $3d_{5/2}$ BE (Figure 3.8c) indicating an electron transfer between the Au second shell and the Ag first shell.

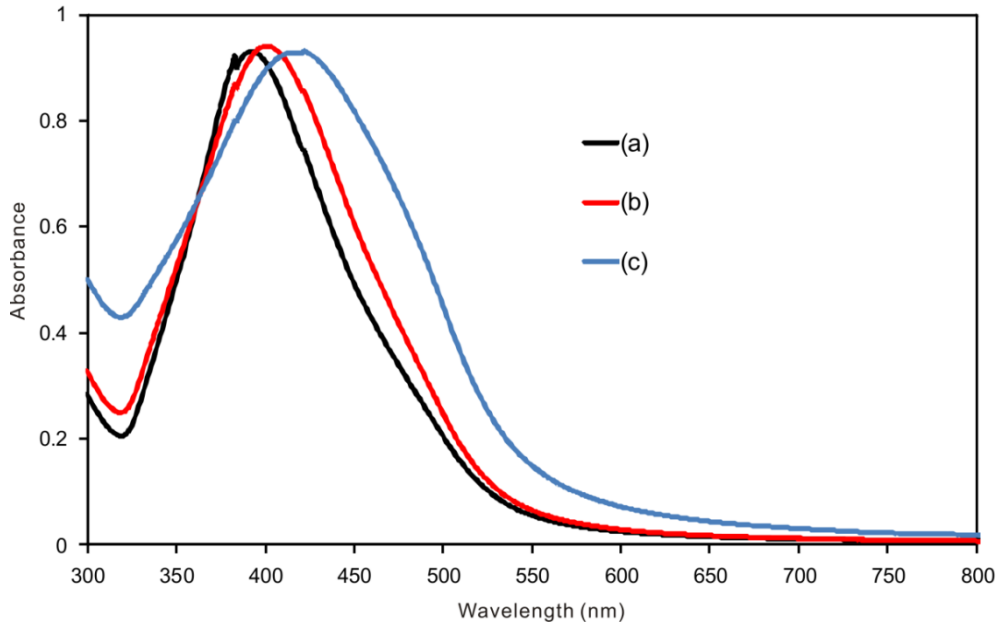

Figure 3.5. UV-Vis spectra of (a) Au@$Ag_{3.6}$, (Au@$Ag_{3.6}$)@Au double shell nanoparticles with different Au shell thicknesses: 0.13 (b) and 1.2 (c) nm.

To further confirm the formation of the Au second shell, STEM-HAADF imaging and EDS elemetal mapping were carried out for the (Au@$Ag_{3.6}$)@Au double shell nanoparticles using a JEOL JEM-ARM200F instrument operated at 200 kV with a spherical aberration corrector (nominal resolution 0.8 Å). Figure 3.6c shows the STEM-HAADF image (high Z contrast) of the (Au@$Ag_{3.6}$)@Au double shell nanoparticles. Since the heavier Au atoms (atomic number, Z = 79) give rise to a brighter image than the lighter Ag atoms (Z = 47) in the dark field image, the Au core appears brighter than the Ag first shell.

One can see a very bright eggshell-thin layer on the Ag first shell (Figure 3.6c). The thickness of the thin layer is 0.13 nm, which agrees well with the theoretical value (0.15 nm) calculated based on the amount of Au precursor added. This indicates that a thin continuous Au second shell was successfully formed on the Au@$Ag_{3.6}$ nanoparticles. The EDS mapping result (Figure 3.6d-f) also clearly indicates that the resulting nanoparticles have a (Au@$Ag_{3.6}$)@Au double shell structure. When Ag nanoparticles were used directly as cores to

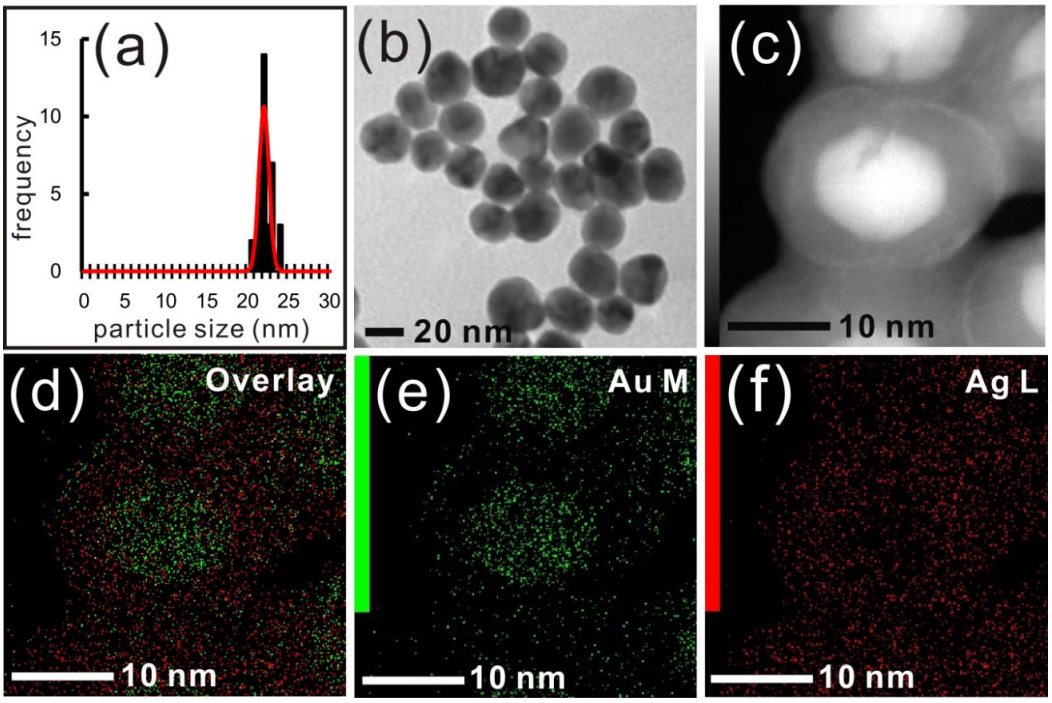

Figure 3.6. Size distribution (a), TEM image (b) and (c) STEM-HAADF image of (Au@$Ag_{3.6}$)@Au double shell nanoparticles (with 0.13 nm of second Au shell). (D-F) EDS elemental mapping images of (Au@$Ag_{3.6}$)@Au nanoparticles: Overlay (D) of Au M edge (E) and Ag L edge (F).

form Ag@Au core@shell nanoparticles, the resulting nanoparticles display defects such as pinholes in the Au shell and/or voids in the interior which are caused by the galvanic replacement reaction.[14] In light of the current results, it is intriguing that a uniform continuous Au shell could be formed on the Ag intermediate shell without special handling. However, the outermost Au shell is only 1-2 Au atomic layers thick, and thus, it might be difficult to prevent the inter-diffusion of Au and Ag atoms and hence the formation of Au-Ag alloy in this particular case. For this reason, we deposited a thicker Au second shell with 1.2 nm theoretical thickness to further probe the characteristics of the second shell. Figure 3.7 shows the STEM-HAADF and the EDS mapping images of the double shell nanoparticles. The mean diameter of the resulting nanoparticles is 23.0±1.9 nm, which agrees well with the theoretical value (23.2 nm) calculated based on the amount of Au precursor added. This means that the Ag first shell was not etched away during the deposition of the Au second shell.

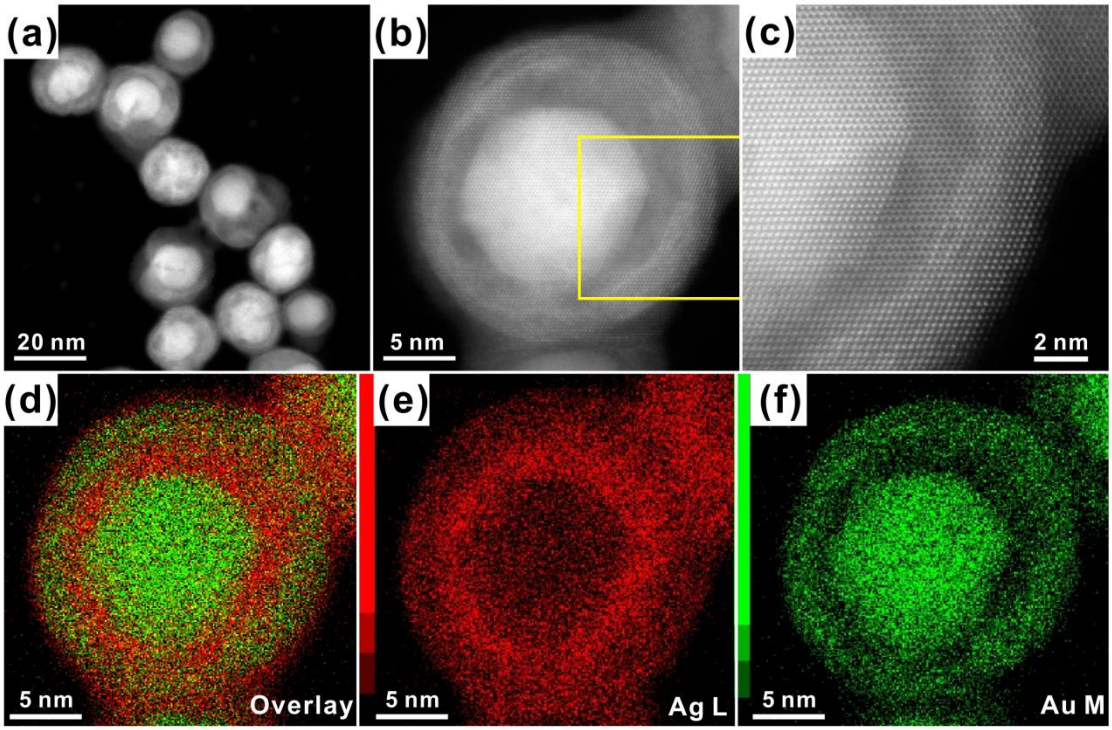

Figure 3.7. (a-c) STEM-HAADF images and (d-f) EDS elemental mapping images of (Au@Ag)@Au double shell nanoparticles with a thick Au second shell (1.2 nm): Overlay (d) of Ag L edge (e) and Au M edge (f).

As can be clearly seen in figure 3.7, the resulting nanoparticles surely have a double shell structure with defect-free Au second shells, although Au and Ag atoms seem to mutually diffuse to a certain degree. Importantly, an interface between the Ag first shell and the Au second shell is totally coherent indicating that the galvanic replacement reaction is significantly suppressed.

3.2.4 Electronic structure of Au-Ag nanoparticles

XPS analysis

In order to confirm the occurrence of the charge transfer effect, we carried out XPS measurements for Au@Ag_x in comparison with pure Ag and Au nanoparticles. Figure 3.8a show high resolution XPS core-level spectra of Ag, Au@Ag_x core@shell nanoparticles. The Ag 3d core levels are split into $3d_{3/2}$ and $3d_{5/2}$ spin-orbit pairs (Figure 3.8a). Taking a closer look at the asymmetrically broadened $3d_{5/2}$ component, the overlapping peaks were deconvoluted by using G-L mixed function.[2] In the case of pure Ag nanoparticles, the $3d_{5/2}$ and $3d_{3/2}$ components could be deconvoluted into Ag^0 (peak at 368.26 eV) and Ag oxide (peak at 367.8 eV) as shown in figure 3.8b-c. On the other hand, in the cases of Au@Ag_x nanoparticles, the $3d_{5/2}$ component could be fitted to Ag^0 (peak at 368.18 ± 0.03 eV (Figure 3.8b-c). Importantly, no Ag oxide peak exists in the Au@Ag_x nanoparticles even though the Ag first shell is exposed to the outside.

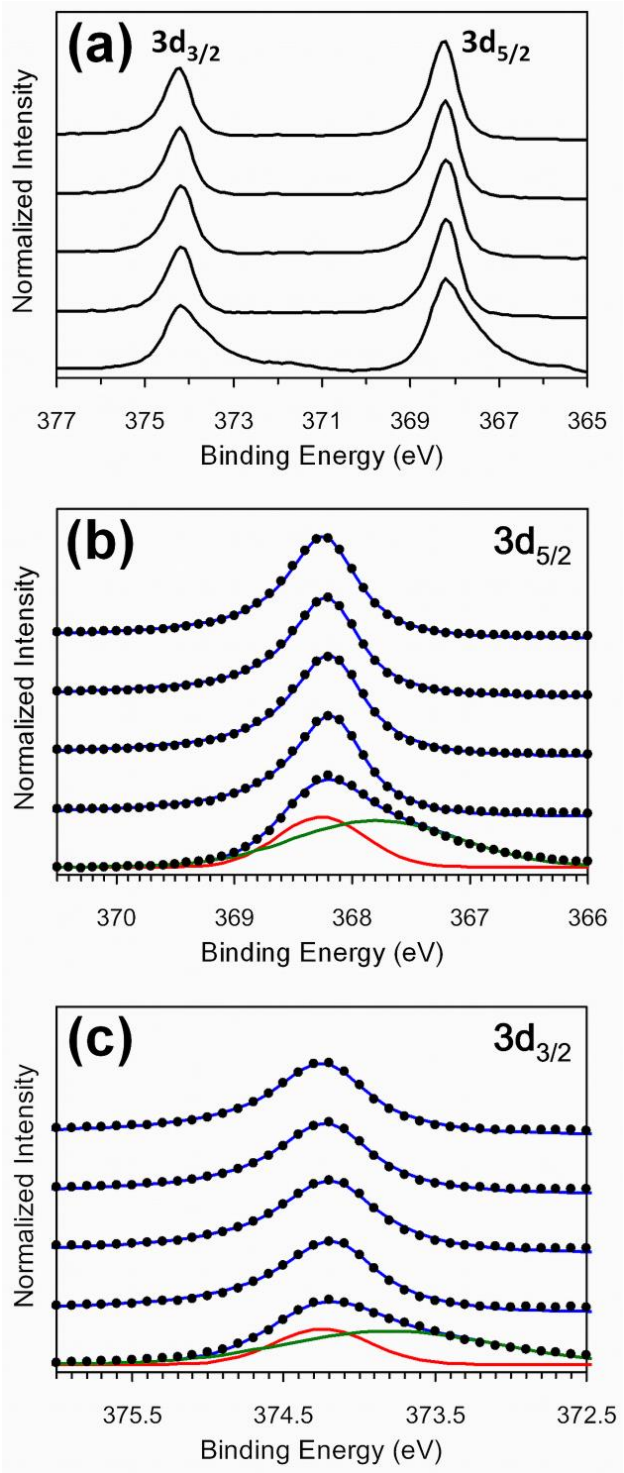

Figure 3.8. (a) XPS spectra of Ag and Au@Ag_x (x = 0.4, 1.0, 2.2 and 3.6, respectively from the bottom to top. Magnified XPS spectra focusing on (b) the Ag $3d_{5/2}$ peak (black circles) and (c) the Ag $3d_{3/2}$ peak (black circles). In the case of Ag nanoparticles, the peak was deconvoluted by using two Gaussian functions corresponding to Ag^0 (red curves) and Ag oxide (green curves) components. Solid blue curves represent the sum of two Gaussian curves. In the case of Au@Ag_x nanoparticles, the peaks were fitted to the asymmetric G-L mixed function (solid blue curves).[2]

The Ag^0 $3d_{5/2}$ peak energy is plotted as a function of x as shown in Figure 3.9. All $Au@Ag_x$ nanoparticles exhibit a negative shift in the Ag^0 $3d_{5/2}$ BE compared to that of pure Ag nanoparticles (368.26 eV). Moreover, the Ag^0 $3d_{5/2}$ BE increases toward the value of pure Ag nanoparticles with increasing x suggesting that the charge transfer takes place only in the vicinity of the interface between the Au core and the Ag shell. It is worth noting that all $Au@Ag_x$ nanoparticles exhibit a positive shift in the Au 4f BE (ca. 0.1 eV) compared to that of pure Au nanoparticles as shown in figure 3.10.

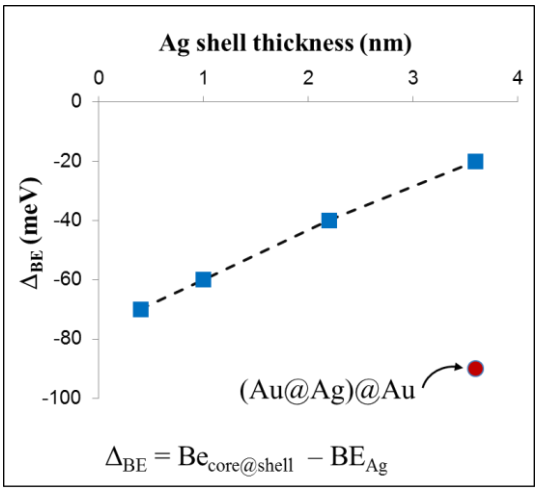

Figure 3.9. The Ag^0 $3d_{5/2}$ peak energy plotted as a function of the Ag shell thickness, x.

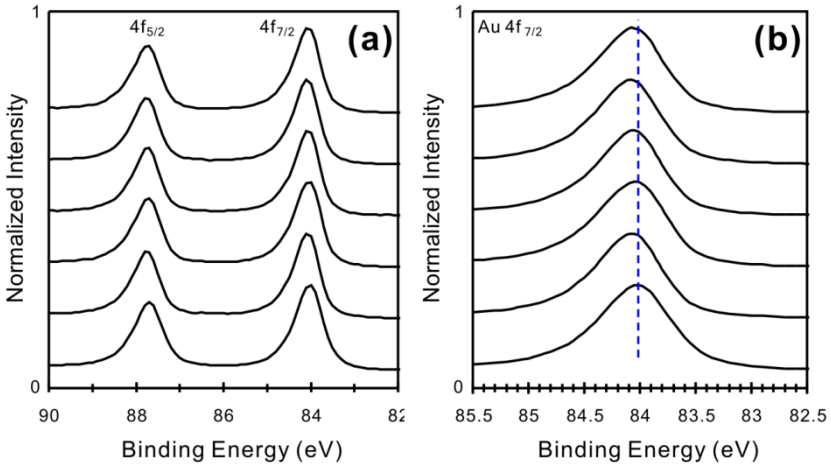

Figure 3.10. (a) XPS spectra of Au, $Au@Ag_x$ (x = 0.4, 1.0, 2.2 and 3.6), and $(Au@Ag_{3.6})@Au$ double shell nanoparticles, respectively from the bottom to top. (b) Magnified XPS spectra focusing on the Au $4f_{7/2}$ peak.

XANES analysis[4]

Figure 3.11 shows the XANES spectra in the Au L_2- and L_3-edges for Au foil, Au nanoparticles, Au@Ag core@shell nanoparticles and (Au@Ag)@Au double-shell nanoparticles. All spectra shows the same resonance patterns as that of Au metal. In particular, the Au foil and Au nanoparticles shows almost identical XANES spectra in both L_2- and L_3-edges. A gradual increase of the threshold resonance at the shoulder peak occurs in the order Au nanoparticles < Au@Ag < (Au@Ag)Au in L_2- and L_3-edges. The increase in the WL area in the L_2- and L_3-edges XANES spectra can be attributed to the decrease in 5d occupancy.[15]

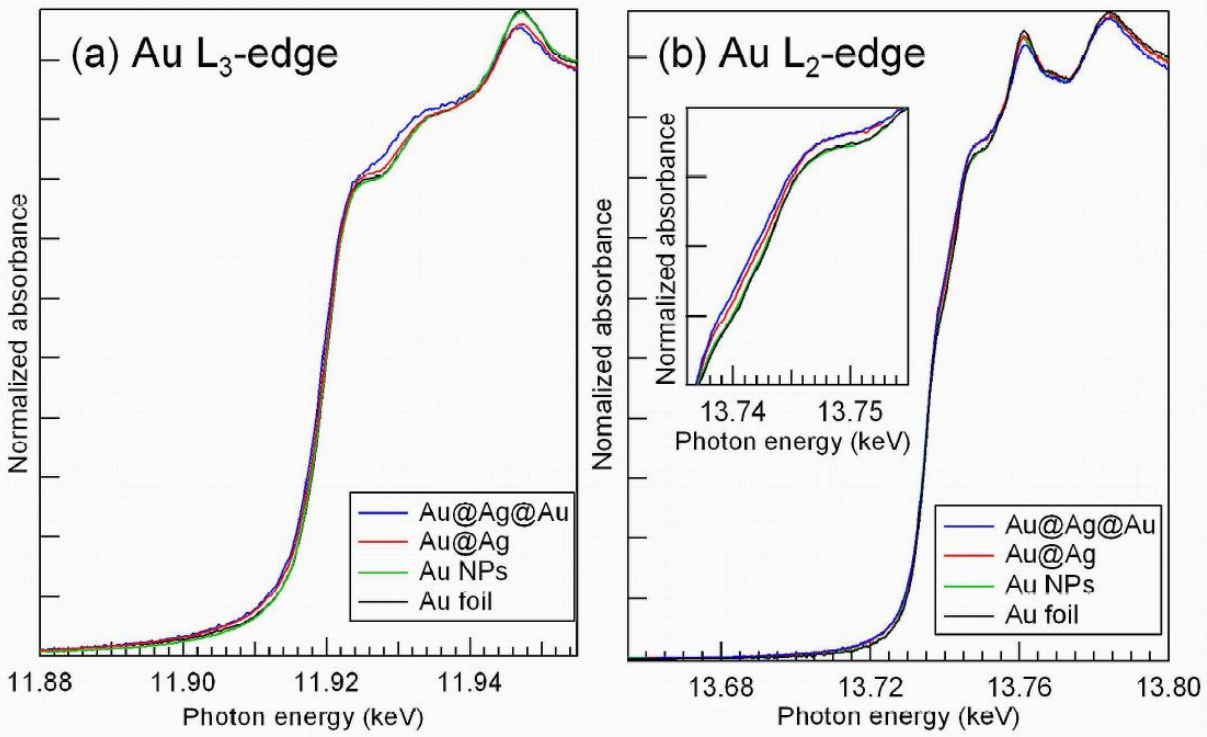

Figure 3.11. (a) Au L_3-edge and (b) Au L_2-edge XANES spectra of the samples. From bottom to top, Au foil, Au nanoparticles, Au@Ag core@shell nanoparticles and (Au@Ag)@Au double-shell nanoparticles.[4]

To further investigate the unoccupied d states, all relevant parameters were derived and listed in table 3.1.[4] Although small differences were detected in the hole densities between Au nanoparticles and Au foil, it is reasonable to assume that there is relatively no electronic

difference between them because our Au nanoparticles have a relatively large diameter (14.4 nm) which is too large to exhibit size-dependent effects.[16,17] There are several reports which showed an increase in the hole density of Au atoms in Au nanoparticles due to the chemisorption of hydrogen[18] or capping ligands[19,20] on the surface, or simply due to the small size.[21] However, these observations are only applied for the cases of small Au clusters less than 4 nm in diameter. In addition, it has been reported that the dodecanethiol-protected Au nanoparticles above approximately 12 nm in diameter have almost the same value of d vacancies as that of bulk Au.[22]

Table 3.1. Derived parameters for the unoccupied d states.[4,23]

Samples	$\mathbf{\Delta A_2}$ (eV.cm^{-1})	$\mathbf{\Delta A_3}$ (eV.cm^{-1})	$\boldsymbol{\Delta h_{3/2}}$	$\boldsymbol{h_{3/2}}$	$\boldsymbol{\Delta h_{5/2}}$	$\boldsymbol{h_{5/2}}$	$\boldsymbol{\Delta h_{3/2} + \Delta h_{5/2}}$
Au foil	0	0	0	0.118	0	0.283	0
Au NPs	157.1	-148.5	6.3×10^{-3}	0.124	-5.5×10^{-3}	0.278	7.8×10^{-4}
Au@Ag NPs	383.0	617.2	1.5×10^{-2}	0.133	1.6×10^{-2}	0.299	3.1×10^{-2}
(Au@Ag)@Au NPs	516.0	1340.6	2.1×10^{-2}	0.139	3.7×10^{-2}	0.320	5.7×10^{-2}

The values of both $\Delta h_{3/2}$ and $\Delta h_{5/2}$ increased in the Au@Ag core@shell nanoparticles when compared to the Au nanoparticles. From Au@Ag core@shell nanoparticles to the (Au@Ag)@Au double-shell nanoparticles, a further increase in both $\Delta h_{3/2}$ and $\Delta h_{5/2}$ was observed. This trend strongly supports that the electron transfer from Au to Ag takes place in the nanoparticles. Figure 3.12a and b show the differences of the d-orbital vacancies ($\Delta h_{3/2}$ + $\Delta h_{5/2}$) and the shifts of Au $4f_{7/2}$ XPS peak energy when compared to those of bulk Au, respectively. In the cases of Au@Ag and (Au@Ag)@Au nanoparticles, an increase in the total d-orbital vacancies and a positive energy shift in the $4f_{7/2}$ peak were clearly observed. Importantly, both of them increase with increasing Au-Ag interfacial area. On the other hand, it has been previously observed that a negative shift in the Ag 3d peak energy occurs for both

Au@Ag and (Au@Ag)@Au nanoparticles when compared to bare Ag nanoparticles.[1] The collective results of XANES for Au and XPS for Au and Ag clearly illustrated that a unique charge transfer from Au to Ag occurs through the formation of a Au@Ag core@shell structure, and which is enhanced by Au outer-shell formation. It is expected that the electronic and chemical properties of the Ag shell can be turned by coupling the Ag shell to the Au core due to a charge transfer that increases electron density within the Ag shell yielding a negative Ag oxidation state which suppress the oxidation of the Ag shell.[1]

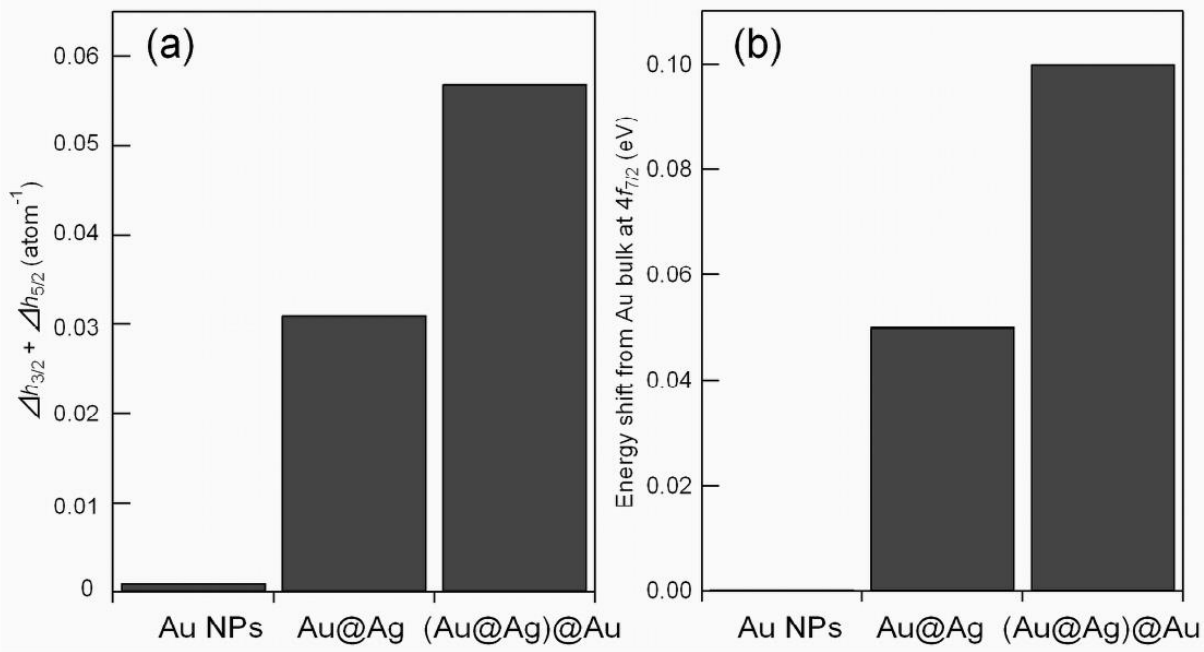

Figure 3.12. (a) Differences of the d-orbital vacancies from bulk Au and (b) XPS energy shift in the $4f_{7/2}$ peak from bulk Au.[4]

Bzowski and coworkers investigated the relationship between Au 5d-hole distribution and Pauling's electronegativity (χ) of the host element in the AuM_2 alloy series (M = Al, Ga, In, Sn, Sb and Te). They found that the number of d holes in Au atoms increases as χ of the M decreases.[24] This phenomenon has been elucidated by a charge-compensation mechanism: the Au gains electron density into the 5d and 6sp orbitals donated from the 5d orbital of M in accordance with χ, thereafter, the lopsided charge balance between Au and M after the donation was corrected for the contribution of back donation from the d orbital of Au to M.

Upon the charge redistribution, the charge onto M is overcompensated. The magnitude of overcompensation is proportional to the difference in χ between Au and M. The electronic behaviors in Au alloys have also been explained based on the same mechanism by other researchers.[25–27] The values of χ for Au and Ag are 2.54 and 1.93, respectively, and thus, the charge-compensation mechanism could be a reason for the charge transfer from Au to Ag at the interface between the Au core (or Au second shell) and Ag shell.

3.2.5 Chemical stability of nanoparticles

If the Ag first shell has a negative oxidation state and the oxidation resistivity is enhanced, the chemical stability of Au@Ag_x nanoparticles to electrolytes is expected to also be improved. Therefore, the chemical stability of Au@$Ag_{3.6}$ nanoparticles is compared to that of pure Ag nanoparticles in the presence of NaCl (8.2 mM). As a result, it was found that the Au@$Ag_{3.6}$ nanoparticles preserved their morphology 3 hours after the addition of NaCl into the aqueous NP dispersion even while some local defects occurred (Figure 3.13b), while the Ag nanoparticles were totally destroyed under identical conditions (Figure 3.13a). However, the mean size of Au@$Ag_{3.6}$ nanoparticles decreased down to 16.4±1.6 nm. This means that nearly 80% of the Ag shell was etched away. In the case of (Au@$Ag_{3.6}$)@Au double shell nanoparticles, their morphology was completely preserved (Figure 3.13c), likely because the (Au@$Ag_{3.6}$)@Au nanoparticles have a more negative Ag oxidation state than Au@Ag_x nanoparticles and/or the Au second shell effectively protects the Ag first shell from contact with Cl^- ions suggesting that the chemical stability of the (Au@$Ag_{3.6}$)@Au nanoparticles is extremely high even under severe conditions. The mean size of (Au@$Ag_{3.6}$)@Au nanoparticles did not change before and after NaCl addition. These results are strong evidence that the Ag first shell is in a negative oxidation state, $Ag^{\delta-}$, due to the electron transfer from the Au core to the Ag shell preventing it from oxidation.

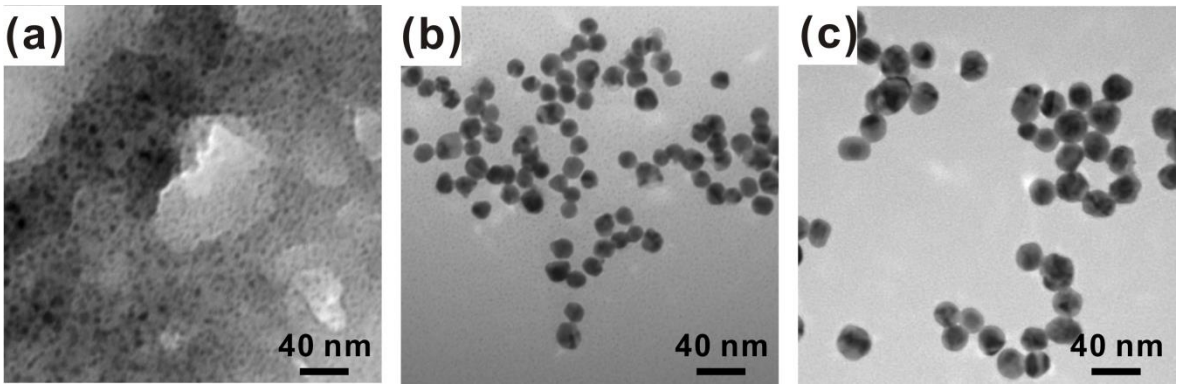

Figure 3.13. TEM images of (a) Ag, (b) $Au@Ag_{3.6}$, and (c) $(Au@Ag_{3.6})@Au$ nanoparticles (with 0.13 nm of the second Au shell thickness) 3 hours after adding NaCl.

3.2.6 SERS activity of nanoparticles

The required biofunctionalization of colloidal particles is a complex process due to the delicate balance between attractive Van der Waals and repulsive electrostatic forces between nanoparticles in aqueous solution. Changes in the ionic strength, pH or temperature can lead to colloidal aggregation. To avoid these difficulties, LSPR biosensing can be performed with nanostructures on solid surfaces. NP assembly on solid substrates is generally carried out by chemical binding, exploiting the high affinity of gold and silver colloids toward amino or mercapto functional groups, typically present on glass surfaces upon silanization.[28–31]

Therefore, as-synthesized nanoparticles were taken for creating assemblies using 3-amino-1,2,4-triazole-5-thiol (ATT). Then the assemblies were deposited onto the APTMS-modification glass substrate. Finally, the surface enhanced Raman scattering (SERS) activity of core@shell nanoparticles was investigated using ATT as a dual linker and reporter molecule using the same protocol reported previously.[32] The SERS activity was found to dramatically increase with increasing x in the case of the $Au@Ag_x$ nanoparticles as shown in figure 3.14 taking advantage of high extinction coefficients and extremely high field enhancements of Ag. Moreover, the $(Au@Ag_{3.6})@Au$ nanoparticles exhibited a SERS activity as high as $Au@Ag_{3.6}$ nanoparticles. Note that an Ar^+ ion laser (wavelength 514.5 nm) was used to obtain the Raman spectra. This result is consistent with previous results; namely, the

SERS activities of Ag and Ag@Au nanoparticles are almost equivalent when ATT molecules are used for assembling nanoparticles to form hot spots.[32]

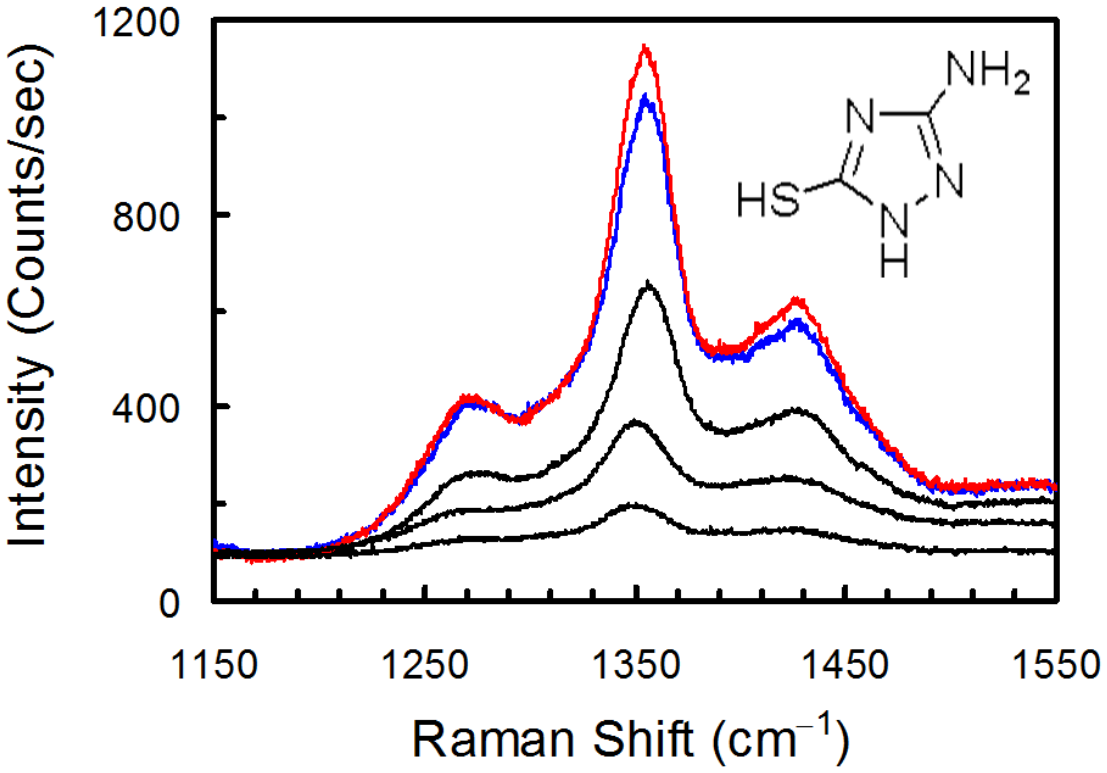

Figure 3.14. Raman spectra of Au@Ag$_x$ [from bottom to top, x = 0.4, 1, 2.2, and 3.6 nm (blue curve)] and (Au@Ag$_{3.6}$)@Au (red curve) NP assemblies created by using ATT.

3.3 Conclusion

In summary, we have found that an electron transfer from the Au core to the Ag shell takes place in Au@Ag core@shell nanoparticles resulting in an enhancement of the oxidation resistivity of the Ag shell. The enhanced oxidation resistivity of the Ag shell effectively suppresses the galvanic replacement reaction during the Au second shell deposition process, and thus, the resultant (Au@Ag)@Au double shell nanoparticles have a uniform size, shape and structure without defects which cannot be avoided in the case of Ag@Au NP syntheses. Using the charge-transfer-induced electronic modification technique, one can synthesize well-defined core@shell nanoparticles which have not been achieved until now. The

(Au@Ag)@Au double shell nanoparticles are highly stable in presence of salt with high Raman activity. These particles are ultimately expected to lead to a novel class of highly active and stable nanoprobes for bio-molecular sensing and diagnostics.

3.4 References

(1) Dao, A. T. N.; Singh, P.; Shankar, C.; Mott, D.; Maenosono, S. *Appl. Phys. Lett.* **2011**, *99*, 073107.

(2) Maenosono, S.; Lee, J.; Dao, A. T. N.; Mott, D. *Surf. Interface Anal.* **2012**, *44*, 1611.

(3) Mott, D. M.; Anh, D. T. N.; Singh, P.; Shankar, C.; Maenosono, S. *Adv. Colloid Interface Sci.* **2012**, *185-186*, 14.

(4) Nishimura, S.; Dao, A. T. N.; Mott, D.; Ebitani, K.; Maenosono, S. *J. Phys. Chem. C* **2012**, *116*, 4511.

(5) Frens, G. *Nature-Phys. Sci.* **1973**, *241*, 20.

(6) Pyatenko, A.; Yamaguchi, M.; Suzuki, M. *J. Phys. Chem. B* **2005**, *109*, 21608.

(7) Mott, D.; Thuy, N. T. B.; Aoki, Y.; Maenosono, S. *Phil. Trans. R. Soc. A* **2010**, *368*, 4275.

(8) Mulvaney, P.; Linnert, T.; Henglein, A. *J. Phys. Chem.* **1991**, *95*, 7843.

(9) Skrabalak, S. E.; Chen, J.; Sun, Y.; Lu, X.; Au, L.; Cobley, C. M.; Xia, Y. *Acc. Chem. Res.* **2008**, *41*, 1587.

(10) Wang, Z. L. *J. Phys. Chem. B* **2000**, *104*, 1153.

(11) Gong, X.; Yang, Y.; Huang, S. *J. Phys. Chem. C* **2010**, *114*, 18073.

(12) Rodríguez-González, B.; Burrows, A.; Watanabe, M.; Kiely, C. J.; Marzán, L. M. L. *J. Mater. Chem.* **2005**, *15*, 1755.

(13) Qian, L.; Yang, X. *Colloids Surfaces A Physicochem. Eng. Asp.* **2005**, *260*, 79.

(14) Ferrer, D. A.; Diaz-Torres, L. A.; Wu, S.; Jose-Yacaman, M. *Catal. Today* **2009**, *147*, 211.

(15) Qi, B.; Perez, I.; Ansari, P. H.; Lu, F.; Croft, M. *Phys. Rev. B* **1987**, *36*, 2972.

(16) Tsunoyama, H.; Sakurai, H.; Negishi, Y.; Tsukuda, T. *J. Am. Chem. Soc.* **2005**, *127*, 9374.

(17) Comotti, M.; Della Pina, C.; Matarrese, R.; Rossi, M. *Angew. Chem. Int. Ed.* **2004**, *43*,

5812.

(18) Soldatov, A. V.; Longa, S. Della; Bianconi, A. *Solid State Commun.* **1993**, *85*, 863.

(19) Zhang, P.; Sham, T. K. *Appl. Phys. Lett.* **2002**, *81*, 736.

(20) Häkkinen, H.; Barnett, R. N.; Landman, U. *Phys. Rev. B* **1999**, *82*, 3264.

(21) Zhang, P.; Sham, T. *Phys. Rev. Lett.* **2003**, *90*, 245502.

(22) Ohyama, J.; Teramura, K.; Shishido, T.; Hitomi, Y.; Kato, K.; Tanida, H.; Uruga, T.; Tanaka, T. *Chem. Phys. Lett.* **2011**, *507*, 105.

(23) Mattheiss, L. F.; Dietz, R. E. *Phys. Rev. B* **1980**, *22*, 1663.

(24) Bzowski, A.; Yiu, Y. M.; Sham, T. K. *Phys. Rev. B* **1995**, *51*, 9515.

(25) Kuhn, M.; Sham, T. K. *Phys. Rev. B* **1994**, *49*, 1647.

(26) Sham, T. K.; Yiu, Y. M.; Kuhn, M. *Phys. Rev. B* **1990**, *41*, 11881.

(27) Sham, T. K.; Perlman, M. L.; Watson, R. E. *Phys. Rev. B* **1979**, *19*, 539.

(28) Nath, N.; Chilkoti, A. *Anal. Chem.* **2002**, *74*, 504.

(29) Xue, C.; Li, Z.; Mirkin, C. A. *Small* **2005**, *1*, 513.

(30) Fujiwara, K.; Watarai, H.; Itoh, H.; Nakahama, E.; Ogawa, N. *Ana. Bioanal. Chem.* **2006**, *386*, 639.

(31) Kreuzer, M. P.; Quidant, R.; Badenes, G.; Marco, M.-P. *Biosens. Bioelectron.* **2006**, *21*, 1345.

(32) Singh, P.; Thuy, N. T. B.; Aoki, Y.; Mott, D.; Maenosono, S. *J. Appl. Phys.* **2011**, *109*, 094301.

Chapter 4. Synthesis and Characterization of Pt@Ag Core@Shell Nanoparticles[1]

4.1 Introduction

Plasmonic-based sensing probes consisting of nanoparticles (NP)s have become highly desirable because of their enhanced sensitivity, low cost, and easy to use nature.[2,3] Gold and silver are the most common type of metal studied for NP-based sensors because of their strong surface plasmon resonance (SPR) properties.[4] Silver is especially intriguing because it has the highest optical cross section for any metal, but still suffers from oxidation and an inability of its plasmonic properties to be tuned for a desired application.[5] As a result, nanoparticles with complex structures (heterostructures) such as core@shell nanoparticles have the potential to display the strong optical properties of silver, be robust and possess controllable plasmonic properties [5]. Several silver-based heterostructured NP systems have been created in an attempt to realize robust and active NP sensing probes, however silver nanoparticles remain sensitive to oxidation, or display compromised plasmonic properties.[5–7] For example, Ag@Au or AuAg alloy nanoparticles have proven limited in exhibiting the same level of plasmonic activity as pure silver nanoparticles, and oftentimes the structure of these particles is challenging to control precisely.[6–8] Instead, a new approach to the creation of silver based heterostructured nanoparticles is required to more fully understand the relationship between NP structure and the resulting optical/plasmonic properties. Recently, it was shown that by understanding the electronic characteristics of silver at the nanoscale, insight can be gained into how to create heterostructured silver based sensing probes with desired and controllable properties.[9,10] Specifically, it was shown that Au@Ag nanoparticles display a unique electron transfer phenomenon that results in the silver shell becoming oxidation resistant while retaining its strong plasmonic properties.[9,11] By extending this phenomenon to other silver based NP systems, insight can be gained into how to manipulate

the particle structure and composition towards the desired characteristics. With this goal in mind, we created a series of different sized platinum particles and coated them in silver shells of various thicknesses. In this case, platinum was chosen as a core material because of its status as a noble metal, its fcc crystal structure (the same as for silver), and its chemical similarity to gold. The resulting particles were characterized in terms of their structural/composition properties, and then the electronic properties of these probes were analyzed by using X-Ray Photoelectron Spectroscopy. The results demonstrate that the electronic transfer phenomenon can be extended to a wide range of heterostructure systems, and provides insight into how to exploit electronic transfer to create silver based sensing probes with enhanced robustness, high optical/plasmonic activity and plasmonic characteristics that can be tuned for a desired application.

4.2 Results and Discussion

The results and discussion section is split into four main parts. First we study the general NP characteristics such as size, shape, composition and structural parameters. This section is followed by analysis of the particle crystalline properties of the Pt@Ag nanoparticles. Next we address the electronic properties in an in-depth XPS study, probing the effect of increasing thickness of silver on the platinum particle surface and the impact on the NP electronic structure. Finally, we comment on the implications of the electronic transfer effect on creating sensitive and robust NP based sensing probes. Throughout the results and discussion section, the notation $Pt_x@Ag_y$ will be used where x and y represent the mean platinum core size or silver shell thickness, respectively. As will be discussed, a wide range of particles with various core size and shell thickness were created, leading to a large amount of redundant data. As a result, we often present a representative sample analysis in the interest of creating a cohesive study.

4.2.1 General Morphology and Optical Properties

Initially, platinum core nanoparticles were synthesized. These particles serve as the basis

for creating Pt@Ag nanoparticles in further studies, and their size, structure and morphology play a key role in the characteristics of the final Pt@Ag nanoparticles. Figure 4.1 shows a set of representative TEM images collected for platinum particles synthesized with increasing size. First, following the above synthetic protocol, relatively small platinum seed particles were created. These seed nanoparticles have a size of 4.5 ± 0.7 nm and are roughly spherical in shape (though they do appear to be slightly clustered). The seed nanoparticles were used in subsequent reaction steps to produce incrementally larger platinum nanoparticles with average sizes of 25.7 ± 4.3, 31.3 ± 5.1, 39.8 ± 4.6 and 99.3 ± 3.7 nm. In general, the platinum NP size and morphology became visually more uniform, but display highly roughened surfaces. The high degree of surface roughness may suggest that the nanoparticles are polycrystalline in nature. The NP sizes were determined using TEM analysis, however in light of the fact that the smaller platinum nanoparticles are slightly clustered, and the larger particles are polycrystalline in nature with highly roughened surfaces, the particle size distributions have a limited amount of statistical significance because of the uncertainty associated in judging the particle sizes graphically. Note that while different ratios of precursor were used (to obtain different particle sizes) the average sizes of platinum particle created in this work are consistent with those created previously.[12]

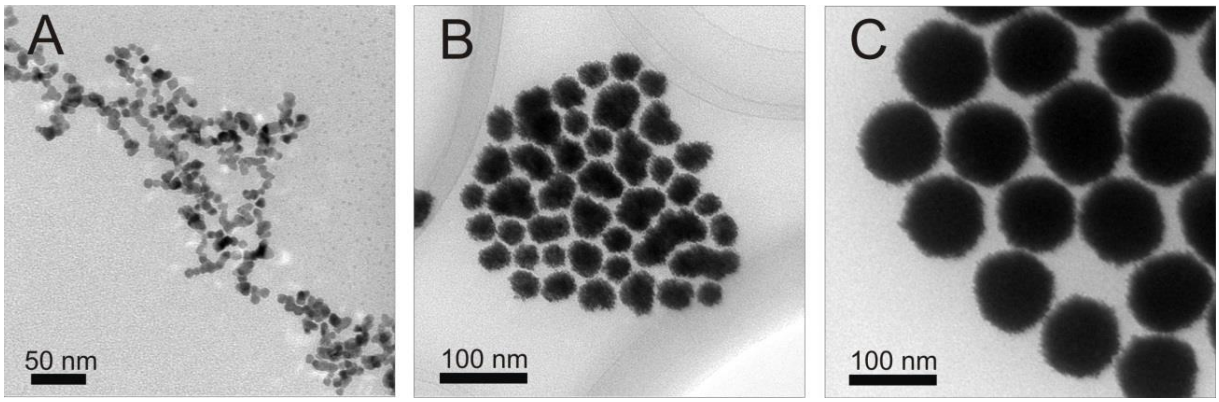

Figure 4.1. TEM images of platinum nanoparticles with a size of 4.5 (**A**); 31.3 (**B**); and 99.3 (**C**) nm.

Next, the platinum nanoparticles were used as cores for the deposition of silver on the

particle surface. Figure 4.2 shows the TEM images collected for a single bare platinum core with a size of 39.8 nm, as well as particles with incrementally increasing silver shell thicknesses of 1.3, 5.2 and 9.1 nm. Immediately after the initial coating with silver, the particle surface becomes much smoother in appearance. This trend continues for increasing silver shell thicknesses.

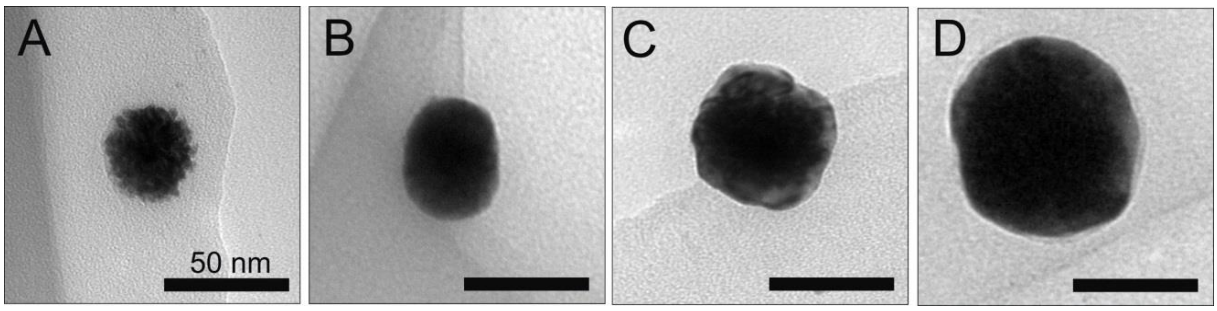

Figure 4.2. TEM images of a platinum core particle (39.8 nm) (**A**) and Pt@Ag particles with an optimal silver shell thickness of 1.3 (**B**); 5.2 (**C**); and 9.1 (**D**) nm.

After coating the platinum particles in a silver shell, the original platinum cores cannot be directly observed in traditional TEM analysis. In order to elucidate the core@shell structural nature of the nanoparticles, we performed STEM-HAADF analysis coupled with EDS elemental mapping technique. The combination of these two analysis techniques gives an excellent 2-dimensional structural picture of the created materials. Figure 4.3 shows the STEM-HAADF image of a single $Pt_{25.7}@Ag_{8.1}$ NP as well as EDS elemental maps taken of the same particle for silver L line, platinum M line and an overlay of the two maps. First, the STEM-HAADF image clearly shows that the platinum particle exists in the center of the newly formed $Pt_{25.7}@Ag_{8.1}$ NP. This is indicated by the very bright core region observed in the image surrounded by a less bright peripheral area. The STEM-HAADF technique offers enhanced contrast sensitivity to the elements atomic number, essentially larger atomic number elements appear relatively more bright in the image, known as Z contrast.[13] The mapping images for platinum and silver show the relative location of these two elements, with the overlay map clearly demonstrating that platinum is confined to the core region of

the particle while silver surrounds the platinum core. The data provides good evidence of the core@shell structural nature of these Pt@Ag nanoparticles.

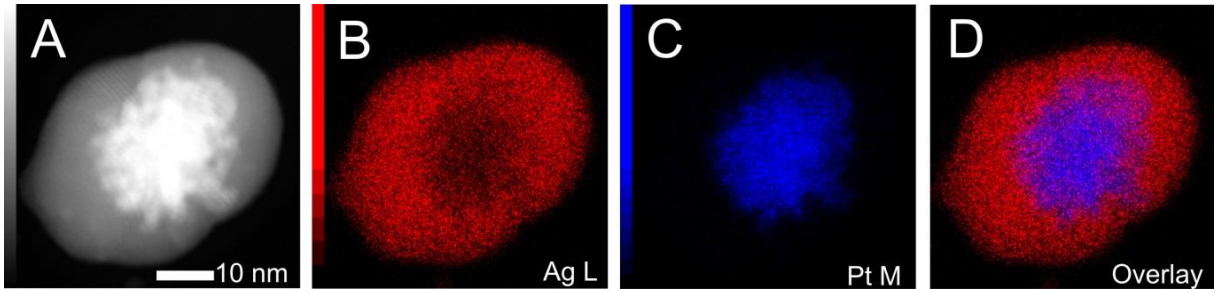

Figure 4.3. STEM-HAADF image (**A**) and the corresponding EDS elemental maps for silver L line (**B**); platinum M line (**C**); and an overlay of the two maps (**D**) for a single $Pt_{25.7}@Ag_{8.1}$ NP.

The bare platinum and Pt@Ag nanoparticles display plasmonic properties which were studied using UV-Vis spectroscopy. Figure 4.4 shows the UV-Vis spectra taken for four different types of NP including bare platinum, $Pt_{39.8}@Ag_{1.3}$, $Pt_{39.8}@Ag_{5.2}$ and $Pt_{39.8}@Ag_{9.1}$ nanoparticles.

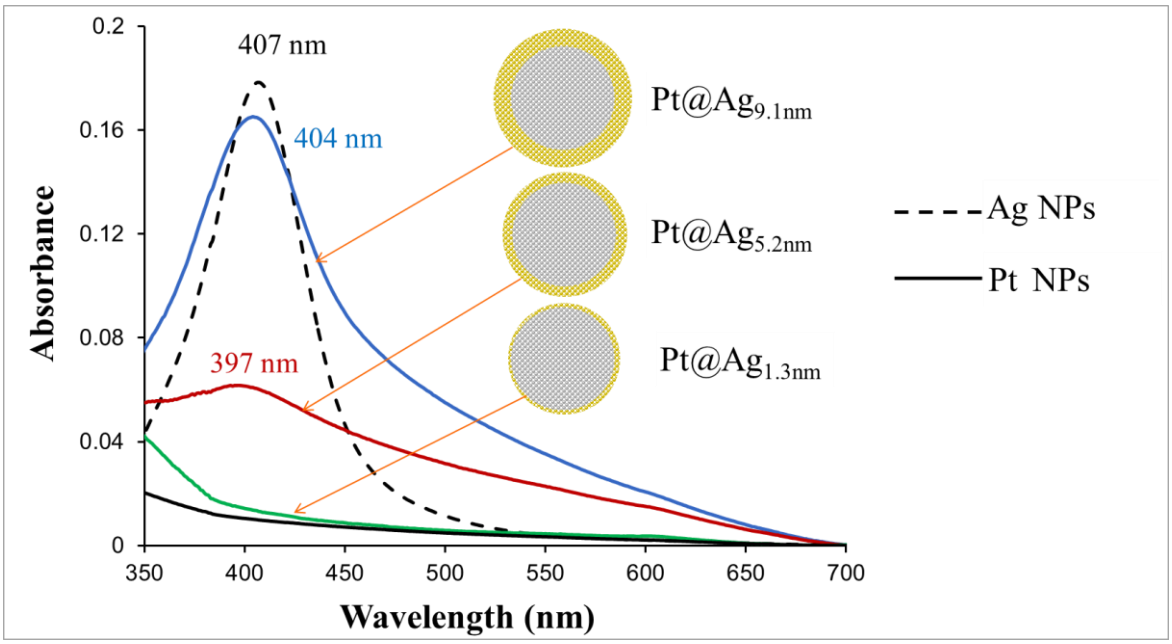

Figure 4.4. UV-Vis spectra for platinum core particle (39.8 nm) and $Pt_{39.8}@Ag_y$ particles with an optimal silver shell thickness of 1.4; 5.2; and 9.1 nm.

It can be observed that the bare platinum and $Pt_{39.8}@Ag_{1.3}$ samples do not display surface plasmon resonance (SPR) in the visible region, but the $Pt_{39.8}@Ag_{5.2}$ and $Pt_{39.8}@Ag_{9.1}$ exhibit a clear SPR band around 400 nm, growing in intensity as the silver shell thickness increases. The position of this SPR band is typical for silver nanoparticles.[5,9,10]

4.2.2 Unique Crystalline Structure

The larger sized platinum nanoparticles as well as the Pt@Ag structures possess a unique crystal structure as evidenced by XRD analysis. Figure 4.5 shows the XRD patterns of three NP samples including platinum nanoparticles with a size of both 4.5 and 25.7 nm, as well as for $Pt_{25.7}@Ag_{8.1}$ nanoparticles.

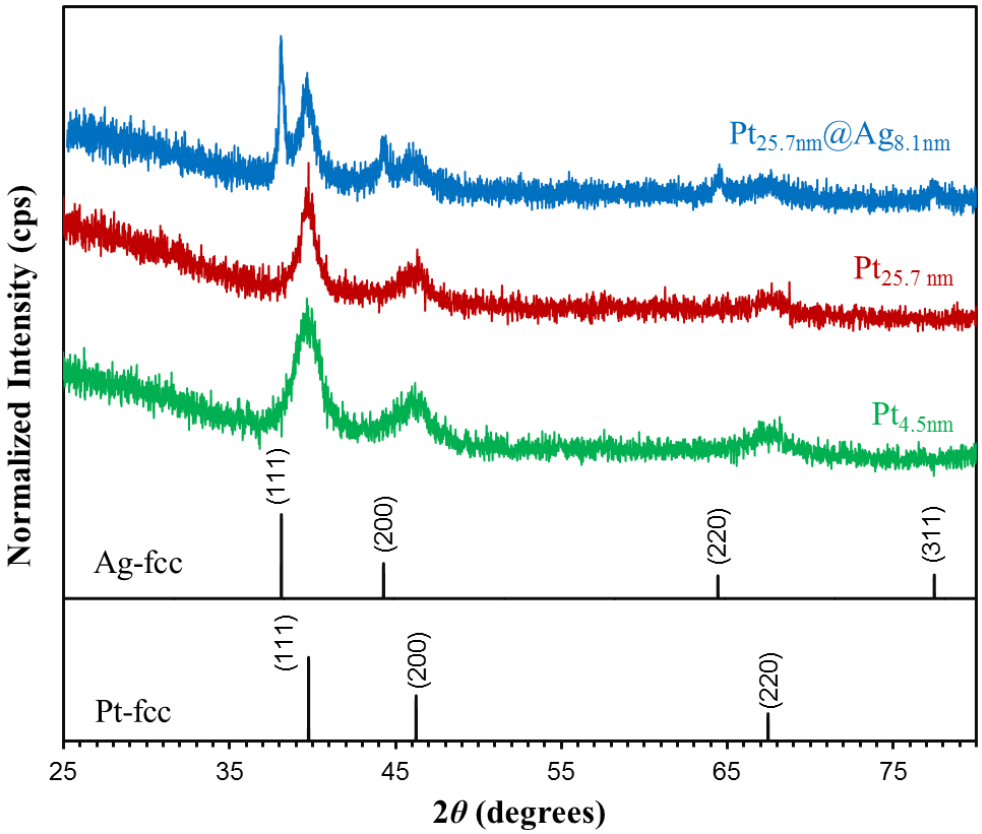

Figure 4.5. XRD pattern of platinum seeds (4.5 nm), platinum nanoparticles (25.7 nm) and $Pt_{25.7}@Ag_{8.1}$ nanoparticles. The reference peak positions for fcc phase platinum and silver are also shown.

The graph also includes the location of reference peaks for fcc silver and platinum.[14,15] For

both sizes of platinum NP, the pattern shows broad peaks at locations consistent for fcc phase platinum. After coating with silver, peaks originating from the platinum metal are still observed with new sharper peaks appearing at the location for fcc phase silver. Scherrer analysis of the primary 111 peaks for both platinum and silver was used to study the crystalline size properties of the particles and revealed a mean crystalline size of 5.1 nm for smaller platinum nanoparticles, 7.3 nm for larger platinum nanoparticles, and 20.2 nm for the silver shells deposited onto the larger sized platinum cores. In this case, the silver has a larger mean crystalline size than the relative shell thickness because the shell is continuous and encapsulates the entire core platinum particle, reflecting the monocrystalline nature of the silver shell. The results reveal a unique crystalline structure for this particle system where larger sized platinum nanoparticles are polycrystalline in nature, while the deposited silver shell is monocrystalline in nature as evidenced by the large mean silver crystal size measured using Scherrer analysis. The resulting morphological structure is a cluster of smaller platinum crystals encapsulated in a continuous silver casing, which could influence the resulting electronic properties to a large degree. Equation 4.1 shows the Scherrer equation used where d (nm) is the mean size of the crystalline domain (crystalline size) of the nanoparticles, K is the shape factor (dimensionless) with a value of 0.9 (but depends on the shape of nanoparticles), λ [nm] is the X-ray wavelength (λ = 0.15418 nm), β (rad) is the peak width at half the maximum intensity (FWHM) and θ [rad] is the peak position (Bragg angle).[16] Table 4.1 lists the determined parameters for the 111 peaks for both platinum and silver metals, as well as the derived mean crystalline size.

$$d = \frac{K\lambda}{\beta cos\theta} \tag{4.1}$$

Table 4.1. Peak parameters and mean crystalline size derived from Scherrer analysis of the 111 peaks in XRD patters.

		2θ (degrees)	β (degrees)	d (nm)
$Pt_{4.5nm}$		39.76	1.73	5.1
$Pt_{25.7nm}$		39.64	1.20	7.3
$Pt_{25.7nm}@Ag_{8.1nm}$	Pt	39.48	1.21	7.3
	Ag	37.94	0.43	20.2

HRTEM analysis provides additional confirmation of the crystalline structure of the Pt@Ag nanoparticles. Figure 4.6 shows HRTEM images of a single platinum NP (25.7 nm) as well as for a single $Pt_{25.7}@Ag_{8.1}$ NP. The bare platinum NP shows a clustered morphology with atomic lattice planes facing several different directions, suggesting a polycrystalline nature. Measurement of the atomic plane spacing gives an average value of 0.220 nm, consistent with the 111 plane of fcc platinum.[14] For the silver coated sample, the outermost area appears more continuous in terms of the crystal lattice. The measurement of the atomic plane spacing at the periphery of the particle gives a value of 0.249 nm, consistent with the 111 plane of fcc silver.[15]

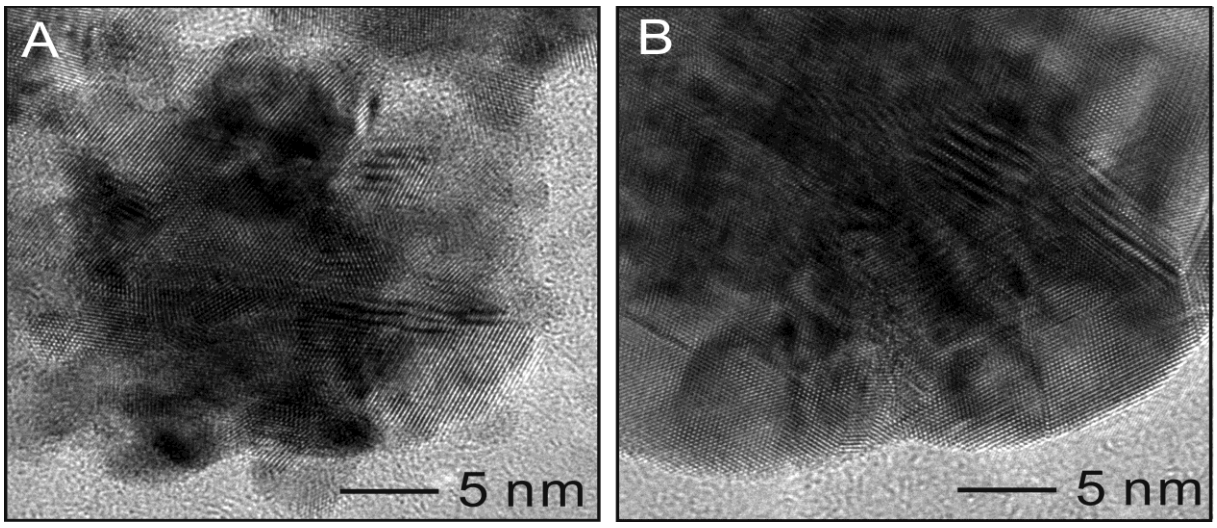

Figure 4.6. HRTEM images of a bare platinum (25.7 nm) NP (**A**) and for a $Pt_{25.7}@Ag_{8.1}$ NP (**B**).

4.2.3 Electronic Structure

In order to gain a diagnostic assessment of the electronic properties of the silver shell in Pt@Ag nanoparticles, XPS analysis was performed on a series of Pt@Ag nanoparticles with increasing shell thickness. A total of five samples were analyzed including pure silver (35.0 nm) nanoparticles, $Pt_{39.8}@Ag_{1.3}$, $Pt_{39.8}@Ag_{5.2}$, $Pt_{39.8}@Ag_{9.1}$ and pure platinum nanoparticles (39.8 nm). Figure 4.7 shows the collected XPS spectra in the Ag 3d area while figure 4.8 shows the XPS spectra collected in the Pt 4f region.

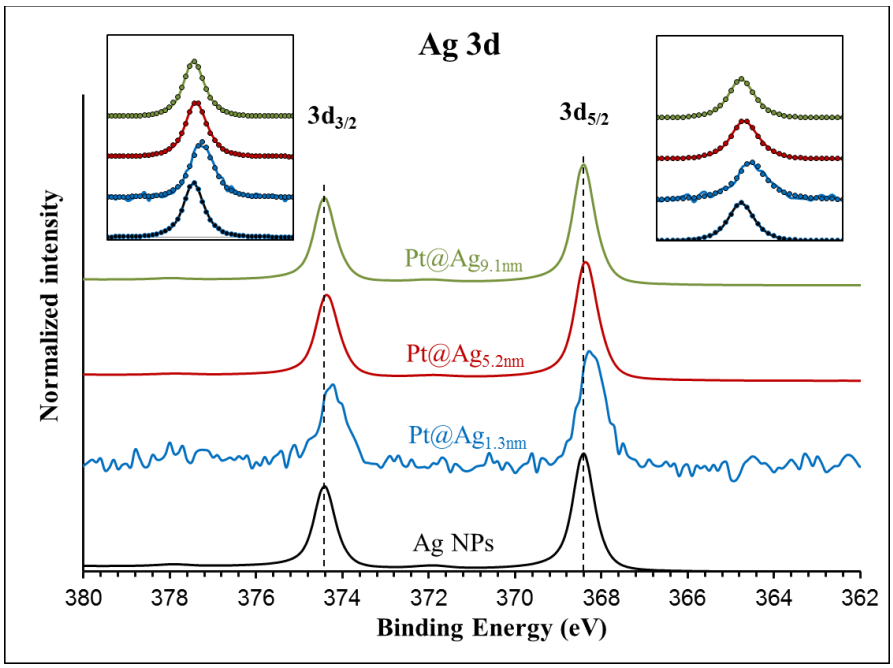

Figure 4.7. XPS spectra in the Ag 3d area for monometallic silver nanoparticles with a size of 35.0 nm, (**A**) and $Pt_{39.8}@Ag_y$ particles with an optimal silver shell thickness of 1.3 (**B**); 5.2 (**C**); and 9.1 (**D**) nm. The inserted graphs show the Ag $3d_{5/2}$ and $3d_{3/2}$ peaks (solid curves) and the fitting with the asymmetric G-L mixed function (circles).

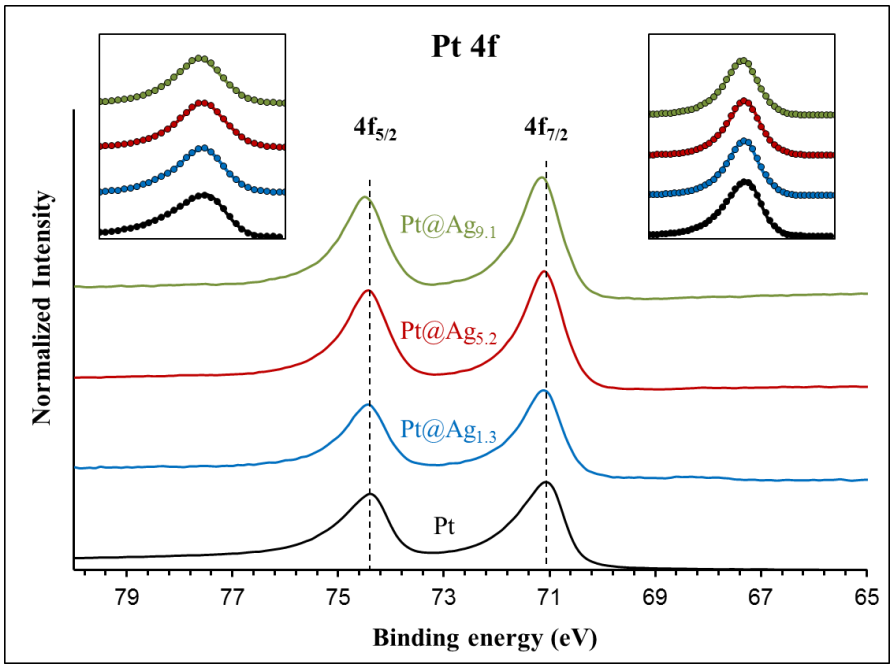

Figure 4.8. XPS spectra for platinum core particle (39.8 nm) (**A**) and $Pt_{39.8}@Ag_y$ particles with an optimal silver shell thickness of 1.3 (**B**); 5.2 (**C**); and 9.1 (**D**) nm. The inserted graphs show the Pt $4f_{7/2}$ and $4f_{5/2}$ peaks (solid curves) and the fitting with the asymmetric G-L mixed function (circles).

Both areas show single phase peaks with no signs of oxidation for each sample. Note that the silver nanoparticles also do not exhibit a characteristic oxide peak (such as that formed as a silver oxide layer on the silver NP surface) because the particles were synthesized under an inert atmosphere and were quickly transferred for the analysis, avoiding the characteristic oxidation. This simplifies the analysis of the electronic transfer by eliminating the overlapping oxide peak in the XPS spectra. Precise peak parameters were determined by using a Gaussian-Lorentzian (G-L) mixed function to fit the experimental data [18]. The inserts to each graph in figure 4.7 and 4.8 show the experimentally collected data (solid lines) as well as the fitted data using the G-L mixed function (dotted lines). Equation 4.2 describes the G-L mixed function while the derived peak parameters for Ag 3d area and Pt 4f area spectra are listed in table 4.2 and table 4.3, respectively.

Table 4.2. Peak parameters obtained by curve fit of Ag 3d peaks using a G-L mixed function.

		$Pt_{39.8}@Ag_{1.3}$	$Pt_{39.8}@Ag_{5.2}$	$Pt_{39.8}@Ag_{9.1}$	$Ag_{35.0}$
$3d_{5/2}$	Peak position	368.21	368.35	368.41	368.41
	FWHM	0.33	0.31	0.31	0.29
	M	0.79	0.87	0.84	0.90
	α	0	0	0	0
$3d_{3/2}$	Peak position	374.22	374.35	374.41	374.41
	FWHM	0.33	0.30	0.29	0.29
	M	0.94	0.85	0.84	0.83
	α	0	0	0	0
Spin-orbit intensity ratio		1.48	1.46	1.43	1.52

Table 4.3. Peak parameters obtained by curve fit of Pt 4f peaks using a G-L mixed function.

		$Pt_{39.8}@Ag_{1.3}$	$Pt_{39.8}@Ag_{5.2}$	$Pt_{39.8}@Ag_{9.1}$	$Pt_{39.8}$
$4f_{7/2}$	Peak position	71.09	71.10	71.13	71.23
	FWHM	0.46	0.46	0.47	0.46
	M	0.73	0.74	0.70	0.73
	α	0.09	0.06	0.09	0.10
$4f_{5/2}$	Peak position	74.43	74.43	74.47	74.56
	FWHM	0.45	0.47	0.47	0.44
	M	0.61	0.67	0.62	0.63
	α	0.12	0.08	0.09	0.13
Spin-orbit intensity ratio		1.36	1.34	1.35	1.39

The Gaussian-Lorentzian mixed function was used to analyze the Ag 3d peak shape[17]:

$$f(x) = \frac{l_0}{\{1 + M(x - x_0)^2/\Gamma^2\} exp\{(1 - M)\ln 2 (x - x_0)^2/\Gamma^2\}} \quad (4.2)$$

where l_0, x_0, x, Γ, and M are the peak height, the peak BE, the BE, a parameter for the peak width, and the G-L mixing ratio, respectively. To introduce the asymmetry into the G-L mixed function, the following variable transformation is incorporated in equation 4.2.[17]

$$(x - x_0) \rightarrow \frac{(x - x_0)}{\{1 + \alpha(x - x_0)/\Gamma\}} \tag{4.3}$$

For silver, there is a clear negative shift in the 3d peak energy for $Pt_{39.8}@Ag_y$ samples as compared to pure silver nanoparticles. The most pronounced shift is observed for the thinnest silver shell with peak energy moving back towards the value for pure silver as the silver shell thickness increases. The platinum 4f peak position also shows a subtle trend in the data with a negative energy shift in the peak position as compared to pure platinum nanoparticles, but in this case as the silver shell thickness increases, the platinum peak positions move slightly towards the expected position for pure platinum. The trends in the XPS spectra peak positions are summarized in Figure 4.9, which shows a plot of peak energy shift in silver 3d and platinum 4f peaks versus the silver shell thickness.

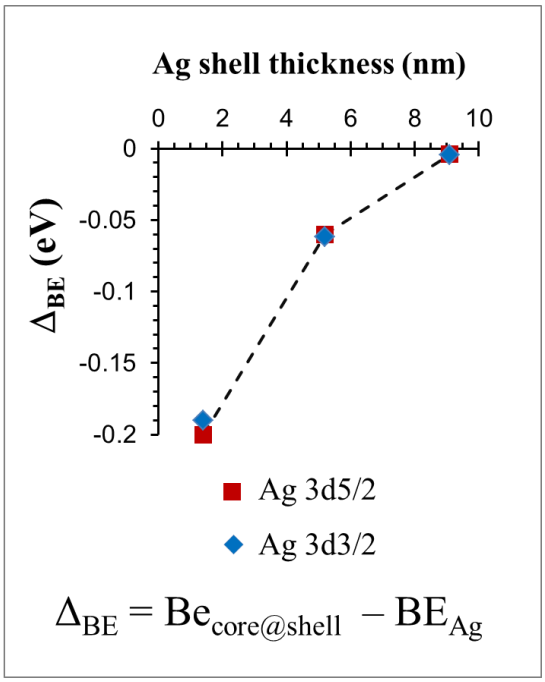

Figure 4.9. The Pt 4f and Ag 3d peak energy shift plotted as a function of silver shell thickness for $Pt_{39.8}@Ag_y$ (y = 1.3, 5.2, and 9.1 nm) nanoparticles. The peak energy shift $\Delta_{BE} = BE_{core\text{-}shell} - BE_{Pt}$ (or BE_{Ag}).

The lines connecting the data points in the graph are included to assist in visual assessment of the relative data point positions. The observations are broadly consistent with

an electron transfer phenomenon where the silver shell gains electron density from the core metal, in this case platinum.[9,11,18] The phenomenon is more pronounced for thinner silver shells because of the interfacial nature of the electron transfer and ultimately results in enhancement of the chemical properties of the silver shell. For instance, an electron rich silver shell is expected to become resistant to oxidation.[9,10,18] A simplified way to understand the observed shift in the XPS peaks is through the effect of relative electron density on the resulting binding energy of peaks in the XPS spectra. As silver gains electron density, it becomes relatively easier to remove electrons from silver sites, hence the binding energy is negatively shifted. For platinum, the 4f peak is also negatively shifted, which is counter intuitive, however this arises from the fact that the electronic transfer process is complex in nature. In reality, the true electronic configuration of the Pt@Ag NP structure may consist of electron donation and back-donation in various orbitals of the metals, which may account for the observation of a concurrent negative shift in silver 3d and platinum 4f orbitals. In addition, because platinum core nanoparticles actually consist of small platinum nanocrystals and have highly roughened surfaces while Pt@Ag nanoparticles have more smooth surfaces with relatively large silver grain sizes, there should be some differences in initial and final state effects of the electron emission process. This may be one of the reasons why the negative shift in platinum 4f peaks is observed. The electronic transfer phenomenon is supported by the observation of a sharp decrease in the BE shift for silver as the silver shell thickness increases, while for platinum the shift in binding energy only changes by a small degree. This shows that the electronic enrichment of silver in the 3d orbital is interfacial in nature, which can only arise in the electronic transfer process. A study on the electronic configuration of bare platinum versus coated nanoparticles using X-ray Absorption Near Edge Structure (XANES) analysis could provide additional information on the electronic configuration of these materials.[11]

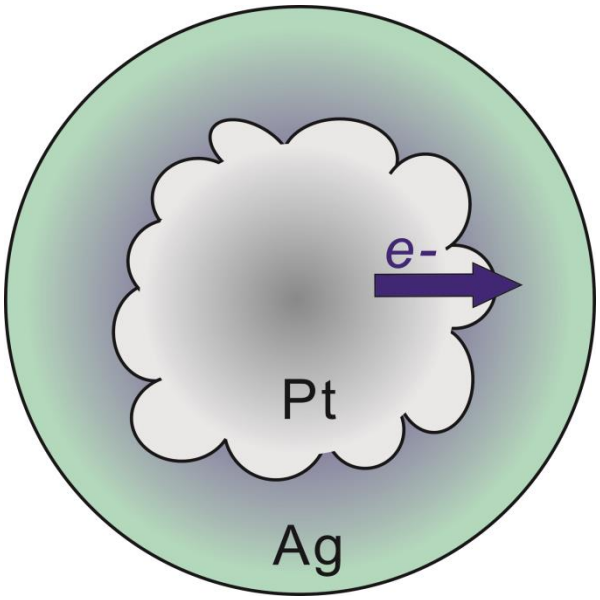

Scheme 4.1. Illustration of the particle structure and general electron transfer process. The purple color at the interface of platinum and silver represents the interfacial nature of the electron transfer.

4.2.4 Implication of the Electronic Properties to Sensing characteristics

The unique electronic properties displayed by the Pt@Ag NP system show that NP heterostructures can lead to materials with controllable and enhanced properties beyond what is offered by monometallic or alloyed NP systems. By controlling the structural parameters of these NP heterostructures, new or enhanced characteristics can be extracted such as resistance to oxidation, robustness, or maximizing plasmonic properties. Such ability is highly advantageous for use in sensing probe systems where these characteristics are critical for creating highly sensitive probes. In the Pt@Ag NP case, by avoiding the oxidation of silver, bio-molecular sensing probes can be formed which are reliable and highly sensitive because the probes do not undergo oxidative degradation. In addition, by understanding the electron transfer mechanism, the plasmonic properties of this class of core@shell structure can be further tailored for desired applications allowing sensing probes to be developed that possess higher sensitivity and accuracy.[18] In general, the electronic transfer can be understood as the enrichment of electron density at silver sites at the expense of electron density at platinum sites in the core@shell structure. The electronic characteristics are analogous to what would

occur in an alloy of platinum and silver, yet the nanostructures here exhibit clear phase segregation. As a result of the small Pt@Ag NP size, alloy-like electronic properties emerge at the interface of the two metals, which in this case is likely enhanced by the polycrystalline nature of the platinum NP core surface. The highly roughened surface of the platinum nanoparticles creates a larger surface area at the interface of platinum and silver in the core@shell structure. Because the electronic transfer phenomenon is interfacial in nature, this provides more sites for the electron transfer, leading to a relatively higher degree of electron enrichment for the silver shell. This observation is especially apparent when comparing the degree of electron transfer in the case of Au@Ag nanoparticles[9] and for the Pt@Ag particles created in this work. For 14.4 nm gold particles coated in a silver shell with a thickness of 1.0 nm, a negative shift of 0.1 eV in the Ag 3d peak in the XPS spectrum is observed, while for the $Pt_{39.8}Ag_{1.3}$ particles created here, a shift of nearly 0.2 eV is observed. While the core particle sizes in these two systems are different, the observation of accentuated electronic transfer in the case of using a platinum core in the Pt@Ag NP structure illustrates the potential for this system to express unique and enhanced sensing characteristics as a result of the strengthened electronic transfer. Scheme 4.1 represents the general structure and processes for electron transfer occurring in the Pt@Ag NP system, including representation of the interfacial nature of the phenomenon shown by the color gradient in the silver shell.

4.2.5 SERs activity of Pt@Ag core@shell nanoparticles

As-synthesized nanoparticles were taken for creating assemblies using 3-amino-1,2,4-triazole-5-thiol (ATT) and R6G. Then the assemblies were deposited onto the APTMS-modification glass substrate. Finally, the surface enhanced Raman scattering (SERS) activity of core@shell nanoparticles was investigated using ATT or R6G as a dual linker and reporter molecule using the same protocol reported previously.[19] The SERS activity was found to dramatically increase with increasing x in the case of the $Pt@Ag_x$ nanoparticles as shown in

figure 4.10 and figure 4.11 taking advantage of high extinction coefficients and extremely high field enhancements of Ag. Note that an Ar^+ ion laser (wavelength 514.5 nm) was used to obtain the Raman spectra. The intense Raman signals at about 1573, 1505, 1362,1307 and 1179 cm^{-1} arise from the totally symmetric modes of in-plane C-C stretching vibrations.

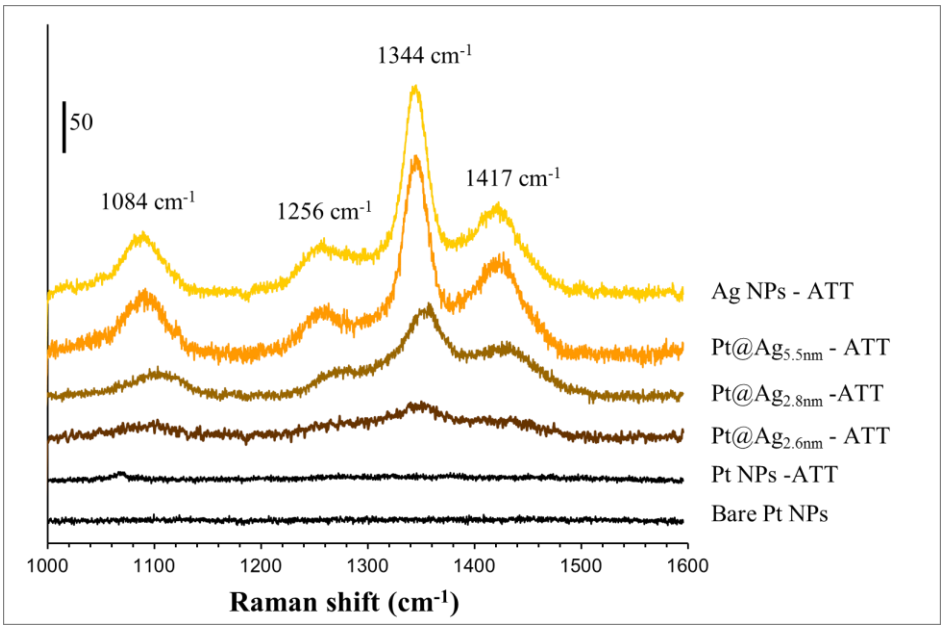

Figure 4.10. Raman spectra of Pt and Pt@Ag_x nanoparticle assemblies created by using ATT.

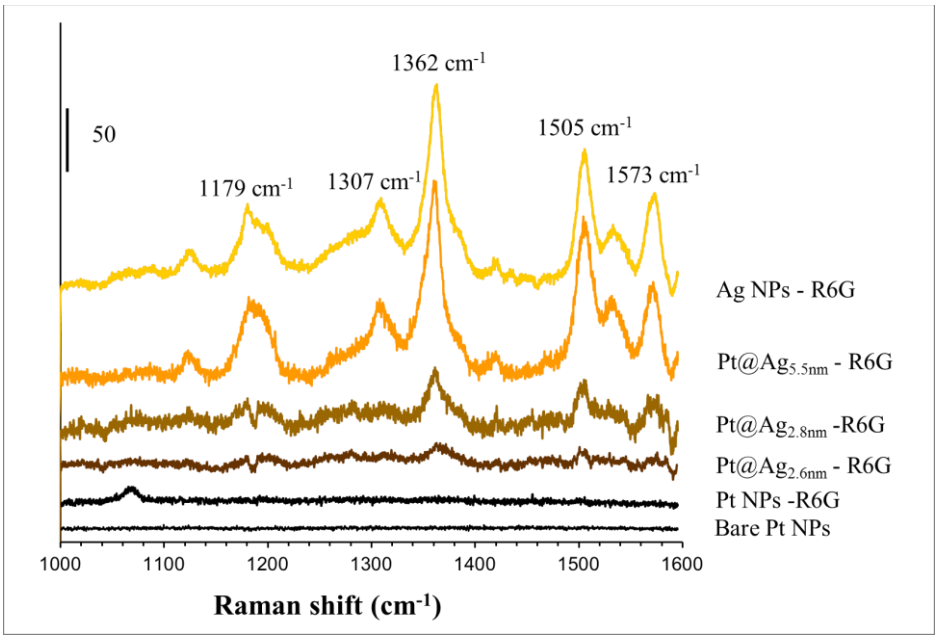

Figure 4.11. Raman spectra of Pt and Pt@Ag_x nanoparticle assemblies created by using R6G.

4.3 Conclusions

A series of platinum coated by silver (Pt@Ag) nanoparticles have been synthesized which display a well-defined structure where polycrystalline platinum particles are completely encapsulated in a continuous monocrystalline silver shell. The understanding of the electron transfer phenomenon in the platinum-silver NP system enhances the ability to purposely manipulate the stability and plasmonic properties of core@shell NP sensing probes and provides fundamental insight into the electronic characteristics of nano-heterostructures. The Pt@Ag particles display surface plasmon resonance properties which could be exploited in plasmonic sensing probe applications. More significantly, these nanoparticles display unique electronic properties where the silver shell gains electron density from the platinum cores, as revealed by analysis of the XPS spectra of these materials. These unique electronic properties give insight into how this class of heterostructured NP can be manipulated to create new and powerful sensing probes with enhanced properties such as oxidation resistance, robustness, plasmonic activity and other properties.

4.4 References

(1) Dao, A. T. N.; Mott, D. M.; Higashimine, K.; Maenosono, S. *Sensors* **2013**, *13*, 7813.

(2) Lim, S. I.; Zhong, C.-J. *Acc. Chem. Res.* **2009**, *42*, 798.

(3) Wang, L.; Shi, X.; Kariuki, N. N.; Schadt, M.; Wang, G. R.; Rendeng, Q.; Choi, J.; Luo, J.; Lu, S.; Zhong, C.-J. *J. Am. Chem. Soc.* **2007**, *129*, 3.

(4) Rosi, N. L.; Mirkin, C. *Chem. Rev.* **2005**, *105*, 1547.

(5) Mott, D.; Thuy, N. T. B.; Aoki, Y.; Maenosono, S. *Phil. Trans. R. Soc. A* **2010**, *368*, 4275.

(6) Ma, Y.; Li, W.; Cho, E. C.; Li, Z.; Yu, T.; Zeng, J.; Xie, Z.; Xia, Y. *ACS Nano* **2010**, *4*, 6725.

(7) Rodríguez-González, B.; Burrows, A.; Watanabe, M.; Kiely, C. J.; Marzán, L. M. L. *J. Mater. Chem.* **2005**, *15*, 1755.

(8) Lu, X.; Tuan, H.-Y.; Chen, J.; Li, Z.-Y.; Korgel, B.; Xia, Y. *J. Am. Chem. Soc.* **2007**, *129*, 1733.

(9) Dao, A. T. N.; Singh, P.; Shankar, C.; Mott, D.; Maenosono, S. *Appl. Phys. Lett.* **2011**, *99*, 073107.

(10) Shankar, C.; Dao, A. T. N.; Singh, P.; Higashimine, K.; Mott, D. M.; Maenosono, S. *Nanotechnology* **2012**, *23*, 245704.

(11) Nishimura, S.; Dao, A. T. N.; Mott, D.; Ebitani, K.; Maenosono, S. *J. Phys. Chem. C* **2012**, *116*, 4511.

(12) Bigall, N. C.; Härtling, T.; Klose, M.; Simon, P.; Eng, L. M.; Eychmüller, A. *Nano Lett.* **2008**, *8*, 4588.

(13) Mott, D. M.; Mai, N. T.; Thuy, N. T. B.; Sakata, T.; Higashimine, K.; Koyano, M.; Maenosono, S. *J. Phys. Chem. C* **2011**, *115*, 17334.

(14) *Reference data accessed from the International Centre for Diffraction Data database, 2012. Card number 00-004-0802 for fcc platinum.*

(15) *Reference data accessed from the International Center for Diffraction Data database, 2012. Card number 00-004-0783 for fcc silver.*

(16) Dutta, S.; Ganguly, B. N. *J. Nanobiotechnol.* **2012**, *10*, 29.

(17) Maenosono, S.; Lee, J.; Dao, A. T. N.; Mott, D. *Surf. Interface Anal.* **2012**, *44*, 1611.

(18) Mott, D. M.; Anh, D. T. N.; Singh, P.; Shankar, C.; Maenosono, S. *Adv. Colloid Interface Sci.* **2012**, *185-186*, 14.

(19) Singh, P.; Thuy, N. T. B.; Aoki, Y.; Mott, D.; Maenosono, S. *J. Appl. Phys.* **2011**, *109*, 094301.

Chapter 5. Correlation of Charge-Transfer Effect and Chemical Stability of Nanoparticles

5.1 Elucidation of charge-transfer effect in multi-metallic nanoparticle systems

5.1.1 Charge-transfer in Ag shell with different core materials

In order to gain a diagnostic assessment of the electronic properties of the silver shell in different core@shell nanoparticles, XPS analysis was performed on a series of Au@Ag and Pt@Ag nanoparticles with increasing shell thickness (see more at section 3.2.3 and 4.2.3). In both cases, binding energy of Ag 3d in core@shell nanoparticles shows a negative shift compared to that of pure Ag nanoparticles. The results also indicate that the charge-transfer effect only happen in the interface between the core and Ag shell.[1] When the Ag shell increases, Ag 3d binding energy will be different nature depending on position. In the other words, Ag 3d orbital which is near Au surface will have higher electron density and that of the Ag 3d orbital far from the interface will be dominated by Ag nature.[2] However, in XPS data, binding energy will be more likely the average, which means the thicker Ag shell thickness is, the binding energy shift will decreases toward zero. Therefore, if we consider the binding energy of Ag 3d in core@shell nanoparticles which has the thickest shell has closest value to that of Ag 3d in pure Ag metallic nanoparticle, we will be able to precisely calculate the binding energy shift of Ag 3d in different Ag shell thickness. Figure 5.1 shows binding energy of Ag 3d peaks are plotted as a function of Ag composition in Au@Ag and Pt@Ag core@shell nanoparticles with different shell thicknesses. We can clearly see when the Ag shell thickness increases, which means the relative composition of Ag to core metal also increases, the binding energy shifts toward higher energy region. However, the binding energy shift of nanoparticle has Ag composition from 17% to 70% in the case of Au@Ag system (~0.05eV) is much smaller than that of Pt@Ag (~0.18eV) system. This is due to the nature characteristic of core surfaces. While surface of Au core is very smooth, Pt core has very rough surface

(figure 4.6). This leads to increase the surface area which in contact with Ag shell. As we knew that the charge-transfer mostly happens in the interface of core and shell metal, the increase of surface area between two systems which has the similar composition ratio should increase the charge-transfer effect. It indicates that binding energy of Ag 3d will shift more strongly toward lower energy region.

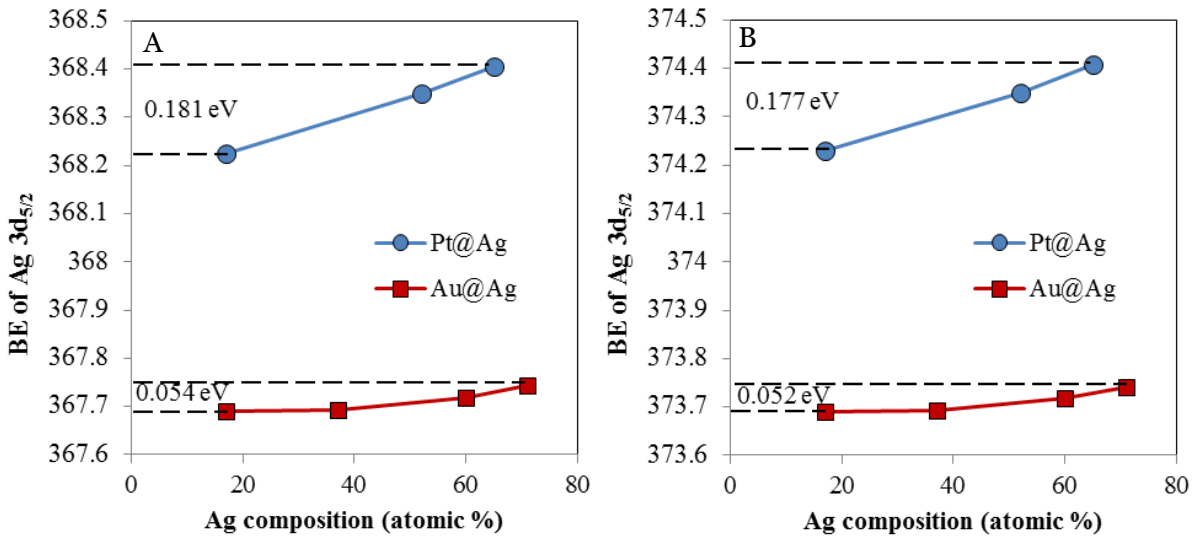

Figure 5.1. Binding energy of Ag 3d peaks are plotted as a function of Ag composition in Au@Ag and Pt@Ag core@shell nanoparticles with different shell thicknesses. Ag 3d XPS spectra has 2 components as (A) $3d_{5/2}$ and (B) $3d_{3/2}$.

In the other hand, the corresponding of Au 4f and Pt 4f orbitals is not that simple and straightforward (figure 5.2). The reason is Ag 3d orbital doesn't directly receipt the electron from 4f orbital of core metal. And the decreasing in electron density of 4f orbital of core metal most likely comes from the increasing in 5d vacancies population of the same metal.[3] However, figure 5.2 shows that the binding energy of Au 4f and Pt 4f is always positive compare to that of pure Au and pure Pt nanoparticles. This strongly indicates the charge-transfer effect from the core metal to Ag shell.

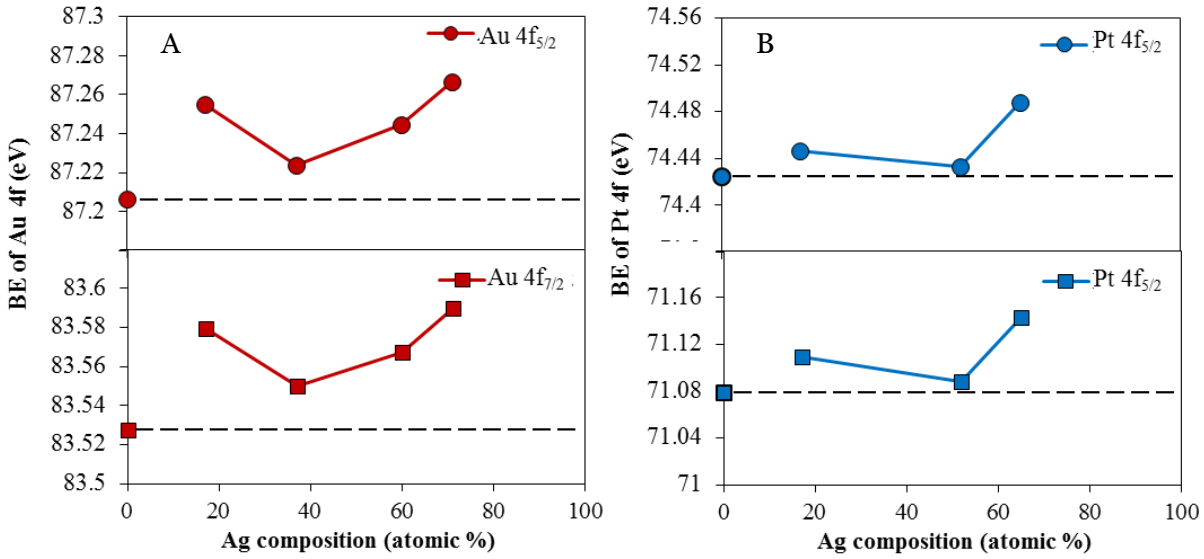

Figure 5.2. Binding energy of (A) Au 4f peaks and (B) Pt 4f peaks are plotted as a function of Ag composition in Au@Ag and Pt@Ag core@shell nanoparticles with different shell thicknesses. Binding energy at Ag composition equal zero is the binding energy of Au core and Pt core nanoparticles withouth coating.

Figure 5.3 shows the comparison of Au 4f and Pt 4f binding energy shift when increasing Ag shell thickness. The results show no significant difference between binding energy shift of Au 4f and Pt 4f. However, Pt 4f binding energy shift is slightly smaller than that of Au 4f. This could be explained by the phenomenon when we combine these two metals in one system. In Au@Pt core@shell nanoparticles, there is a positive shift in binding energy of Au 4f (figure 5.4) and negative shift in binding energy of Pt 4f. It means there is a chance of electronic charge-transfer from Au to Pt despite the similar nature of these two elements. Therefore, the charge-transfer effect from Au to Ag should be stronger than from Pt to Ag which leads to the positive shift in binding energy of Au 4f in Au@Ag is slightly higher than Pt 4f in Pt@Ag core@shell nanoparticles. This should not be confused with the negative shift of Ag 3d in Au@Ag and Pt@Ag which we mentioned above. Once again, it should be emphasized that despite the stronger nature of charge-transfer effect caused by Au, the percentage of interface atoms in Pt core still dominant and enhance the electron density in Ag 3d .

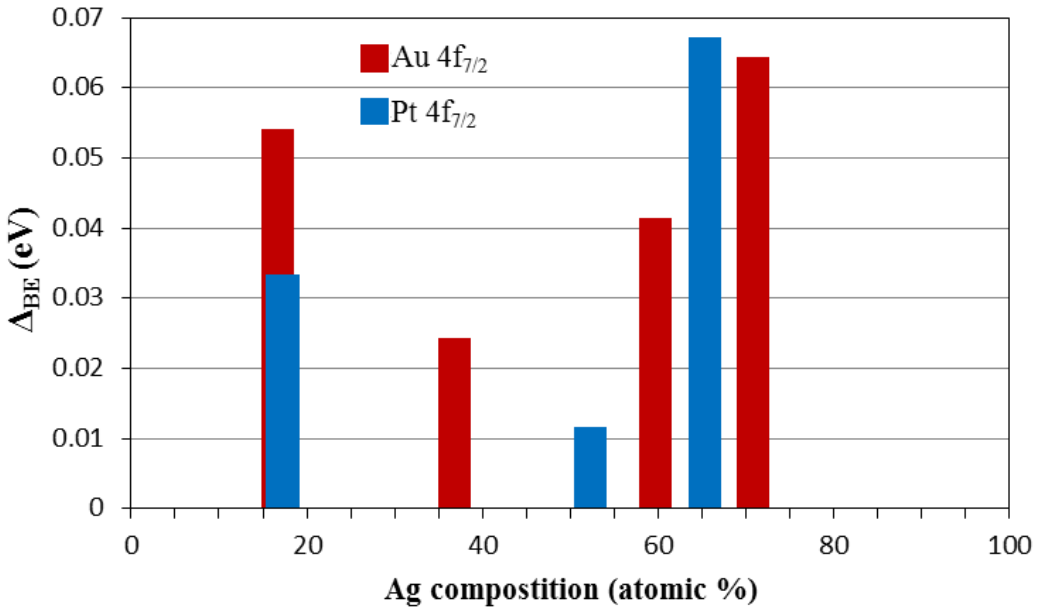

Figure 5.3. Binding energy shifts of Au $4f_{7/2}$ and Pt $4f_{7/2}$ peaks are plotted as function of Ag composition in Au@Ag and Pt@Ag core@shell nanoparticles with different shell thicknesses. The peak energy shift $\Delta_{BE} = BE_{core@shell} - BE_{Ag}$.

5.1.2 Charge-transfer in Au core with different shell materials

Charge-transfer is not a one way effect. It's the electron donation and back donation from orbital to orbital between different metallic atoms in one system. In order to prove this assumption, we carried out the XPS measurement of core@shell nanoparticles composed Au in the core and different metal in the shell. All the core@shell nanoparticles in this experiment have the shell thickness no larger than 1 nm in order to assure about the clear occurrence of charge-transfer effect. And the Au cores are the same size, shape and surface property in every case.

Figure 5.4 shows binding energy shifts of Au 4f peaks in different core@shell nanoparticles: Au@Ag, Au@Fe, Au@Cu, and Au@Pt. In most cases, Au 4f peaks binding energy show positive shift which indicate the electron transfer from Au core to the shell. Beside Pt has high oxidation resistance in nature, Ag and Cu metal in the shell also doesn't show any oxidation state. Meanwhile, Au 4f peaks binding energy in Au@Fe core@shell

nanoparticles show a small negative shift. Without assuring that the charge-transfer in this case happen in opposite direction, Fe shell to Au core, we believe that the arising of electron density in Au 4f indicate that the charge-transfer effect in this case couldn't improve the oxidation resistance of Fe shell. Fe in the shell of Au@Fe core@shell nanoparticles has similar oxidation states as in pure Fe nanoparticles and no Fe^0 could be observed.[4]

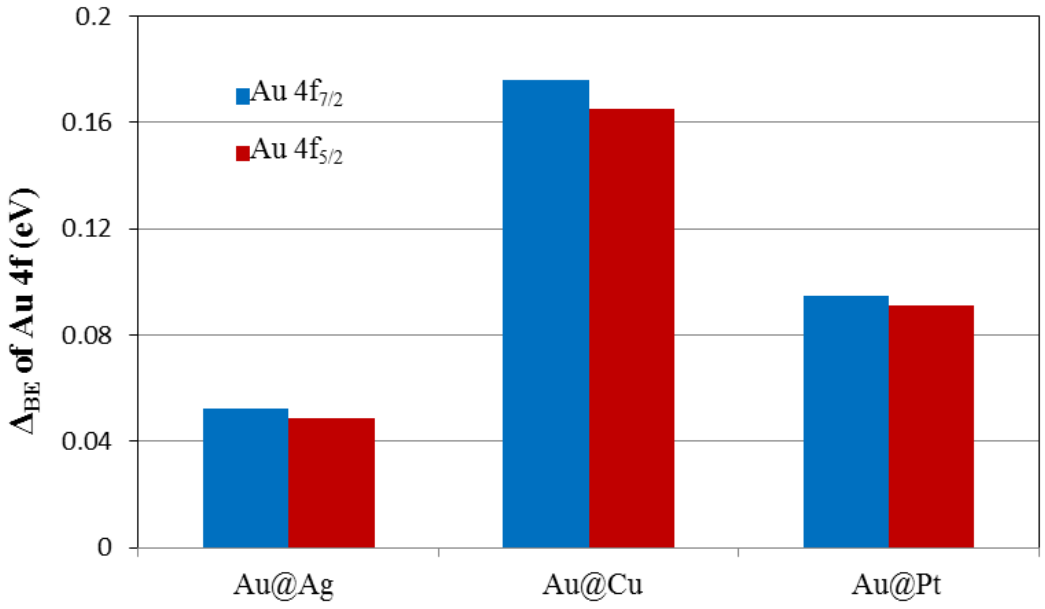

Figure 5.4. Binding energy shifts of Au 4f peaks in different core@shell nanoparticles. The peak energy shift $\Delta_{BE} = BE_{core@shell} - BE_{Au}$.

5.2 Impact of charge-transfer effect on chemical stability of metallic nanoparticles

In order to understand how charge-transfer effect on chemical stability of metal, we study the oxidation state of shell materials in different core@shell systems. Figure 5.5 show XPS spectra for Ag, Cu, and Pt in the shell of core@shell nanoparticles. In the case of Ag, Cu and Pt, we only observe one main peak of pure metal. For the shell thickness less than 1 nm, the charge-transfer effect is strong enough to prevent the oxidation of the metal in the shell.

$$Au \rightleftharpoons Au^{3+} + 3e \qquad E^0 = +1.52\ V$$

$$Pt \rightleftharpoons Pt^{2+} + 2e \qquad E^0 = +1.188\ V$$

$$Ag \rightleftharpoons Ag^{+} + 1e \qquad E^0 = +0.8\ V$$

$$Cu \rightleftharpoons Cu^{2+} + 2e \qquad E^0 = +0.34\ V$$

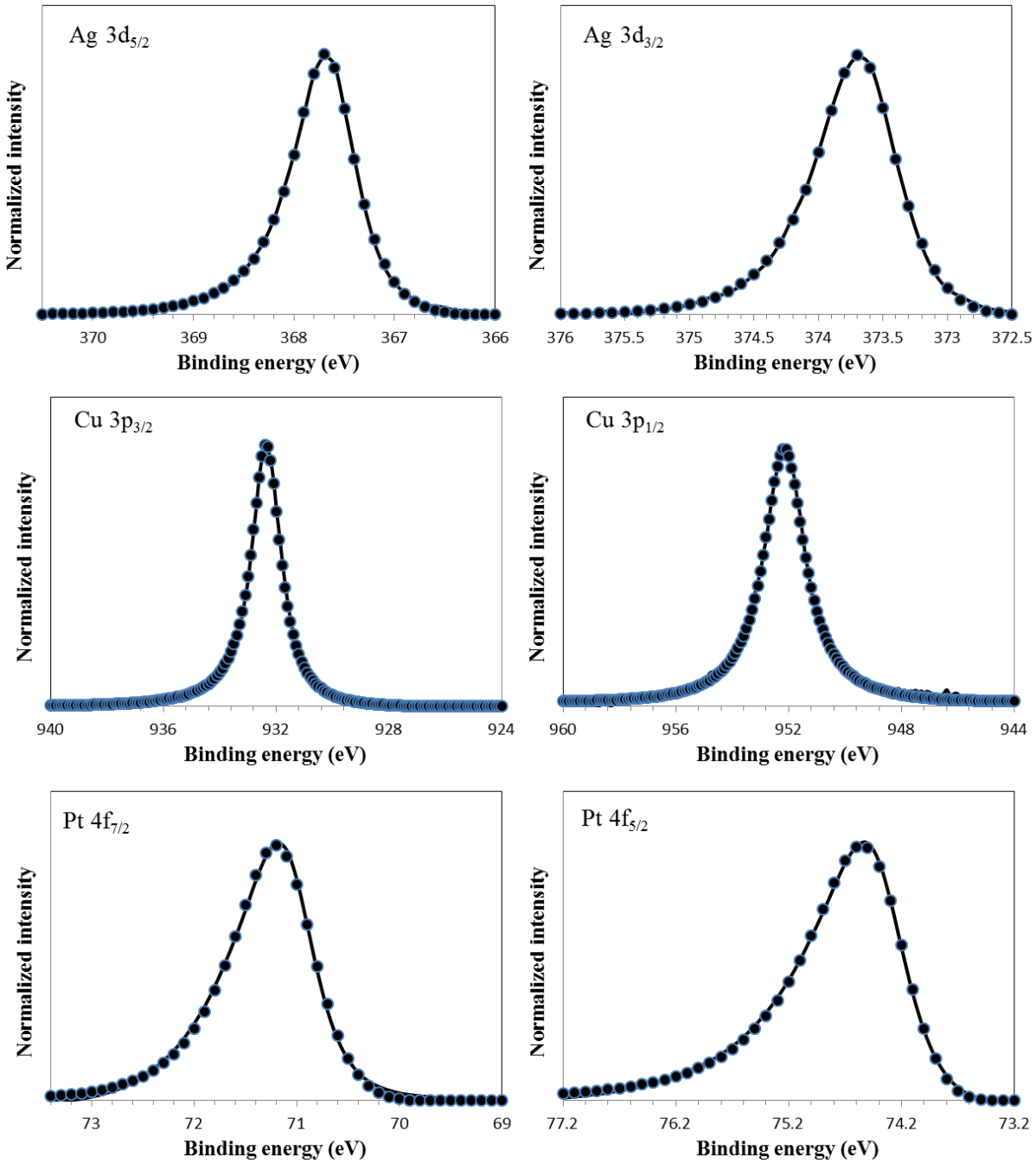

Figure 5.5. XPS spectra for Ag, Cu and Pt in the shell of core@shell nanoparticles. The graphs show the raw data (solid curves) and the fitting with the asymmetric G-L mixed function (circles).

5.3 References

(1) Dao, A. T. N.; Singh, P.; Shankar, C.; Mott, D.; Maenosono, S. *Appl. Phys. Lett.* **2011**, *99*, 073107.

(2) Maenosono, S.; Lee, J.; Dao, A. T. N.; Mott, D. *Surf. Interface Anal.* **2012**, *44*, 1611.

(3) Nishimura, S.; Dao, A. T. N.; Mott, D.; Ebitani, K.; Maenosono, S. *J. Phys. Chem. C* **2012**, *116*, 4511.

(4) Singh, P.; Mott, D. M.; Maenosono, S. *Chem. Phys. Chem.* **2013**, *14*, 1.

Chapter 6. Conclusions and Future Plan

6.1 Summary results

In summary, we have found that an electron transfer from the Au core to the Ag shell takes place in Au@Ag core@shell nanoparticles resulting in an enhancement of the oxidation resistivity of the Ag shell. The enhanced oxidation resistivity of the Ag shell effectively suppresses the galvanic replacement reaction during the Au second shell deposition process, and thus, the resultant (Au@Ag)@Au double shell nanoparticles have a uniform size, shape and structure without defects which cannot be avoided in the case of Ag@Au NP syntheses. Using the charge-transfer-induced electronic modification technique, one can synthesize well-defined core@shell nanoparticles which have not been achieved until now. The (Au@Ag)@Au double shell nanoparticles are highly stable in presence of salt with high Raman activity.

A series of platinum coated by silver (Pt@Ag) nanoparticles have been synthesized which display a well-defined structure where polycrystalline platinum particles are completely encapsulated in a continuous monocrystalline silver shell. The understanding of the electron transfer phenomenon in the platinum-silver NP system enhances the ability to purposely manipulate the stability and plasmonic properties of core@shell NP sensing probes and provides fundamental insight into the electronic characteristics of nano-heterostructures. The Pt@Ag particles display surface plasmon resonance properties which could be exploited in plasmonic sensing probe applications. More significantly, these nanoparticles display unique electronic properties where the silver shell gains electron density from the platinum cores, as revealed by analysis of the XPS spectra of these materials.

The unique electronic properties give insight into how this class of heterostructured NP can be manipulated to create new and powerful sensing probes with enhanced properties such as oxidation resistance, robustness, plasmonic activity and other properties. These

particles are ultimately expected to lead to a novel class of highly active and stable nanoprobes for bio-molecular sensing and diagnostics.

6.2 Originality and novelty of the research

Plasmonic metallic nanoparticles have been explored extensively in terms of their fundamental and practical applications such as for optoelectronic devices,[1,2] optical metamaterials,[3,4] sensors,[3,5–10] and solar cells[11,12] as well as many others. During the past decade the concomitant rapid development of plasmonics into a vibrant sub-area of nanotechnology has focused almost entirely on Au and Ag as (nano) plasmonic metals. Ag provides high enhanced-Raman activity, while the Au provides excellent chemical stability and a great reactivity with sulfur containing biomolecules, which has inevitably leaded to the combination of Au and Ag in a single nanoparticle system.[13–20] The synthetic approach to Au-Ag nanoparticles still has many obstacles. Aqueous synthesis techniques for Ag nanoparticles are advantageous for biological applications because the resulting nanoparticles can often be used directly, yet these techniques typically provide unstable Ag nanoparticles of low monodispersity, or with a size that is difficult to control.[5,14,21,22] In addition, it is still challenging to synthesize well-defined uniform Ag@Au nanoparticles because the Ag core is easily etched away due to the galvanic replacement reaction between Au ions and the Ag metal cores which causes gaps in the Au shell or hollow sections at the interface of the core and the shell.[14,16,20,22–26] There are also several attempts to create Au@Ag core@shell nanoparticles. However, the synthetic approach seemed not efficient enough to obtain uniform and controllable morphology and composition of the core@shell nanoparticles.[26–28] We have been successful in synthesizing Au@Ag core@shell nanoparticles with uniform morphology and tunable size and composition. The synthetic approach is straightforward with citrate reduction and the products don't require complicated treatment process for further uses. In addition, Au@Ag core-shell nanoparticles were demonstrated to have better chemical stability than pure Ag nanoparticles and very high SERS activity together with

tunable size, shell thickness and plasmonic properties. Moreover, Ag in the shell also could suppress the galvanic replacement reaction allowing the formation of double shell (Au@Ag)@Au nanoparticles without any defects or gaps in the structure.[29] Double shell nanoparticles have shown excellent stability with controllable characteristics and very high SERs activity. All of these attractive aspects arise from the electron transfer phenomenon which has been shown to occur in the Au-Ag system. [29–31] Liz Marzán and coworkers have synthesized Au@Ag, Au@Ag@Au and finally Au@Ag@Au@Ag multishell NPs.[32] In their approach however, the deposited intermediate Ag shell thickness was much greater than our own (ca. 32 nm), which resulted in the formation of hollow structures with partial alloying when the Au shell was deposited. In our own study, the intermediate Ag shell thickness is limited to the range where the charge transfer phenomenon takes place, allowing the ability to create Au@Ag@Au NPs without significant alloying or defects in the structure.

By extending this phenomenon to other silver based NP systems, insight can be gained into how to manipulate the particle structure and composition towards the desired characteristics. With this goal in mind, we created a series of different sized platinum particles and coated them in silver shells of various thicknesses. In this case, platinum was chosen as a core material because of its status as a noble metal, its *fcc* crystal structure (the same as for silver), and its chemical similarity to gold. The resulting particles were characterized in terms of their structural/composition properties, and then the electronic properties of these probes were analyzed by using X-Ray Photoelectron Spectroscopy. The results demonstrate that the electronic transfer phenomenon can be extended to a wide range of heterostructure systems, and provides insight into how to exploit electronic transfer to create silver based sensing probes with enhanced robustness, high optical/plasmonic activity and plasmonic characteristics that can be tuned for a desired application. In addition, nanoparticles which are composed of Au, Ag or Pt are promising not only in biosensing and diagnostics applications but also are a good candidate for medical – therapy or catalyst applications.

Electron transfer or charge transfer phenomenon is very attractive as a route to manipulate the properties of materials and also presents a complex challenge. Understanding the mechanism of operation and its effect to materials characteristics can lead us to systematically design materials with distinct characteristics for specific applications. Charge-transfer or charge-redistribution term has been mentioned before in several researches but mostly focused on the alloy structure of the nanoparticles and the correlation of this effect to metallic nanoparticles characteristics hadn't been discussed.[3334,35] My PhD research attempted to make clear the controllability of electron transfer phenomenon specifically in multi-metallic nanomaterials. In order to have the full picture of electron transfer phenomenon, we clarify the interaction among three noble metals (Ag, Au and Pt) by comparing Au-Ag, Pt-Ag and Au-Pt in homogeneous and heterogeneous nanostructure. Furthermore, we have discussed the impact of charge-transfer effect on metallic nanoparticles characteristics, such as stability and plasmonic properties. This fundamental research will provide scientists with a useful tool in understanding, designing and controlling the properties of metallic nanomaterials. In our laboratory research, electron transfer effect has been indeed utilized in designing and synthesizing several multi-metallic nanoparticle structure in order to modify and stabilize metal phase, such as Au@Fe core@shell, Au@Cu core@shell, ZnSb nanoparticles with Sb rich in the core and Zn rich in the shell, FeCo@Ag core@shell nanoparticles, etc.

6.3 Future plan

The purpose of my future research plan is to develop a novel and unique sensing probe that will be used to detect C-reactive protein more accurately, quickly and with lower cost than traditional detection methods. This will be accomplished by harnessing the attractive characteristics of the electronic transfer phenomenon developed in my graduate research to create a new class of active and robust sensing probe that will be used in the practical detection of C-reactive protein. C-reactive protein is an important biological marker that is

constantly produced by the liver in the human body. The level of C-reactive protein present in the body is an indicator for inflammation and has been used as a specific marker for heart disease or infection, as a result it is highly important to be able to detect the molecule quickly and accurately to identify those people at high risk of heart disease. The detection of C-reactive protein is occasionally conducted using traditional techniques such as ELISA, which is time consuming, expensive, and requires highly skilled personnel to operate.[36] There have been some initial studies into using magnetic nanoparticles for the detection of C-reactive protein, but these still suffer from low reliability, sensitivity and ease of use.[36] Consequently, there is a great need to develop a sensing technique for C-reactive protein that is highly accurate, can be administered anywhere, and provides quick results that can be interpreted by anyone. In this research project, these goals will be achieved through the development of multi-component FePt@Au@Ag nanoparticles (iron platinum alloy coated in gold coated in silver) which will be employed as a probe for the fast, accurate, and mobile detection of C-reactive protein.

6.4 References

(1) Gole, A.; Murphy, C. J. *Chem. Mater.* **2004**, *16*, 3633.

(2) Daniel, M.-C.; Astruc, D. *Chem. Rev.* **2004**, *104*, 293.

(3) Hutter, E.; Fendler, J. H. *Adv. Mater.* **2004**, *16*, 1685.

(4) Mayer, K. M.; Hafner, J. H. *Chem. Rev.* **2011**, *111*, 3828.

(5) Murphy, C. J.; Gole, A. M.; Hunyadi, S. E.; Orendorff, C. J. *Inorg. Chem.* **2006**, *45*, 7544.

(6) Love, J. C.; Estroff, L. A.; Kriebel, J. K.; Nuzzo, R. G.; Whitesides, G. M. *Chem. Rev.* **2005**, *105*, 1103.

(7) Murphy, C. J.; Gole, A. M.; Hunyadi, S. E.; Stone, J. W.; Sisco, P. N.; Alkilany, A.; Kinard, B. E.; Hankins, P. *Chem. Commun.* **2008**, 544.

(8) Sepúlveda, B.; Angelomé, P. C.; Lechuga, L. M.; Liz-Marzán, L. M. *Nano Today* **2009**, *4*, 244.

(9) Lim, I.-I. S.; Zhong, C.-J. *Gold Bull.* **2007**, *40*, 59.

(10) Lee, J.-S.; Ulmann, P. A.; Han, M. S.; Mirkin, C. A. *Nano Lett.* **2008**, *8*, 529.

(11) Link, S.; Wang, Z. L.; El-Sayed, M. A. *J. Phys. Chem. B* **1999**, *103*, 3529.

(12) Barnes, W. L.; Dereux, A.; Ebbesen, T. W. *Nature* **2003**, *424*, 824.

(13) Mallin, M. P.; Murphy, C. J. *Nano Lett.* **2002**, *2*, 1235.

(14) Singh, P.; Thuy, N. T. B.; Aoki, Y.; Mott, D.; Maenosono, S. *J. Appl. Phys.* **2011**, *109*, 094301.

(15) Ma, Y.; Li, W.; Cho, E. C.; Li, Z.; Yu, T.; Zeng, J.; Xie, Z.; Xia, Y. *ACS Nano* **2010**, *4*, 6725.

(16) Pearson, A.; O'Mullane, A. P.; Bansal, V.; Bhargava, S. K. *Chem. Commun.* **2010**, *46*, 731.

(17) Drube, W.; Treusch, R. *Phys. Rev. B* **1998**, *58*, 6871.

(18) Lee, K.-S.; El-Sayed, M. A. *J. Phys. Chem. B* **2006**, *110*, 19220.

(19) Maye, M. M.; Luo, J.; Han, L.; Kariuki, N. N.; Zhong, C.-J. *Gold Bull.* **2003**, *36*, 75.

(20) Ferrer, D. A.; Diaz-Torres, L. A.; Wu, S.; Jose-Yacaman, M. *Catal. Today* **2009**, *147*, 211.

(21) Sharma, V. K.; Yngard, R. A.; Lin, Y. *Adv. Colloid Interface Sci.* **2009**, *145*, 83.

(22) Mott, D.; Thuy, N. T. B.; Aoki, Y.; Maenosono, S. *Phil. Trans. R. Soc. A* **2010**, *368*, 4275.

(23) Skrabalak, S. E.; Chen, J.; Sun, Y.; Lu, X.; Au, L.; Cobley, C. M.; Xia, Y. *Acc. Chem. Res.* **2008**, *41*, 1587.

(24) Mott, D.; Lee, J.; Thuy, N. T. B.; Aoki, Y.; Singh, P.; Maenosono, S. *Jpn. J. Appl. Phys.* **2011**, *50*, 065004.

(25) Cui, Y.; Ren, B.; Yao, J.-L.; Gu, R.-A.; Tian, Z.-Q. *J. Phys. Chem. B* **2006**, *110*, 4002.

(26) Yang, Y.; Shi, J.; Kawamura, G.; Nogami, M. *Scr. Mater.* **2008**, *58*, 862.

(27) Gong, X.; Yang, Y.; Huang, S. *J. Phys. Chem. C* **2010**, *114*, 18073.

(28) Lim, D.-K.; Kim, I.-J.; Nam, J.-M. *Chem. Commun.* **2008**, 5312.

(29) Dao, A. T. N.; Singh, P.; Shankar, C.; Mott, D.; Maenosono, S. *Appl. Phys. Lett.* **2011**, *99*, 073107.

(30) Mott, D. M.; Anh, D. T. N.; Singh, P.; Shankar, C.; Maenosono, S. *Adv. Colloid Interface Sci.* **2012**, *185-186*, 14.

(31) Nishimura, S.; Dao, A. T. N.; Mott, D.; Ebitani, K.; Maenosono, S. *J. Phys. Chem. C* **2012**, *116*, 4511.

(32) Rodríguez-González, B.; Burrows, A.; Watanabe, M.; Kiely, C. J.; Marzán, L. M. L. *J. Mater. Chem.* **2005**, *15*, 1755.

(33) Kuhn, M.; Sham, T. K. *Phys. Rev. B* **1994**, *49*, 1647.

(34) Tyson, C. C.; Bzowski, A.; Kristof, P.; Kuhn, M.; Sammynaiken, R.; Sham, T. K. *Phys. Rev. B* **1992**, *45*, 8924.

(35) Bzowski, A.; Yiu, Y. M.; Sham, T. K. *Phys. Rev. B* **1995**, *51*, 9515.

(36) Lin, Y.-J.; Yang, J.-Y.; Shu, T.-Y.; Lin, T.-Y.; Chen, Y.-Y.; Su, M.-Y.; Li, W.-J.; Liu, M.-Y. *J. Chromatogr. A* **2013**, *1315*, 188.

Appendix I

for

Cyclic voltammetry measurements of Au and Au@Ag nanoparticles

A1.1 Fundamentals of cyclic voltammetry

Cyclic voltammetry (CV) is an electrochemical technique which measures the current that develops in an electrochemical cell under conditions where voltage is in excess of that predicted by the Nernst equation. CV is performed by cycling the potential of a working electrode, and measuring the resulting current. The effectiveness of CV results from its capability for rapidly observing the redox behavior over a wide potential range.

CV consists of cycling the potential of an electrode, which is immersed in an unstirred solution, and measuring the resulting current. The potential of this working electrode is controlled versus a reference electrode such as a saturated calomel electrode (SCE) or a silver/silver chloride electrode (Ag/AgCl). The controlling potential which is applied across these two electrodes can be considered an excitation signal. The excitation signal for CV is a linear potential scan with a triangular waveform as shown in figure A1.1.[1] This triangular potential excitation signal sweeps the potential of the electrode between two values, sometimes called the switching potentials. The scan rate is reflected by the slope. Single or multiple cycles can be used.

A cyclic voltammogram is obtained by measuring the current at the working electrode during the potential scan. The current can be considered the response signal to the potential excitation signal. The behavior of the current during the potential scan can be understood by carefully examining the concentration-distance profiles (*C-x* profiles). The current is proportional to the slope of the *C-x* profiles at the electrode surface as described by

$$i = nFAD\left(\frac{\partial C}{\partial x}\right)_{x=0} = K\left(\frac{\partial C}{\partial x}\right)_{x=0} \quad \text{(A1.1)}$$

where i is the current, n is the number of electrons transferred per ion, A is electrode area, D is diffusion coefficient, C is the concentration, and x is the distance from the electrode.

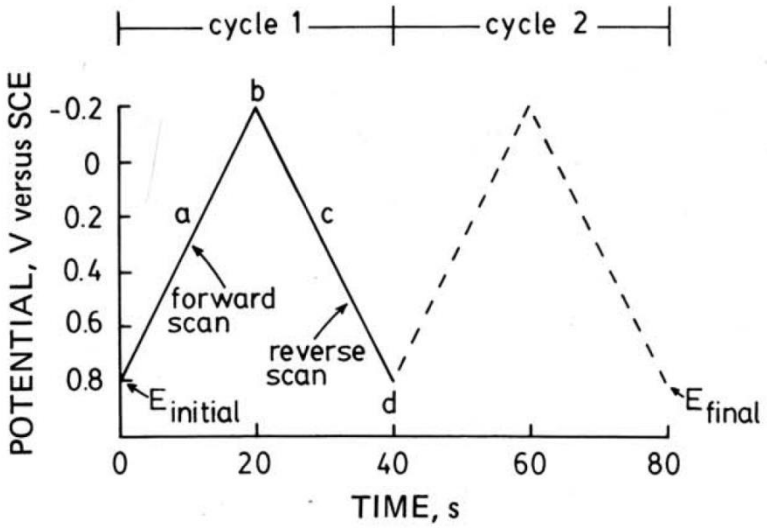

Figure A1.1. Typical excitation signal for CV - a triangular potential waveform with switching potentials at 0.8 and –0.2 V versus SCE.[1]

The important parameters of a cyclic voltammogram are the magnitudes of the anodic peak current (i_{pa}), cathodic peak current (i_{pc}), the anodic peak potential (E_{pa}) and cathodic peak potential (E_{pc}) (Fig. A1.2a). A redox couple in which both species rapidly exchange electrons with the working electrode is termed an electrochemical reversible couple. The formal reduction potential $E^{o\prime}$ for a reversible couple is

$$E^{o\prime} = \frac{E_{pa} + E_{pc}}{2} \quad \text{(A1.2)}$$

Figure A1.2b shows the voltammogram for a quasi-reversible reaction for different values of the reduction and oxidation rate constants. The first curve shows the case where both the oxidation and reduction rate constants are still fast, however, as the rate constants are lowered the curves shift to more reductive potentials.

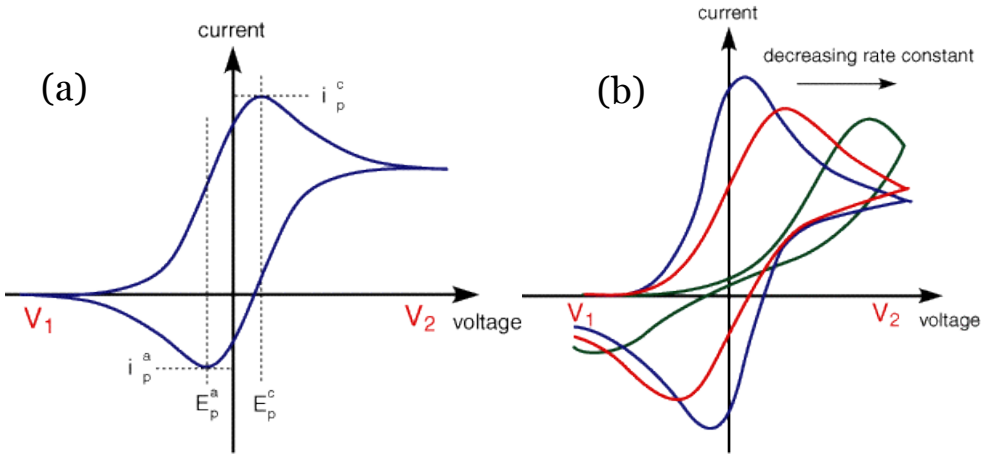

Figure A1.2. (a) A typical cyclic voltammogram; (b) shows the voltammogram for a quasi-reversible reaction for different values of the reduction and oxidation rate constants.[2]

A1.2 Experiments, results and discussions

The CV measurements were carried out for Au and Au@Ag core@shell nanoparticles with different shell thicknesses. The sample details are listed in table A1.1.

Table A1.1. Sample information for CV measurements

Sample No.	Particles Name	[Cl^-]	[Citrate]	[NO_3^-]	pH
1	$Au@Ag_{0.4nm}$	1.6 mM	2.87 mM	0.12 mM	6.60
2	$Au@Ag_{1nm}$	1.6 mM	2.87 mM	0.3 mM	6.64
3	$Au@Ag_{2.2nm}$	1.6 mM	2.87 mM	0.8 mM	6.73
4	$Au@Ag_{3.6nm}$	1.6 mM	2.87 mM	1.6 mM	7.10

Nanoparticles were dropped on the working electrode of the screen-printed carbon strip (SPCS) surface, and then left to dry in vacuum.

The voltammogram of Au and Au@Ag core@shell nanoparticles are shown in figure A1.3 and A1.4.

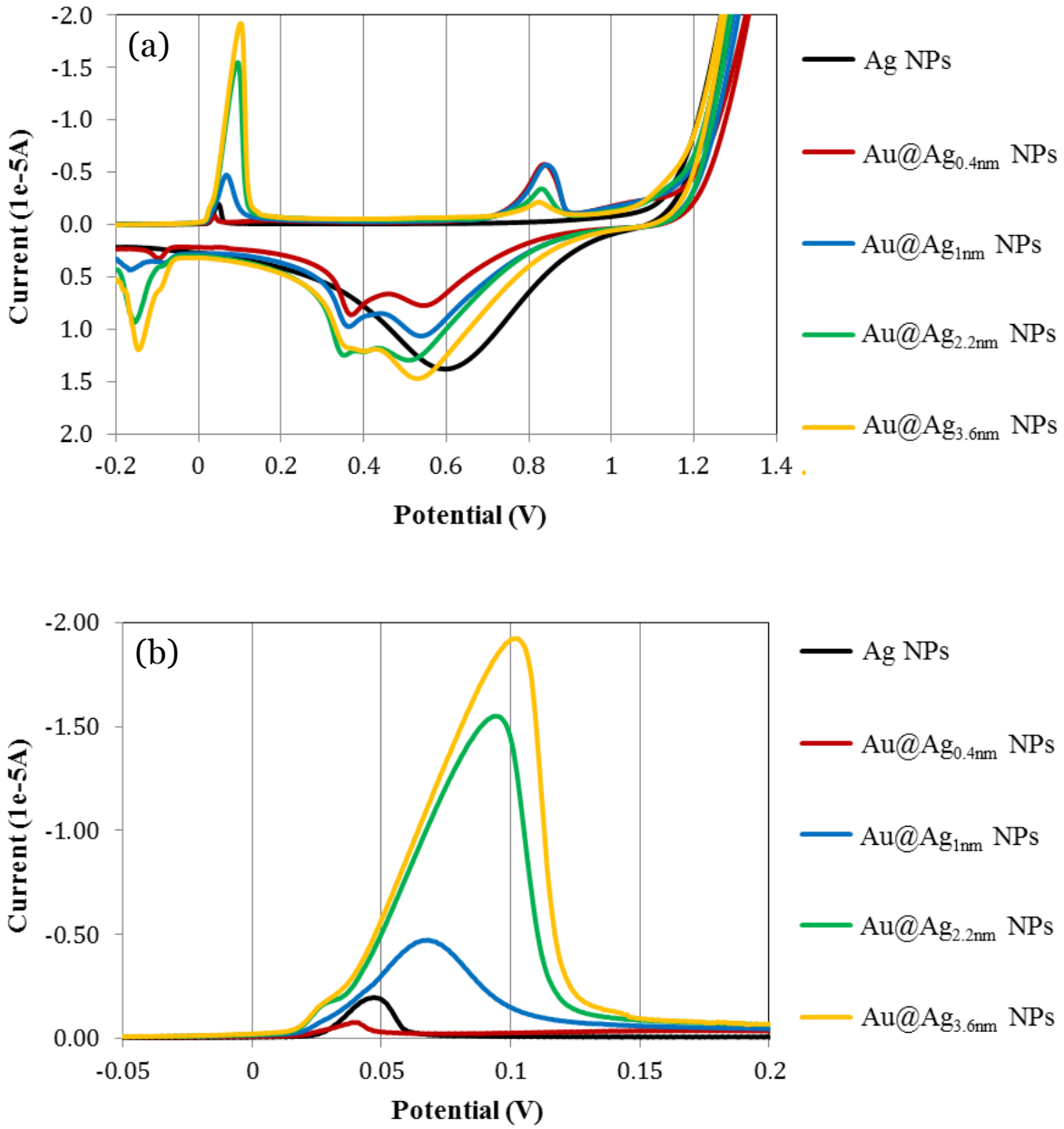

Figure A1.3. (a) Cyclic voltammetry curves and (b) magnified cathodic peak for Ag NPs and Au@Ag NPs which is diluted 10 times from original concentration.

The results show the increase of cathodic peak currents and cathodic peak potentials when the shell thickness of Au@Ag core@shell increases. This could be due to the high current which leads to high resistivity of the working electrode. And, as mentioned above, when the rate constant decreases the curves shift to more reductive potentials. In other words, these side effects are comparable to the electron charge-transfer effect in core@shell nanoparticles

which could be another factor to cause the shift of the curves. However, in these experiments the resistivity yet could be controlled. Therefore we cannot assign or clearly observe the change of reduction potential due to electron charge-transfer effect. In order to archive this, we need to carry out more controllable experiment in respect to measurement conditions.

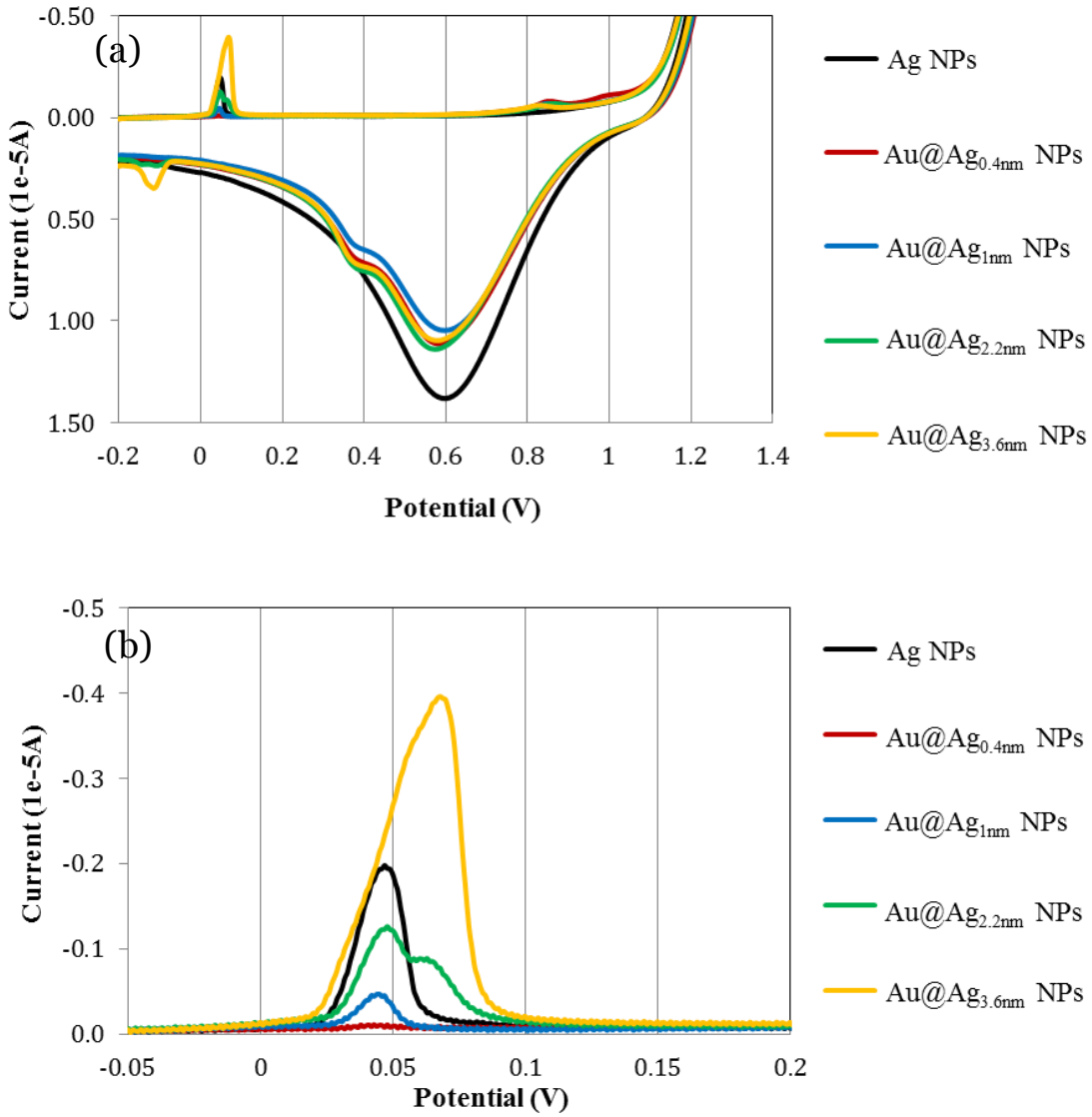

Figure A1.4. (a) Cyclic voltammetry curves and (b) magnified cathodic peak for Ag NPs and Au@Ag NPs which is diluted 100 times from original concentration.

References

(1) Kissinger, P. T.; Heineman, W. R. *J. Chem. Educ.* **1983**, *60*, 702.

(2) Linear sweep and cyclic voltammetry: the principles http://www.ceb.cam.ac.uk/.

Appendix II

for

Calculation of shell thickness of core@shell type nanoparticles

There are two ways to calculate the shell thicknesses of the resulted core@shell nanoparticles based on the information from TEM and composition measurement.

The first way is the most simple and straightforward: using TEM size measurement. TEM measurements were conducted for the core@shell nanoparticles and the core nanoparticles which were used for its synthesis. Information of nanoparticle radius was measured from TEM images. The average shell thickness (S) is

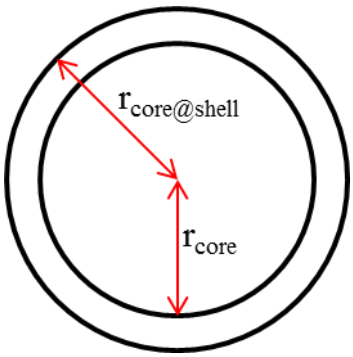

$$S = r_{core@shell} - r_{core} \tag{A2.1}$$

This method is applicable for the core@shell system which has uniform shell thickness deposited on the core. In the case of non-uniform shell thickness we should calculate it based on composition of the core@shell nanoparticles (to obtain a statistically "average" value). After calculating the core size from TEM images and knowing the composition, the shell thickness will be

$$S = \sqrt[3]{\frac{3(V_{core} + V_{shell})}{4\pi} - r_{core}^3} \tag{A2.2}$$

The ratio of V_{core}/V_{shell} will be the approximate of composition of core@shell nanoparticle if the crystal structure and lattice constant of core and shell material are similar enough (e.g. Au and Ag).

Abstract of Minor Research Project

Flourine-19 is the only stable isotope of fluorine. Its abundance is 100% and no other isotopes of fluorine exist in significant quantities. ^{19}F NMR is used for identifying fluorine-containing compounds. ^{19}F has a nuclear spin of 1/2 and a high magnetogyric ratio, which means that this isotope is highly responsive to NMR measurements. The technology for obtaining ^{19}F NMR spectra is virtually the same as getting ^{1}H NMR data. However, because a fluorine nucleus is on average surrounded by 9 electrons, rather than a single electron as is the case with hydrogen, the range of fluorine chemical shifts and the sensitivity of fluorine chemical shifts to the details of the local environment are much higher for fluorine than hydrogen. Because of its favorable nuclear properties and high abundance, ^{19}F NMR measurements are very fast compared to ^{1}H NMR measurements.

^{19}F NMR provides a unique perspective of conformation, topology and dynamics and the changes that ensue under biological conditions. In particular, ^{19}F NMR has provided insight into biologically significant events such as protein folding and unfolding, enzymatic action, protein-biological molecules interactions as well as aggregation and fibrillation.

^{19}F NMR is an invaluable tool for determination of the structure of fluorinated compounds, but the characteristics of ^{19}F NMR spectra make it very useful to investigate the interaction of fluorinated compounds with biological systems. Utilizing this can give us great imaging probes for biological events in greater detail in vivo.

This research is to study behavior of fluorine-labeled probes in detecting nucleic acid by ^{19}F NMR technique. The study can help us understand more about the interaction of probe-DNA and the effect to ^{19}F NMR signal which leads to the ability in controlling and designing new probes for nucleic acid detection.